E.Yu.Pikalova, E.G.Kalinina
Russ. Chem. Rev., 2021, **90** (6) 703 – 749

https://doi.org/10.1070/RCR4966

Solid oxide fuel cells based on ceramic membranes with mixed conductivity: improving efficiency

Elena Yu. Pikalova,[a, b]* Elena G. Kalinina [b, c]

[a] *Institute of High Temperature Electrochemistry of the Ural Branch of the Russian Academy of Sciences,*
ul. S.Kovalevskoy 22/Akademicheskaya 20, 620137 Ekaterinburg, Russian Federation
[b] *Ural Federal University,*
ul. Mira 19, 620002 Ekaterinburg, Russian Federation
[c] *Institute of Electrophysics of the Ural Branch of the Russian Academy of Sciences,*
ul. Amundsena 106, 620016 Ekaterinburg, Russian Federation

Modern approaches to increasing the efficiency of solid-oxide fuel cells (SOFCs) based on electrolytic membranes with mixed conductivity are considered. These approaches are based on material-science concepts (expansion of the electrolytic domain boundary due to the doping of basic oxides and development of various composite materials) and various technological solutions (application of electron-blocking layers on the anode and cathode sides, rational selection of the electrolyte thickness, and optimization of the electrolyte and electrode structures by synthesizing heterostructures). The methods of mathematical modelling of devices with an electrolytic membrane having mixed conductivity are analyzed in order to determine the most efficient design and optimal operation conditions for SOFCs. The application of nanocomposite electrolytes with a core – shell structure and salt composites is considered. Data on new design solutions — single-layer and single-chamber SOFCs — are presented. The prospects of the proposed approaches are evaluated.
The bibliography includes 384 references.

Contents

1. Introduction 704
2. Solid solutions based on ceria: structure, defect formation, electrical and electrolytic properties, application in SOFCs 705
   2.1. Structure and properties of ceria 705
   2.2. Structure and electrical properties of doped ceria 706
      2.2.1. Solid solutions based on ceria 706
      2.2.2. Ionic conductivity in doped CeO_2. Factors affecting the total and bulk conductivity in oxidizing media 708
      2.2.3. Grain boundary conductivity: influence of microstructure and dopant concentration. 712
   2.3. Reduction of CeO_2 electrolytes in the SOFC anode channel as a factor determining the cell specific power 713
3. Modification of the bulk properties of electrolytes based on CeO_2 717
   3.1. Criteria of choosing elements for co-doping in order to improve the electrical and electrolytic properties of CeO_2 electrolytes 717
   3.2. Co-doping with REE and alkaline-earth or alkali metal cations. Effective index 719
   3.3. Composite electrolytes based on doped CeO_2 and protonic conductors 720
4. Technologies and methods for forming multilayer structures of SOFCs and thin-film electrolytes based on ceria 720
5. Theoretical approaches to modelling SOFCs with an electrolytic membrane based on a mixed conductor 725
   5.1. Continuum and phenomenological models of the processes occurring in SOFCs 725
   5.2. Development of macroscopic continuum models of SOFC with a solid electrolyte having mixed conductivity 726
6. Nanocomposites based on electrolytes with mixed conductivity 729
   6.1. Composition and structure of salt nanocomposites 729
   6.2. Modelling of the transport properties of salt composites 730
   6.3. Experimental study of the electrical properties of salt composites 731
   6.4. SOFCs based on salt composites and ways to increase their operation efficiency 732
7. Methods aimed at increasing the SOFC performance by forming heterostructures 734
   7.1. Formation principles and properties of electrolytic heterostructures 736
   7.2. Increasing the electrode response in heterostructural systems 738
8. Modification of SOFC designs. Electrolyte-free and single-chamber cells 739
9. Conclusion 742
10. List of acronyms and designations 742

Received 1 June 2020

© 2021 Uspekhi Khimii, ZIOC RAS, Russian Academy of Sciences and IOP Publishing Limited

1. Introduction

Recently, in view of the instability in the hydrocarbon market and aggravation of environmental problems, global changes have occurred in the structure of the energy sector. The increase of the fraction of the sources alternative to conventional ones (wood, coal, oil) in the general balance of energy resources opens new horizons in the development of energy storage and distributed generation systems. Much attention is paid to fuel cells (FCs): electrochemical devices converting directly the chemical energy of fuel and oxidant, supplied separately to electrodes, into electrical energy. The high thermodynamic efficiency and continuous operation, combined with excellent environmental characteristics, are advantages of FCs over conventional power plants, such as small gas turbines and microturbines, internal combustion engines, windmills, and solar cells.[1–4]

The use of solid-oxide fuel cells (SOFCs) opens ways to design systems for different purposes: from portable to high-power stationary ones. SOFCs work in the temperature range from 500 to 1000 °C; this circumstance determines their high energy efficiency (electrical efficiency 40 – 60%)[5] and high rates of electrode reactions; it also minimizes the possibility of catalytic poisoning of electrodes. Therefore, one of important advantages of SOFCs in comparison with other classes of known fuel cells is the possibility of applying various hydrocarbons of virtually any purity as a fuel. In addition, an SOFC is a compact completely ceramic system, which does not contain any components harmful for human health. The modular principle, used in the SOFC design, makes it possible to increase easily the plant specific power and replace elements. The thermal energy produced simultaneously as a result of power plant operation, can be used in municipal engineering for hot-water supply systems. It was shown that, depending on the configuration and functioning parameters, the efficiency of integrated structures may reach 90%.[6,7] Being a promising energy storage system, reversible SOFCs can be considered as an economical solution of the problem of power consumption control using intermittent energy sources.[8–11] An analysis of the tendencies of SOFC development and research activity in this field, as well as the implementation of developed technologies, gave grounds to conclude that SOFCs are being dynamically developed and their wide commercial implementation is expected to occur in the nearest 5 – 10 years.[2,12]

A detailed review of the strategies aimed at optimizing the SOFC operation with respect to different parameters was presented by Ramadhani *et al.*[13] Computer simulation is a powerful tool for developing SOFC components, due to which researchers can predict, understand, and explain the mechanisms lying in the basis of experimentally observed properties and causes for cell degradation.[14–18] A general trend in the development of modern SOFCs is to reduce the operating temperature. In this context, much attention is paid to the material-science aspects, in particular, search for new materials with high functional characteristics in the medium-temperature (600 – 750 °C) and low-temperature (450 – 600 °C) ranges for electrolytes,[19–22] oxygen electrodes,[19,23–27] and modified cermet[28] and oxide anodes.[29] The development of new synthesis methods opens ways to obtain nanomaterials and nanocomposites with peculiar properties.[30,31]

Currently, the SOFC technology developed in Russia implies mainly the use of conventional electrolytes based on zirconia, stabilized with yttrium (YSZ) or scandium (SSZ) oxides, as the construction oxygen-conducting ceramics in commercial devices.[32–40] At a dopant concentration of 8 mol.%, the YSZ conductivity reaches 0.1 S cm^{-1} at 1000 °C. However, because of the high activation energy of ionic conductivity, the efficiency of YSZ devices, even in the thin-film design, sharply decreases even in the temperature range of 650 – 700 °C.[41] Despite the high electrical characteristics, the drawbacks of SSZ electrolytes, along with the chemical interaction with electrodes, are phase instability and rapid ceramics ageing. Co-doping with yttrium and cerium makes it possible to increase the stability of these materials;[42] however, the problem of their high cost still remains.

Materials based on CeO_2, which have a high ionic conductivity up to 500°C and are thermodynamically stable in the presence of water vapour and hydrocarbons and chemically compatible with many oxide electrodes, are promising candidates for electrolytes in new-generation SOFCs with reduced working temperature.[1] In Russia, the study of electrolyte materials based on ceria was initiated at the Institute of High Temperature Electrochemistry of the Ural Branch of the Russian Academy of Sciences back in the 1960s. The almost 40-year experience accumulated in this field of research on solid electrolytes in the Soviet Union was generalized in the review (published in English) by Kharton *et al.*[43] In addition, there are reviews of the foreign literature, concerning the investigations of the defect structure, phase transitions, and formation of local structural complexes in doped CeO_2, and also on its applications in various electrochemical technologies and catalysis.[44–47]

One of essential problems related to the use of CeO_2 electrolytes as single-electrolyte membranes is that cerium is partially reduced from Ce^{4+} to Ce^{3+} at low partial oxygen pressures. Due to this, electronic conductivity arises in the material, which may cause internal short circuit in the SOFC and, as a result, decrease in the open-circuit value (OCV) and cell specific power.[18] Various approaches have been proposed to optimize the design of SOFCs with a membrane based on electrolytes having mixed conductivity: from a structural modification to the fabrication of various composite electrolytes. The new-generation SOFCs, operating in the medium- and low-temperature ranges, are considered as promising devices for developing global hydrogen and alternative power engineering. Among the large variety of SOFCs, the cells with an electrolytic membrane based on doped ceria, which are characterized by high ionic conductivity and phase stability, are promising for wide application due to the possibility of achieving high specific power densities. At the same time, CeO_2 electrolytes are charac-

E.Yu.Pikalova. Ph.D. Senior Researcher of the IHTE UB RAS, Leading Researcher at the Departament of Environmental Economics, UrFU.
E-mail: e.pikalova@list.ru
Current research interests: seria-based materials, solid oxide fuel cells (SOFCs); electrophoretic deposition (EPD); composite material; cathode material; electrode kinetics.
E.G.Kalinina. Ph.D. Senior Researcher of the IEP UB RAS, Assistant Professor at the Departament of Physical and Inorganic Chemistry, UrFU.
E-mail: kalinina@iep.uran.ru
Current research interests: solid oxide fuel cells (SOFCs); electrophoretic deposition (EPD); nanoparticles; colloidal systems; stable suspensions; thin films; composite material.

terized by the occurrence of partial electronic conductivity in reducing media, which causes leakage because of the inner short circuit during SOFC operation and deteriorates the fuel consumption efficiency. Currently, methods of forming barrier layers to suppress the electron conductivity in electrolyte are developed, and the processes occurring in SOFCs with an electrolyte having a mixed conductivity are simulated. Some new designs have been elaborated; in particular, electrolyte-free and single-chamber SOFC designs have been proposed.

In this review, we analyze the different lines of research concerning the properties of materials based on CeO_2 and their modification for application as SOFC electrolytes and the existing methods of increasing the operation efficiency of SOFCs with an electrolytic membrane having a mixed conductivity and estimate the prospects of their incorporation into domestic technologies.

2. Solid solutions based on ceria: structure, defect formation, electrical and electrolytic properties, application in SOFCs

2.1. Structure and properties of ceria

Cerium is the first element in the lanthanide series; its electron configuration is $[Xe]4f^15d^16s^2$. It exhibits a variable oxidation state in chemical compounds: +3 or +4. Ceria(IV) CeO_2 has a cubic lattice (fluorite-type structure, space group $Fm\bar{3}m$) with a relatively large ion–ion distance, facilitating oxygen diffusion in its structure (Fig. 1 *a*).[48] The lattice parameter at room temperature corresponds to 5.411 Å.[49] In the CeO_2 structure, Ce^{4+} cations, located at the centre of oxygen cube, are coordinated by eight O^{2-} anions, which occupy tetrahedral sites, whereas octahedral sites remain unoccupied.[50] Ceria structure, having a high defect capacity, remains nevertheless stable upon heating in air in the range from room to melting temperature ~2400 °C.[44, 51] Upon heating in a hydrogen atmosphere, the fluorite structure is retained to 650 °C; nonstoichiometric oxide $CeO_{2-\delta}$, where $0 < \delta < 0.5$, is formed, which is reversibly oxidized to CeO_2 in an oxygen-containing atmosphere. The reduction at a higher temperature leads to the formation of hexagonal phase Ce_2O_3 with the lattice parameters a = 3.888 Å, c = 6.096 Å[52] (Fig. 1 *b*).

The reduction of CeO_2 to $CeO_{2-\delta}$ in the Kröger–Vink notation is described by the generation of defects in the form Ce'_{Ce}

$$2Ce_{Ce}^{\times} + O_O^{\times} \overset{K_1}{\rightleftharpoons} 2Ce'_{Ce} + V_O^{\cdot\cdot} + \frac{1}{2}O_2\,(gas) \qquad (1)$$

where $Ce_{Ce}^{\times}$ are cerium ions in the intrinsic structural site; Ce'_{Ce} are the electron defects localized on cerium ions; K_1 is the reduction reaction constant for cerium; $V_O^{\cdot\cdot}$ are the vacancies in the oxygen sublattice; $O_O^{\times}$ are the oxygen ions in proper structural sites. The charge compensation is mainly due to the generation of oxygen vacancies (the percentage of interstitial cations is < 0.1%).[44]

Vacancies in the fluorite structure tend to form associates with cations. Within the modern approach to the description of ceria defect structure, it is accepted to present singly charged ($V_O^{\cdot\cdot}$) and neutral ($V_O^{\times}$) vacancies in the form of associates of vacancies with cations: dimers $(Ce'_{Ce}-V_O^{\cdot\cdot})^{\cdot}$ and trimers $(Ce'_{Ce}-V_O^{\cdot\cdot}-Ce'_{Ce})^{\times}$ (Ref. 53). The dependences of the concentrations of individual defects, that is, oxygen vacancies (c_v), dimers (c_1), trimers (c_2), and elec-

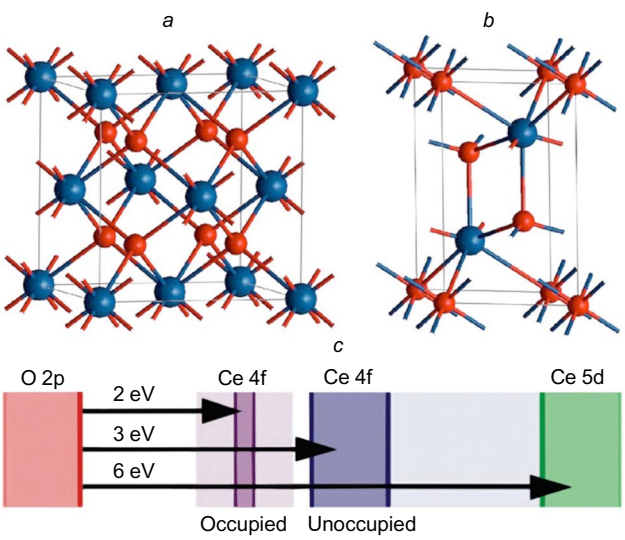


Figure 1. Crystal structures of (*a*) cubic and (*b*) hexagonal Ce_2O_3[48] and (*c*) schematic diagram of occupation of electron levels in CeO_2.[47] Ce^{4+} cations and O^{2-} anions are shown as blue and red spheres, respectively. Figures a and b are published with permission of American Physical Society.

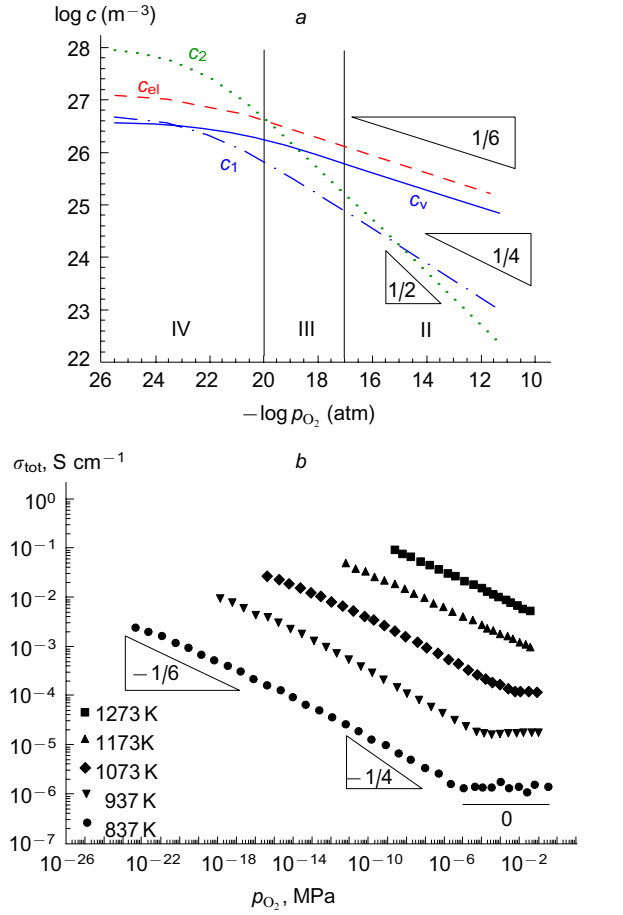


Figure 2. Dependences of the (*a*) concentrations of defects in $CeO_{2-\delta}$ — oxygen vacancies (c_v), dimers (c_1), trimers (c_2), and electrons (c_{el})[47] and (*b*) the total conductivity (σ_{tot}) of this oxide on the partial oxygen pressure.[57] Figure *b* is published with permission of IOP Publishing.

trons (c_{el}), formed during reduction of CeO_2, are presented in Fig. 2.[47] Here, four regions can be selected. Region I (is omitted) corresponds to impurity conductivity; the level of oxygen vacancies in it is determined by the presence of di- and trivalent impurities in the oxide. In region II, intrinsic defects, electrons, and unbound oxygen vacancies are dominant carriers:

$$c_{el} \approx 2\,c_v \quad (1a)$$

$$c_v \sim p_{O_2}^{-1/6} \quad (1b)$$

In region III the concentration of bound vacancies is rather high, as a result of which there are significant deviations from the dependence $p_{O_2}^{-1/6}$. In region IV no dependence of defect concentration on p_{O_2} is observed. Similar division into regions (to describe changes in the defect structure of ceria) was performed in the classical study by Tuller and Nowick.[54] Since the electron mobility (μ_{el}) greatly exceeds the mobility of ionic defects, it was suggested that the total conductivity of ceria at moderate deviations from stoichiometry is equivalent to electronic conductivity

$$\sigma_{el} = ne\mu_{el} \quad (2)$$

where e is the elementary charge.

The electronic conductivity is described in terms of the mechanism of small-radius polaron. The entire defect, which by definition is an electron in the environment of deformed lattice, moves *via* thermally activated hops. In this case, the electron mobility is defined as

$$\mu_{el} = \frac{\mu_0}{T}\exp\left(-\frac{E_H}{kT}\right) \quad (3)$$

where μ_0 is a pre-exponential factor of the temperature dependence of the electron mobility, E_H is the hop activation energy for a small-radius polaron, k is the Boltzmann constant, and T is absolute temperature.

Ceria is a wide-gap semiconductor with a band gap of 6 eV (Fig. 1 *c*).[55] The states O_{2p} form the valence band, and the state Ce_{5d} forms the conduction band. The localized unfilled level Ce_{4f} is located at a distance of $\sim$3 eV from valence band. According to the electronic structure calculations, polarons fill the states arising as a result of the reduction of CeO_2, which lie somewhat below the unfilled level Ce_{4f} at a distance of 2 – 2.4 eV from the valence band. They are also located 1 eV below the Fermi level, as was shown experimentally by X-ray photoelectron spectroscopy (XPS).[56] Dependences of the electrical conductivity of polycrystalline $CeO_{2-\delta}$ (99.9%) on partial oxygen pressure, reported by Xiong *et al.*,[57] are presented in Fig. 2 *b*. The electronic conductivity increases with an increase in temperature in the entire range of partial oxygen pressures. At a high temperature (1000 °C) the σ_{el} value decreases with an increase in p_{O_2} (the region with a slope of $-1/6$). At lower temperatures, in the range of intermediate values of p_{O_2}, one can also observe a dependence of electrical conductivity proportional to $p_{O_2}^{-1/6}$, which is transformed with a further decrease in partial pressure and becomes proportional to $p_{O_2}^{-1/4}$.

At high values of p_{O_2} and low temperatures, there are regions where σ_{tot} is independent of p_{O_2}. Many researchers explain the presence of this 'plateau' by a small contribution of extrinsic ionic conductivity. However, it was also suggested that this behaviour may be due to the appearance (as a result of 'autoionization') of intrinsic positive carriers: holes $V_O^{\bullet}$.[57] The activation energies of total conductivity, calculated for the regions with exponents of $-1/6$, $-1/4$, and 0 for the partial oxygen pressure are, respectively, 2.2, 2.9, and 1.9 eV. The total conductivity of undoped ceria is rather low: $\sim 10^{-6}$ S cm^{-1} in air at 600 °C.

2.2. Structure and electrical properties of doped ceria

2.2.1. Solid solutions based on ceria

The dopant solubility limit in the CeO_2 structure is described by introducing the concept of the energy of strains (W), which arise in the lattice because of the difference in the 'host' and dopant ionic radii. The relationship between the W value and the change in the lattice parameter of cubic fluorite (Δa) during the formation of a solid substitutional solution is given by the expression [58]

$$W = 6Ga_0(\Delta a)^2 \quad (4)$$

where G is the shear modulus and a_0 is the lattice constant of CeO_2.

Different empirical equations have been proposed to calculate the lattice parameter of a solid solution based on CeO_2 with a fluorite structure. For example, according to Hong and Virkar,[59] for trivalent dopants (M), the parameter of solid solution $Ce_{2-x}M_xO_{2-\delta}$ is given by

$$a(x, r_M) = \frac{4}{\sqrt{3}}[xr_M + (1-x)r_{Ce} + (1-0.25x)r_O + 0.25xr_{Vo}]0.9971 \quad (5)$$

where r_M, r_{Ce}, r_O, and r_{Vo} are the ionic radii of the dopant, cerium, and oxygen atoms and the oxygen vacancy, respectively, and x is the dopant mole fraction. This calculation is valid for low dopant concentrations, on the assumption that all vacancies are independent. A universal dependence for dopants with different valences was proposed by Kim [58]

$$a = 0.5413 + \Sigma(0.0220\Delta r_k + 0.00015\Delta z_k)m_k \quad (6)$$

where $\Delta r_k = (r_k - r_{Ce})$ and $\Delta z_k = (z_k - 4)$ are, respectively, the differences in the radii and valences of the kth dopant and Ce^{4+} ion and m_k is the content of the kth dopant in the solid solution (mol.%).

The theoretical value of the critical radius (r_c) of a dopant whose dissolution in a fluorite lattice causes neither its expansion nor compression ($\Delta a \to 0$), calculated from empirical dependences, amounts, according to Hong, Virkar [59] and Kim,[58] to 1.024 and 1.038 Å, respectively. It was experimentally shown that, at dopant concentrations up to $\sim$20 mol.%, the concentration dependences of parameters are linear and obey Vegard's law.[21] Note that $\Delta a \to 0$ for dysprosium, which has an ionic radius (1.027 Å) close to the theoretical value of critical radius determined by Hong anf Virkar.[59]

The data of Brauer and Gradinger [60] on the structure of solid solutions based on CeO_2 with trivalent dopants are presented in Table 1. Aliovalent doping is accompanied by the generation of oxygen vacancies, and the fluorite phase is retained to a certain concentration (x_{max}), dependent on the dopant nature. Above this limit, X-ray diffraction patterns exhibit reflections corresponding to the C-type superstructure (cubic, space group *Ia*3), which is typical of sesquioxides of REEs (from Gd to Eu), in which REE ions are octahedrally coordinated.

Based on the analysis of data in the literature, Coduri *et al.*[61] showed that the x_{max} values obtained by different

Table 1. Lattice parameters (Å) of phases of solid solutions based on CeO_2 and oxides of trivalent dopants $MO_{1.5}$.[61]

$MO_{1.5}$ content (mol.%)	$NdO_{1.5}$	$SmO_{1.5}$	$GdO_{1.5}$	$DyO_{1.5}$	$YbO_{1.5}$	$YO_{1.5}$
10	–	5.412 F	5.407 F	5.401 F	5.390 F	5.397 F
20	5.437 F	5.422 F	5.412 F	5.400 F	5.379 F	5.393 F
30	5.452 F	5.432 F	5.417 F	5.397 F	5.368 F	5.389 F
40	5.467 F	5.439 F	5.420 C	5.394 F	5.355 F	5.382 F
45	–	–	–	–	5.350 F	–
50	5.478 F	5.443 C	5.420 C	5.386 F	5.344 F (+C)	5.373 F
60	5.491 C	5.448 C	5.419 C	5.379 C	5.346 F(+C)	5.361 F
65	–	–	–	–	–	5.354 C
70	5.502 C	5.453 C	5.416 C	5.367 C	–	5.343 C
75	5.506 C	–	–	–	–	5.337 C
80	C+A	5.455 C	5.412 C	5.355 C	5.230 C (+F)	5.328 C
85	–	–	–	–	–	5.318 C
90	C+A	5.455 C	5.405 C	5.340 C	5.230 C	5.310 C
95	F	5.454 C	5.401 C	5.330 C	5.222 C	5.300 C
97.5	–	–	–	–	–	5.295 C

Note. Designations: F is a cubic phase of fluorite type (space group $Fm\bar{3}m$), C is a C-type cubic phase (space group $Ia3$), and A is a hexagonal phase (space group $P321$); impurities of the corresponding phase are indicated in parentheses.

research teams have a large spread, which may be due to the differences in both the synthesis methods and the sensitivity of the techniques used for structural analysis. According to the generalized data, the average x_{max} values for trivalent dopants lie in the range of ~35 – 60 mol.%.

Due to the application of modern high-resolution methods, such as analysis of extended X-ray absorption fine structure (EXAFS) and X-ray absorption near-edge structure (XANES) spectra and transmission electron microscopy (TEM), which make it possible to investigate local structure, ordered C-type regions were found to exist in a solid solution with a fluorite-type structure at a low dopant concentration.[62, 63] The EXAFS study revealed a decrease in the M – O bond length in the first coordination sphere for a number of rare-earth ions (from Gd^{3+} to Nd^{3+}) with an increase in the dopant content against the background of systematic increase in the lattice parameter (according to the X-ray diffraction (XRD) data) (Fig. 3 *a*). A possible reason for this contradiction is local deviations from the $Fm\bar{3}m$ symmetry, specifically, the decrease in the coordination number of near-neighbour (NN) cations and occurrence of oxygen vacancies with an increase in the dopant content. The EXAFS and XRD experimental data for a combined model structure were coordinated by Kraynis *et al.*,[64] who, using inverse Monte Carlo simulation based on the evolution algorithm, confirmed the bimodal distribution of Ce – O and M – O bond lengths in the first coordination shell and Ce – M bond lengths in the second coordination shell for the solid solutions $CeO_2 - Sm_2O_3$ and $CeO_2 - Y_2O_3$ with dopant contents of 5 and 10 mol.%, respectively. Because of this asymmetry, the NN sites are non-equivalent for oxygen vacancy hops.

One can estimate the concentration of oxygen vacancies in doped CeO_2 and obtain data on the formation of their associates with cations using Raman spectroscopy.[65] The structure of undoped CeO_2 is described by the single Raman mode T_{2g} at a frequency of 465 cm^{-1}, corresponding to symmetric vibrations of oxygen atoms near immobile cations.[66] Having analyzed the spectra recorded for the solid

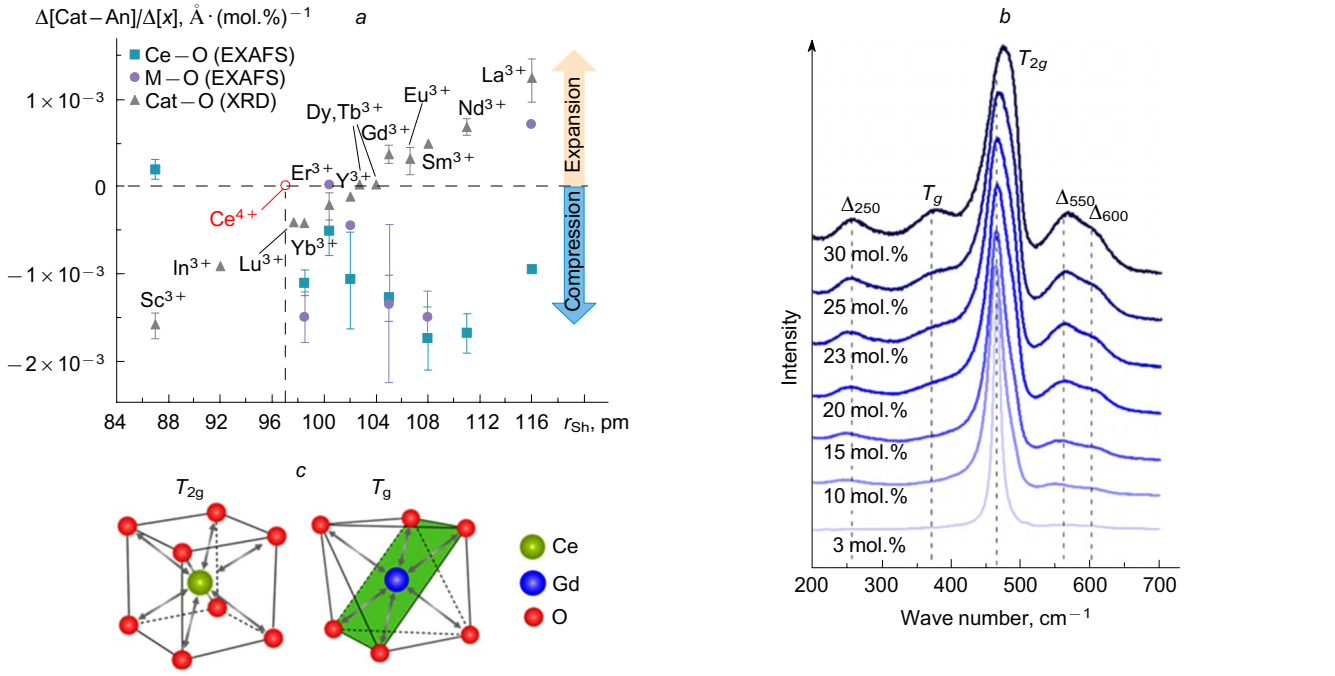


Figure 3. Generalized EXAFS and XRD data on the change in cation – anion bond lengths (ΔCat – An) in CeO_2 doped with trivalent elements (M), in dependence of their Shannon's effective ionic radius (r_{Sh}) in eight-coordinated environment (*a*);[47] Raman spectra recorded for the $CeO_2 - Gd_2O_3$ system in the range of dopant concentrations from 3 to 30 mol.%; (*b*)[67] and cation – anion bonds corresponding to Raman modes T_{2g} and T_g in fluorite and bixbyite structures, respectively (*c*).[67] Figures *b* and *c* are published with permission of American Physical Society.

solution $CeO_2-Gd_2O_3$, Schmitt *et al.*[67] indicated that, along with the red shift of the fundamental mode, additional modes occur at frequencies of 250, ~550, and 600 cm^{-1} at low dopant concentrations (denoted as Δ_{250}, Δ_{550}, and Δ_{600} in Fig. 3 *b*). The authors noted that the activation of these modes is caused by the decrease in the local symmetry due to the presence of oxygen vacancies. For a dopant content >20 mol.%, an additional mode is recorded at a frequency of 370 cm^{-1}. This mode coincides with the T_g-mode of Gd_2O_3, which is a manifestation of ordering of oxygen vacancies with the formation of a bixbyite-type structure (Fig. 3 *c*). It is of interest to use the potential of Raman spectroscopy to study *in situ* the properties of CeO_2 electrolytes under SOFC operation conditions.[68]

The critical radius of divalent ions amounts to 1.106 Å.[58] The solubility of divalent dopants in the fluorite lattice of CeO_2 is much lower than that of trivalent ones.[51] In particular, Yahiro *et al.*[69] revealed the solubilities of Sr^{2+} and Ca^{2+} in CeO_2 to be ~8 and 23 mol.%, respectively; solid solutions with Ba^{2+} and Mg^{2+} cannot be formed. The high solubility of Ca^{2+} is confirmed by the results of Thangadurai and Kopp,[70] who proposed a method for preparing a solid solution $Ce_{1-x}Ca_xO_{2-\delta}$ with a dopant concentration up to 20 mol.% at a calcination temperature of ⩽400 °C. Júnior *et al.*[71] and Anjaneya *et al.*[72] evidenced the occurrence of $SrCeO_3$ peaks in XRD patterns and Raman spectra of a solid solution $Ce_{1-x}Sr_xO_{2-\delta}$, obtained with application of citrate and hydrothermal methods, even with a dopant content >5 mol.%. Milliken *et al.*[73] investigated the solubility of Sr^{2+} in CeO_2 when carrying out solid-phase synthesis in different media, as well as the stability of solid solution under conditions of electrochemical potential gradient. It was shown that a solubility limit of 10 mol.% is obtained both in air and in an atmosphere of H_2 + 3% H_2O at 1000 °C; according to the XRD data, the thus formed materials were single-phase. At the same time, testing of an electrolyte with 10 mol.% Sr^{2+} in an SOFC subjected to long-term exposure (>1000 h) at 750 °C revealed precipitation of 'spurious' phases, SrO, $Sr(OH)_2$, and $SrCO_3$, at the electrolyte/anode interface, as a result of which the cell output was significantly deteriorated. It was noted that the chemical expansion of electrolyte in wet hydrogen decreases with an increase in the dopant content. In particular, materials with 4, 10, and 35 mol.% Sr^{2+} at 1000 °C demonstrate expansion by 2.3, 2.0, and 0.5% [1.5% for $Ce_{0.8}Gd_{0.2}O_{1.9}$ (GDC20)].

As the experiments[43] showed, solid solutions are not formed in the CeO_2-BaO system. The formation of cerate $BaCeO_3$ was found by XRD for the $0.5\,CeO_2-0.5\,BaO$ composition. However, as the authors noted, the observed rise in the electrical conductivity with an increase in the barium content in the system to 10 mol.% may be related to the low solubility of this element in the fluorite lattice with the formation of grain boundary mosaic structures. No solid solutions were found in the CeO_2-MgO system; however, MgO is used as a sintering and strengthening additive to electrolytes based on CeO_2.[74] Other examples of modifying additives are Al_2O_3 and TiO_2, which also exhibit limited solubility in the fluorite structure.[75, 76]

To form gas-tight ceramics based on CeO_2 from powders prepared by conventional solid-phase synthesis, one needs temperatures above 1600 °C. Higher sintering temperatures must be used for dopants of larger radius and for higher dopant concentrations. Along with the use of highly dispersed and readily sintered materials obtained by chemical methods, various sintering additives are applied, in particular, transition metal oxides, which make it possible to reduce the sintering temperature by 100 – 300 °C.[77 – 80] Other additives in use are Bi_2O_3 (Ref. 81) and salts of alkali elements.[82] Different mechanisms have been proposed to explain the enhancement of sintering caused by introduction of these additives:

— liquid-phase sintering with the formation of an additive – electrolyte liquid phase at grain boundaries, which facilitates rapid mass transfer and formation of a dense structure at relatively low temperatures;[81]

— mechanism of 'viscous flow' with the formation of amorphous films on the surface of electrolyte particles, reducing the friction between them.[83] Along with the enhancement of strengthening properties of material, these additives can improve its electrical properties of materials, neutralizing the SiO_2 impurity at grain boundaries (the so-called scavending effect).[84]

It was revealed in a number of studies that doping with transition metals (Co, Ni, Cu, Fe) may reduce the polarization of oxygen electrodes contacting with a CeO_2 electrolyte, which is due to the increase in the oxygen exchange rate because of the high p-type electronic conductivity on the electrolyte surface.[84, 85] A similar effect was also observed for GDC20 doped with praseodymium (2 mol.%); praseodymium cations simultaneously enhance the electron – hole transport and act as catalytically active sites.[86] The introduction of transition metal additives, even in small amounts (2 mol.%), leads to the occurrence of p-type conductivity in the electrolyte in air; however, its value decreases with a decrease in temperature (the ion transport numbers are 0.89 and 0.99 at 1000 and 650 °C, respectively).[79]

2.2.2. Ionic conductivity in doped CeO_2. Factors affecting the total and bulk conductivity in oxidizing media

The equation for the reaction of formation of impurity defects in a material doped with trivalent-element oxide has the following form in the Kröger – Vink notation:

$$M_2O_3 \rightarrow 2\,M'_{Ce} + V^{\cdot\cdot}_O + 3\,O^{\times}_O \qquad (7)$$

Since the concentration of intrinsic defects in CeO_2 is low at high partial oxygen pressures, the defect concentration and electrical properties are determined by the dopant content

$$[V^{\cdot\cdot}_O] = \frac{1}{2}[M'_{Ce}] \qquad (8)$$

The ionic conductivity (σ_{ion}) of pure oxygen-ion conductor is described by the equation

$$\sigma_{ion} = [V^{\cdot\cdot}_O] N_O\, q_{ion} \mu_{ion} \qquad (9)$$

where $[V^{\cdot\cdot}_O]$ is the mole fraction of mobile oxygen vacancies in the oxygen sublattice, N_O is the number of 'oxygen' sites per volume unit, q_{ion} is the charge of oxygen ion, and μ_{ion} is its mobility.

The conductivity in oxygen-ion conductors is a thermally activated property. The empirical temperature dependence of electrical conductivity of doped fluorite-type oxides has the form[44]

$$\sigma T = \sigma_0 \exp\left(-\frac{E_a}{kT}\right) \qquad (10)$$

where σ_0 is the pre-exponential factor and E_a is the electrical conductivity activation energy. Within the simplest theory of random walks, the electrical conductivity obeying the vacancy mechanism can be presented as

$$\sigma T = A \exp\left(-\frac{\Delta H_m}{kT}\right) \quad (11)$$

Here, A is the pre-exponential factor and ΔH_m is the change in enthalpy as a result of oxygen ion transport.

In the case of fluorite-type lattice, the Arrhenius equation for the electrical conductivity can be written as

$$\sigma T = \frac{q_V^2}{k}[V_O^{\cdot\cdot}] N_O a^2 v_O \exp\left(\frac{\Delta S_m}{k}\right) \exp\left(-\frac{\Delta H_m}{kT}\right) \quad (12)$$

where q_V is the oxygen vacancy charge, a is the distance at which oxygen ion hops, v_O is the oxygen ion hopping rate, and ΔS is the change in entropy. It is noteworthy that the value $[V_O^{\cdot\cdot}]$ in this equation is the concentration of mobile oxygen vacancies involved directly in the charge transfer.

A specific feature of solid solutions based on CeO_2 is that, as a result of the doping-induced lattice distortion, oxygen vacancies may interact with dopant cation to form local structures $(M'_{Ce} - V_O^{\cdot\cdot} - M'_{Ce})^{\times}$ and $(M'_{Ce} - V_O^{\cdot\cdot})^{\cdot}$; thus, additional energy is required to release them from such clusters to be involved in transport. The binding energy in these structures is mainly due to the Coulomb interaction; however, it contains also a component related to the lattice relaxation around the defect, which depends on the dopant nature. Thus, in the low-temperature range the activation energy of ionic conductivity contains, along with the migration enthalpy (ΔH_m), an additional component (ΔH_a), related to the formation of vacancy – cation associates.

Jung *et al.*[87] selected linear portions with different slopes in the Arrhenius dependence of the electrical conductivity of $(CeO_2)_{1-x}(SmO_{1.5})_x$ on temperature, $\ln(\sigma T) - 1000/T$; these portions interest at some critical temperature T_c (Fig. 4 *a*). Below T_c mobile oxygen vacancies are captured into ordered clusters with a dopant cation, whereas above T_c all oxygen vacancies are mobile. Having modified Eqn (12),

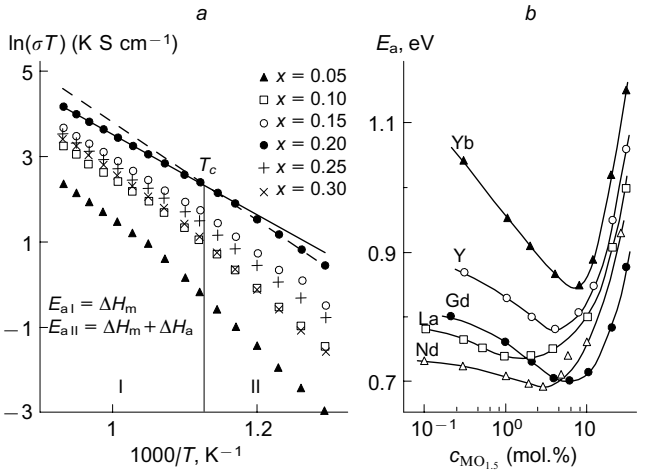


Figure 4. Arrhenius dependences of electrical conductivity of $(CeO_2)_{1-x}(SmO_{1.5})_x$ (regions with different activation energies are presented [87]) (*a*) and dependences of the activation energy of ionic conductivity in $CeO_2 - M_2O_3$ solid solutions on the dopant concentration (*b*).[88]

Jung *et al.*[87] proposed the following equations to calculate the electrical conductivity on isolated portions:
for $T < T_c$

$$\ln(\sigma T) = \ln\left(A'' \exp\frac{\Delta H_a}{kT_c}\right) - \frac{\Delta H_m + \Delta H_a}{kT} \quad (13)$$

for $T > T_c$

$$\ln(\sigma T) = \ln A'' - \frac{\Delta H_m}{kT} \quad (14)$$

where

$$A'' = \left(\frac{q_V^2}{k}\right)[V_O^{\cdot\cdot}] N_O a^2 v_O \exp\left(\frac{\Delta S_m}{k}\right) \quad (14a)$$

At temperatures below critical the pre-exponential factor in the Arrhenius equation and the activation energy of total conductivity have an additional term, related to the formation of vacancy associates. The value T_c, depending on the dopant concentration, ranges from 591 to 673 °C (the minimum is at the dopant concentration $x = 0.20$). The maximum conductivity (0.56 S cm^{-1} at 800 °C) and minimum E_a (0.82 eV) and ΔH_a (0.18 eV) values also correspond to $x = 0.20$.

Faber *et al.*[88] calculated (based on experimental data) the ΔH_a values for a number of trivalent dopants; the lowest values were obtained for Nd^{3+} (0.23 eV), La^{3+} (0.29 eV), and Gd^{3+} (0.32 eV). The E_a values reach a minimum at the dopant concentration ~3 – 8 mol.% (Fig. 4 *b*). The presence of minimum is explained by the fact that more neutral dimers are formed at a higher dopant concentration $(M'_{Ce} - V_O^{\cdot\cdot} - M'_{Ce})^{\times}$; the binding energy significantly increases, which leads to a drop of conductivity and a sharp increase in the activation energy.

The results of calculating the formation energy for vacancy associates, performed by Minervini *et al.*,[89] are presented in Fig. 5 *a*. The authors considered the NN (point *1* in the inset of Fig. 5 *a*) and next-near neighbour (NNN) (points *2* and *3* in the inset) interaction. According to the data obtained, cations with an ionic radius smaller than the Gd^{3+} radius undergo mainly NN interactions with vacancies, whereas cations with a larger ionic radius demonstrate an opposite tendency; the minimum of interaction in two coordination spheres corresponds to Gd^{3+}. The minimum binding energy for Gd^{3+} (0.17 and 0.26 eV for NN and NNN) was calculated by Butler *et al.*[90] using the Mott – Littleton generalized procedure. Among divalent dopants, higher binding energies were observed for Ca^{2+} (1.08 and 1.58 eV) and Mg^{2+} (1.23 and 1.86 eV). Based on *ab initio* quantum mechanical calculations with allowance for the NN and NNN interactions, Andersson *et al.*[91] established the minimum of binding energy for Pm^{3+} (0.02 eV); a minimum ionic conductivity activation energy was also noted for this dopant (Fig. 5 *b*). The calculations were performed for two extreme cases: NN cations and cations in the absence of vacancy in the nearest environment (isolated cations), which may occur at a dopant concentration of 4.2 mol.%. It was demonstrated that the obtained results are in good agreement with the experimental data on a similar dopant content.[88] It was shown that doubly doped systems (Nd + Sm, Pr + Gd) have lower binding energies, which are close to the optimal values obtained for Pm^{3+}.

Ceramic electrolytes are polycrystalline compacts, whose conductivity is determined by the grain bulk (σ_g) and grain boundary (σ_{gb}) contributions; the latter are measured using *ac* impedance spectroscopy. Impedance

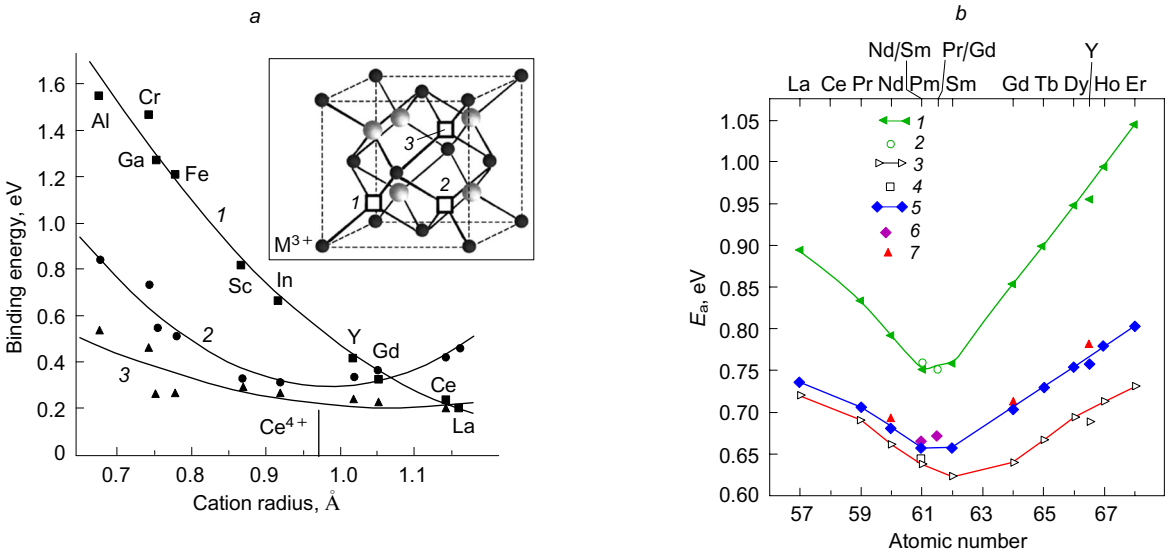


Figure 5. Theoretical dependences of the dopant cation binding energy with oxygen vacancies of the first (1), second (2), and third (3) orders (points 1, 2, and 3, respectively, in the inset) (*a*)[89] and dependences of the ionic conductivity activation energy on the atomic number of dopant (4.2 mol.%): calculation results for the first-order vacancies (shown green), isolated defects (red), and averaged effective activation energy at $E_m = 0.5$ eV (blue) and experimental values (*b*). (*b*): (*1*) Near neighbour of M^{3+}, (*2*) near neighbour of M^{3+} (Nd/Sm or Pr/Gd), (*3*) isolated ion M^{3+}, (*4*) isolated ion M^{3+} (Nd/Sm or Pr/Gd), (*5*) effective mean, (*6*) effective mean (Nd/Sm or Pr/Gd), and (*7*) experimental values. Figure *a* is published with permission of Elsevier; Fig. *b* was compiled by the authors based on the data of Refs 88, 91.

spectroscopy data can be interpreted within different models, among which the brick layer model (BLM) is most popular.[92–94] In terms of this model, grains are cubes with an edge length d_g, separated by a thin grain boundary of thickness δ_{gb} (Fig. 6 *a*). The classical brick layer model (S-BLM)[78,94] is applied to ceramics with a grain size of $\sim 1-2$ μm and high-resistance grain boundaries; this model consideres current flow through the grain bulk and the boundary perpendicular to the grain surface. Fitting of impedance spectra is performed in terms of an equivalent circuit, representing a series connection of circuits (including resistance R and capacitance C) R_gC_g and $R_{gb}C_{gb}$ (Scheme *1* in Fig. 6 *b*). Using the resistances and characteristic capacitances, obtained by fitting the spectra, and, with the sample geometric sizes known, one can calculate the electrical conductivity in the grain bulk and boundaries and estimate the grain boundary thickness.[78]

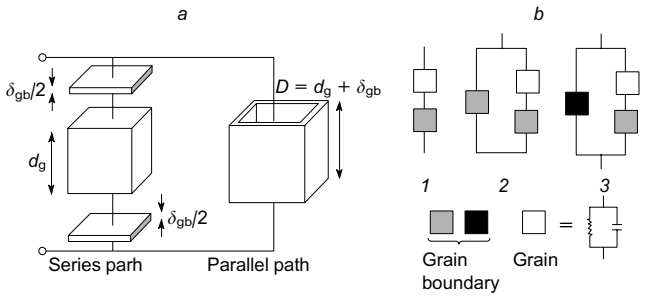


Figure 6. Block model of grain bulk and grain boundary conductivity of polycrystalline materials (*a*) and equivalent circuits for describing impedance spectra in terms of the block model with allowance for the asymmetry of transport properties along (gray squares) and across (black squares) grain boundaries (*b*).[93] (*1*) $d_g \gg \delta_{gb}$, (*2*) $d_g \approx \delta_{gb}$, (*3*) $d_g \approx \delta_{gb}$. Published with permission of Springer Nature.

For nanoceramics, in which grain boundaries and grains themselves have comparable sizes, one must take into account the additional way of current flow along grain boundaries. Thus, one should use the SP-BLM model considering series R_gC_g and $R_{gb}C_{gb}$ circuits, connected in parallel with the $R_{gb}C_{gb}$ circuit (Scheme *2* in Fig. 6 *b*).[78,95] A modified model was proposed (SP′-BLM)[96] (Scheme *3* in Fig. 6 *b*) to distinguish conveniently between the conductivities along and across grain boundaries.

Far from always one can select two well-resolved lines corresponding to the grain bulk and boundary in the spectra of polycrystalline electrolytes. The behaviour of such materials is described within the Maxwell–Wagner effective-medium theory, universal model of embedded cube, *etc.*[93,97] Equivalent schemes related to the models in which grain boundaries, in contrast to the brick layer model, are not considered as an individual phase containing glasslike impurities were described by van Herle *et al.*[92] In the models presented by the authors, the grain–grain contact is interpreted as a blocking or partially blocking zone, in which ion transport is hindered as a result of the formation of a space charge caused by non-equilibrium distribution of point defects at the grain boundary and in the grain bulk.

In early studies, the choice of dopant at which maximum bulk conductivity is attained was justified based on the methodology proposed by Kilner and Brook.[98] Maximum conductivity is expected for a dopant whose introduction causes minimum elastic stress in the lattice; ideally, the difference between the dopant ion radius (r_d) and critical radius (r_c) should tend to zero:

$$|r_d - r_c| \rightarrow 0$$

According to Kim,[58] the theoretical value r_c, calculated from empirical dependences, is 1.038 Å. The minimum of $|r_d - r_c|$ correspond to the cation Gd^{3+}; therefore, maximum values of conductivity can be achieved by doping with gadolinium. Indeed, an analysis of the data of different

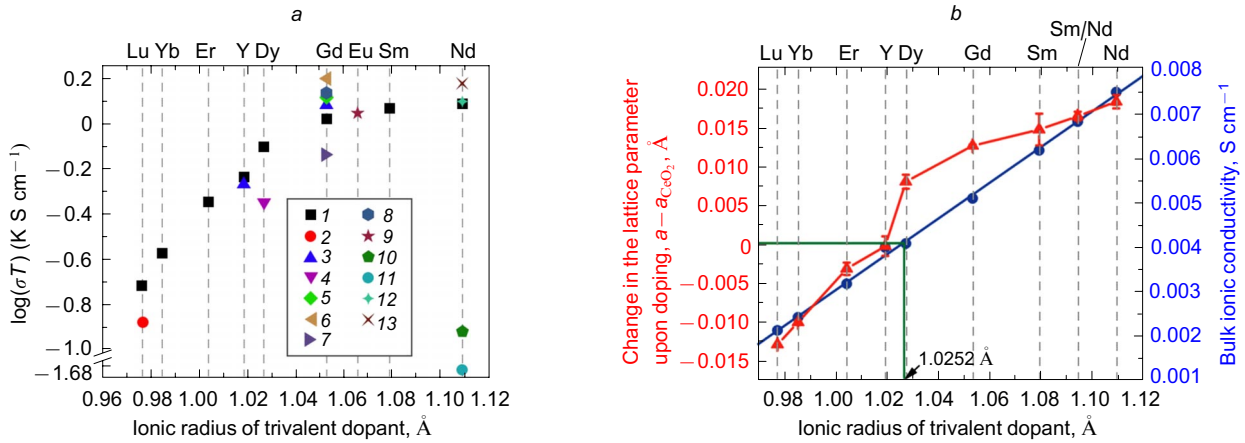


Figure 7. Values of bulk conductivity (*a*)[112] and change in the lattice parameter upon doping in dependence of the dopant radius (*b*).[99] (*a*) Dopant concentration 10 mol.%, T = 400 °C, data of Refs 1 (99) 2 (100) 3 (101) (4) (102) (5) (103) 6 (104) 7 (105) 8 (106) 9 (107) 10 (108) 11 (109) 12 (110) 13 (111); (*b*) dopant concentration 10 mol.%, T = 500 °C. Figure *a* is published with permission of Royal Society of Chemistry. Figure *b* is published with permission of American Ceramic Society.

research teams on the conductivity of CeO_2-based electrolytes at 400 °C showed that the highest values of conductivity are obtained for the Gd^{3+} dopant (Fig. 7 *a*).[99–111] To determine the radius of 'ideal dopant' at SOFC working temperatures, Omar *et al.*[99] performed high-temperature experiments aimed at studying the structure of a number of CeO_2 electrolytes and obtained the value r_d = 1.0252 Å, which corresponds to the minimum difference in the lattice parameters of doped and undoped samples at 500 °C (Fig. 7 *b*). In the case under consideration, this radius corresponds to Dy^{3+}; however, the largest values of bulk conductivity were found for $Ce_{0.9}Nd_{0.1}O_{1.95}$ (NDC10) (7.25 mS cm^{-1}) and CeO_2, co-doped with Nd^{3+} and Sm^{3+} [$Ce_{0.9}(Sm_{0.5}Nd_{0.5})_{0.1}O_{1.95}$ (SNDC10)] (7 mS cm^{-1}).

In recent study by Koettgen *et al.*[112], a method based on combined calculations within the density functional theory (DFT) and kinetic Monte Carlo method was proposed to determine the ionic conductivity. The migration of vacancies between two neighbouring tetrahedral oxygen sites in the lattice along the (100) direction was considered. A

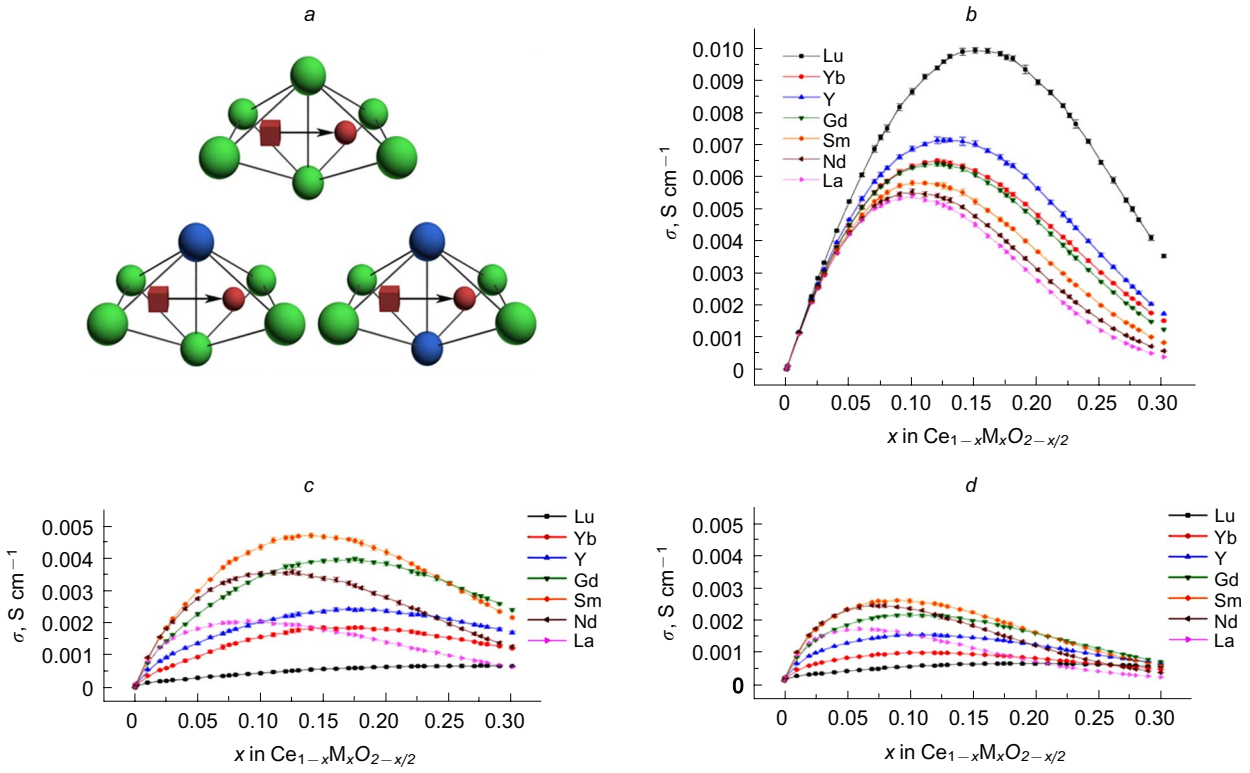


Figure 8. Possible barriers for oxygen vacancy migration in CeO_2 doped with a rare-earth element (Ce – Ce, Ce – M, M – M) (*a*) and theoretical concentration dependences of ionic conductivity at 500 °C, obtained considering only vacancy blocking effect (*b*), only vacancy trapping (*c*), and both vacancy blocking and trapping (*d*).[112] In Fig. *a* cerium ions are shown green, REE ions (M) are blue, and oxygen ions and vacancies are violet (spheres and cubes, respectively). Published with permission of Royal Society of Chemistry.

moving vacancy should overcome the migration barrier formed by the binding energy of two cations (Fig. 8 *a*). In terms of this approach the migration energy was analyzed from the point of view of symmetry/asymmetry of vacancy hops in the forward and backward directions — cases denoted by the authors as blocking and trapping, respectively. Trapping describes the effect of associates of dopant ions and oxygen vacancies on the migration energy. The energy barrier for a vacancy hop in doped CeO_2 is higher than in the undoped material; at the same time, a hop in the backward direction is energetically more favourable (asymmetry). The blocking effect is related to the increase in the energy barrier for a hop as a whole (in both forward and backward directions) due to the presence of dopants in the lattice. The results are presented in Figs 8 *b* – *d*. The blocking effect determines the dopant concentration at which the maximum ionic conductivity is obtained, and the trapping effect determines the value of maximally attainable conductivity.

The ionic conductivity activation enthalpy increases with an increase in the height of Ce – M energy barrier and the dopant concentration. Medium-size cations (samarium and neodymium) have a minimum activation enthalpy. Due to this, the calculated activation energies of ionic conductivity exceed the experimental values, because the influence of grain boundary effects is disregarded. The difference in the activation enthalpies in high- and low-temperature regions is insignificant.

2.2.3. Grain boundary conductivity: influence of microstructure and dopant concentration.

It is generally accepted that, because of the presence of impurities and formation of SiO_2-based glasslike phases at grain boundaries, the grain boundary contribution to conductivity is smaller than the grain (bulk) contribution ($\sigma_{gb} < \sigma_g$) and has a higher activation energy; therefore, its influence on the electrolyte conductivity may be decisive in the low-temperature range. In addition, σ_{gb} depends also on the dopant concentration. As an example, we will consider the concentration dependence of the grain boundary conductivity in $CeO_2 - GdO_{1.5}$ systems with high and low impurity contents. For an electrolyte with a high impurity content, the total conductivity is limited by the low grain boundary conductivity, with a maximum attained at a dopant content of 20 mol.% (GDC20) (Fig. 9 *a*).[113] The grain boundary conductivity reaches a maximum at a dopant content of 25 mol.%. The grain conductivity of the material becomes maximum at a dopant content of 10 mol.% and decreases with a further increase in the dopant level. Thus, at a low temperature (500 °C), $\sigma_{tot} < \sigma_g$ in the entire concentration range. For a system with a low impurity content the contribution of grain-boundary resistance (R_{gb}) becomes insignificant at a dopant content of 10 mol.% $Ce_{0.9}Gd_{0.1}O_{1.95}$ (GDC10); in this case, the total conductivity becomes high (9.5 – 54.4 mS cm^{-1} at 500 – 700 °C). The R_{gb} fraction is insignificant even at a temperature of ~400 °C, whereas for GDC10 and GDC20, characterized by a high impurity content, R_{gb} makes a significant contribution up to temperatures of 1000 and 700 °C, respectively (Fig. 9 *b*).

Hong *et al.*[114] investigated the influence of the microstructure and concentration (3 – 21 mol.%) of some trivalent dopants (Dy^{3+}, Er^{3+}, Gd^{3+}, Ho^{3+}, La^{3+}, Nd^{3+}, Sm^{3+} and Yb^{3+}) on the σ_{gb} and σ_g values. It was shown that the grain-boundary resistance is inversely proportional to the dopant radius. The partial values σ_{gb} and σ_g increase with an increase in the dopant content; however, in this case the grain conductivity activation energy is lower than the activation energy of grain-boundary conductivity, especially at low dopant contents. The contribution of grain-boundary resistance to the total resistance decreases with an increase in the dopant concentration. A study of the sample microstructure did not confirm the presence of glasslike phases, however, a decrease in the dopant concentration was found on grain boundaries for Er^{3+}-containing samples; for the samples doped with Dy^{3+} the dopant cation concentration was the same in the grain bulk and on grain boundaries.

Tschöpe *et al.*,[115] who investigated the blocking effect of grain boundaries in electrolytes with dopant (Y, Gd, La) contents from 0.1 to 27 mol.%, showed that, at low dopant concentrations, σ_g exceeds σ_{gb} by four orders of magnitude; the difference decreases significantly with an increase in the dopant concentration >10 mol.%. The authors demonstrated satisfactory agreement between the experimental

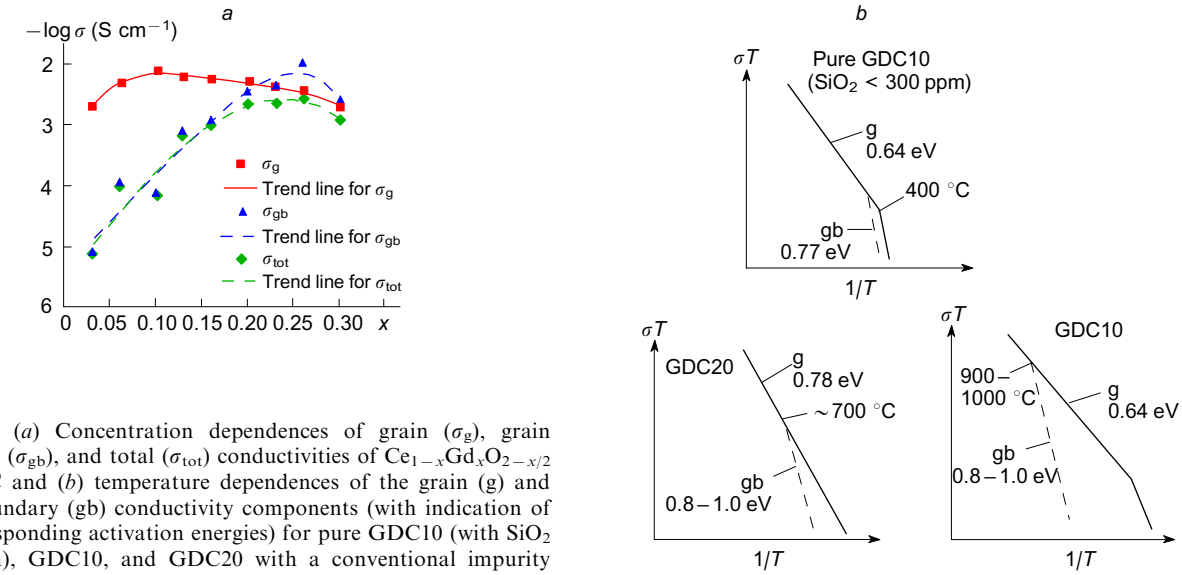


Figure 9. (*a*) Concentration dependences of grain (σ_g), grain boundary (σ_{gb}), and total (σ_{tot}) conductivities of $Ce_{1-x}Gd_xO_{2-x/2}$ at 500 °C and (*b*) temperature dependences of the grain (g) and grain boundary (gb) conductivity components (with indication of the corresponding activation energies) for pure GDC10 (with SiO_2 < 30 ppm), GDC10, and GDC20 with a conventional impurity content.[113] Published with permission of Elsevier.

results and theoretical dependences, obtained by calculation within the modified space-charge model, developed by them with allowance for the nonequilibrium distribution of point defects. The oxygen vacany formation enthalpy on grain boundaries is lower as compared with grain bulk; therefore, the vacancy concentration on grain boundaries increases. The excess charge of grain shell is screened by the newly formed space charge layer with a characteristic thickness λ (Debye length), in which electrons are accumulated, and vacancy concentration is reduced. Therefore, this layer can block the ionic conductivity in electrolyte.[116]

A number of studies (see, *e.g.*, Refs 115, 117 – 121) were devoted to the influence of size factor on the grain boundary conductivity and the relationship between the ionic and electronic conductivities in undoped and doped CeO_2 and theoretical simulation of the behaviour of systems within the space-charge theory. Consideration of this question is important because of the well-known advantages of nanoscale YSZ electrolytes.[122, 123] Submicron materials based on CeO_2 were also found to have high ionic conductivity.[124, 125] For example, it was shown[125] that the grain boundary conductivity of submicron YSZ electrolyte obtained by laser evaporation increases with a decrease in the grain size in the range of 800 – 90 nm (in contrast to the tendency for microscale materials). The conductivity of thin-film (10 μm) electrolyte based on such submicron powders (57 mS cm^{-1} at 900 °C and $E_a \approx 1$ eV) practically corresponds to the single-crystal conductivity. The application of this electrolyte in a single SOFC with a carrier tubular electrolyte 140 μm thick made it possible to obtain specific power values of 300 – 600 mW at 785 – 883 °C and high OCV ($\sim$1.1 V).[126] Gorelov *et al.*,[127] who studied $CeO_2 - GdO_{1.5}$ samples fabricated by the same method, with a dopant concentration of 20 mol.%, obtained values of conductivity 127 – 170 mS cm^{-1} at 900 °C and $E_a \approx 0.8$ eV; the range of variation in the grain size in samples of sintered ceramics turned out to be 90 – 200 nm.

Nevertheless, it is known that the transition to the size scale on the order of 1 – 10 nm in doped CeO_2 can be accompanied by an increase in the n-type conductivity due to the increase in the concentration of small polarons in the interfacial region. This effect is observed also in undoped CeO_2 with an impurity level of 1000 ppm (Fig. 10 *a*).[117] Mainly ionic conductivity is observed for the CeO_2-based material with a grain size > 1000 nm. With an increase in the acceptor dopant concentration, the range of dominant ionic conductivity shifts towards smaller grains (Fig. 10 *b*).[118] In particular, for the material with a dopant content of 10 mol.%, ionic conductivity dominates at a grain size > 20 nm, which is in good agreement with the data of Gorelov *et al.*[127] Mixed oxygen ionic and electronic conductivity (provided that the σ_{ion} and σ_{el} values are equal) of an electrolyte with 10 mol.% dopant increases by two orders of magnitude with a decrease in the grain size (Fig. 10 *c*), whereas the mixed conductivity of undoped cerium in the nano- and micrometre-sized state differs by four orders of magnitude. The distributions of electron and ion carriers in this mixed conductor were found in the aforementioned studies[115, 117, 118] by solving numerically the three-dimensional Poisson – Boltzmann equation in the finite-difference approximation at a difference of 2.3 eV between the enthalpies of oxygen vacancy formation in the grain bulk and on the grain boundary. They are in good agreement with the experimental data on the conductivity and Seebeck coefficients for nanoscale CeO_2 (the references to the corresponding experimental studies are given in Ref. 117). Based on the data obtained, one can choose appropriate synthesis methods and dopant concentrations to prepare CeO_2-based electrolytes with desired electrolytic properties.

Among reviews, we should mention the publication by Gregory *et al.*,[128] who discussed in detail the influence of grain boundaries on the properties of different oxygen ionic and protonic conductors and considered the theoretical models and practical approaches to increase the grain boundary conductivity.

2.3. Reduction of CeO_2 electrolytes in the SOFC anode channel as a factor determining the cell specific power

The rate of electrochemical reactions in SOFC is determined to a great extent by the cell operation conditions, *i.e.*, by the temperature and difference in partial oxygen pressures in the anode and cathode compartments. The partial oxygen pressure in the cathode channel is chosen in the range of 0.21 – 1 atm, while a reducing atmosphere is formed in the anode channel ($p_{O_2} \approx 10^{-30} - 10^{-20}$ atm at 500 – 700 °C

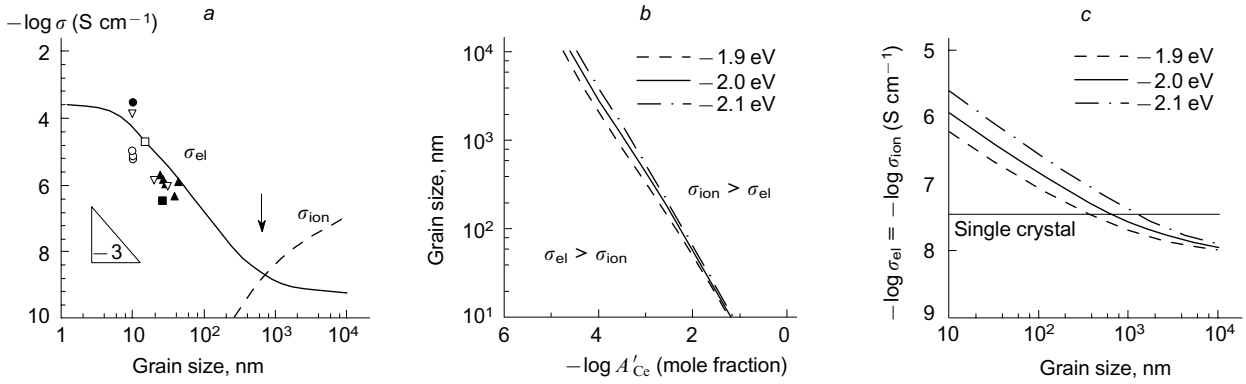


Figure 10. (*a*) Theoretical dependences of σ_{ion} and σ_{el} on the grain size for CeO_2 with an impurity content of 1000 ppm (in comparison with the corresponding experimental data, shown by different symbols)[117] and dependences of the electrolytic domain boundary ($\sigma_{ion} = \sigma_{el}$) in doped CeO_2 on the (*b*) dopant content and (*c*) the grain size at a dopant concentration of 10 mol.%. The slope of −3 in Fig. *a* corresponds to the portion of plot with experimental points; in Figs *b* and *c*, the differences in the oxygen vacancy formation enthalpies in grain bulk and on grain boundaries are indicated for the corresponding curves. The data are given for T = 500 °C and $p_{O_2} = 0.21$ atm.[118] Published with permission of Springer Nature.

when wet hydrogen is used as a fuel).[113] Under reducing conditions electrolytes based on CeO_2 are characterized by the occurrence of partial electronic conductivity, whose value depends on the external conditions. The occurrence of the electronic component of conductivity in CeO_2 electrolyte in a reducing atmosphere is related to the formation of oxygen vacancy excess [see Eqn (1)], as a result of which electronic defects — small-radius polarons Ce'_{Ce} — are formed. At small deviations from stoichiometry (δ) in $Ce_{2-x}M_xO_{2-x/2-\delta}$, when free doubly charged oxygen vacancies dominate, the concentration of electron defects is determined by the relation

$$[Ce'_{Ce}] = K_r(T)^{1/2}[V_O^{\cdot\cdot}]^{-1/2}p_{O_2}^{-1/4} \quad (15)$$

where K_r is the cerium reduction reaction constant.

Disregarding the concentration of reduced cerium in comparison with the dopant concentration in the electroneutrality condition

$$2[V_O^{\cdot\cdot}] = [Ce'_{Ce}] + [M'_{Ce}], \quad (16)$$

the simplified electroneutrality condition will be written as

$$[V_O^{\cdot\cdot}] = \frac{1}{2}[M'_{Ce}] \quad (17)$$

Having substituted the right-hand side of relation (17) into Eqn (15), we arrive at the dependence of electron carrier concentration on partial oxygen pressure for doped CeO_2 in the form

$$[Ce'_{Ce}] = 0.5^{-1/2}K_r(T)^{1/2}[M'_{Ce}]^{-1/2}p_{O_2}^{-1/4} \quad (18)$$

The cerium reduction reaction constant (invariable at a given temperature) is

$$K_r(T) = [Ce'_{Ce}]^2[V_O^{\cdot\cdot}]^{-1/2}p_{O_2}^{-1/4} \quad (19)$$

Since $x = [Ce'_{Ce}]/2$, at a specified temperature,

$$K'_r = [2x]^2p_{O_2}^{1/2} \text{ and } x \propto p_{O_2}^{1/2} \quad (20)$$

In addition,

$$K'_r = \exp\left(\frac{\Delta S_r}{k}\right)\exp\left(-\frac{\Delta H_r}{kT}\right) \quad (20a)$$

where ΔS_r and ΔH_r are, respectively, the entropy and enthalpy of cerium reduction reaction. On the assumption that ΔS_r is constant in the temperature range under consideration, the temperature dependence of the equilibrium constant can be written as

$$K'_r = K_r^0\exp\left(-\frac{\Delta H_r}{kT}\right) \quad (21)$$

Gorelov *et al.*[129] showed that the behaviour of partial electronic conductivity in GDC20 in the region of moderate deviations from stoichiometry is adequately described by the dependence on $p_{O_2}^{-1/4}$ (Fig. 11 *a*). On the assumption that the plateau in the dependence of total conductivity corresponds to ionic conductivity (the electronic contribution is negligible), the electronic conductivity can be calculated by the difference method. The authors suppose that this method is sufficiently correct at a high dopant concentration and, with allowance for the mobility of electrons and

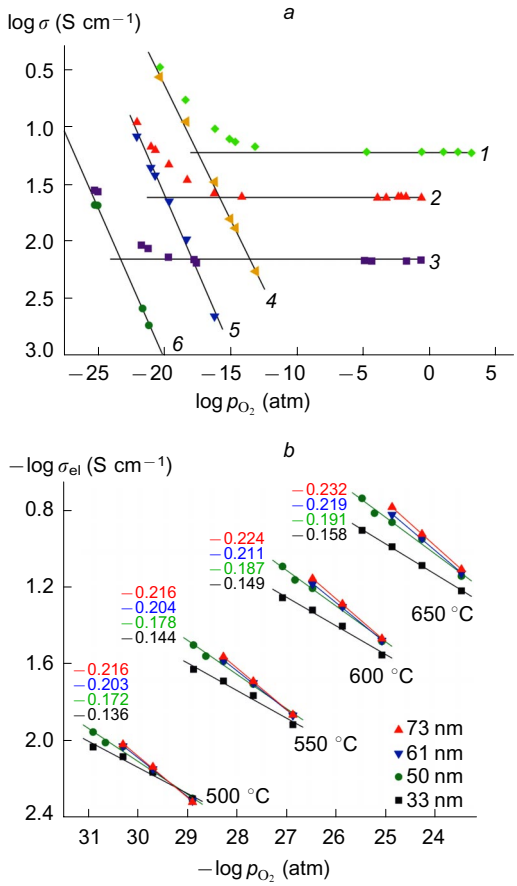


Figure 11. (*a*) Dependences of the ionic (*1* – *3*) and electronic (*4* – *6*) conductivities of GDC20 on the partial oxygen pressure at temperatures of 700, 800, and 900 °C, respectively,[129] and (*b*) dependences of the electronic conductivity of SDC15 (grain size 33 – 73 nm) on the partial oxygen pressure in the temperature range of 500 – 650 °C (the negative numbers are the slopes of the corresponding dependences).[131] Figure *a* is published with permission of Springer Nature. Figure *b* is published with permission of IOP Publishing.

oxygen vacancies, does not introduce large errors into the calculation of electronic conductivity. The values of critical partial oxygen pressure $p^*_{O_2}$ (at which $\sigma_{ion} = \sigma_{el}$) for GDC20 were found to be $10^{-22.5}$, 10^{-20}, and 10^{-18} atm at 600, 700, and 800 °C, respectively. Since the oxygen vacancy concentration also depends on partial oxygen pressure, according to Vegard's law, this leads to a $p_{O_2}^{-1/4}$-like dependence of the lattice parameters; the dependence of the chemical expansion of GDC20, which was studied by the authors by dilatometry, correlates with the dependence of electrical conductivity on $p_{O_2}^{-1/4}$ (Ref. 129). The expansion of $Ce_{1-y}Gd_yO_{2.0-0.5y-\delta}$ at different partial oxygen pressures was also studied using high-temperature XRD by Wang *et al.*[130] It was shown that the anomalous expansion caused by the reduction and corresponding occurrence of oxygen vacancies is observed for doped compositions at temperatures > 600 °C, whereas for CeO_2 this expansion is observed in the range > 700 °C, which is due to the higher binding energy of oxygen ions in undoped CeO_2.

The difference method was also used to obtain data on the electronic conductivity of nanoscale (33 – 73 nm) $Ce_{0.85}Sm_{0.15}O_{1.925}$ (SDC15) by Souza *et al.*[131] (Fig. 11 *b*). The authors noted that a decrease in the electrolyte grain

Table 2. Dependence of the critical partial oxygen pressure on the dopant concentration for solid electrolyte $Ce_{1-x}Gd_xO_{2-\delta}$.[133]

Dopant concentration (mol.%)	$p^*_{O_2}$ (atm) at temperature (°C)			
	700	750	800	850
10	1.3×10^{-16}	2.53×10^{-15}	2.43×10^{-14}	3.56×10^{-13}
20	1.24×10^{-18}	3.92×10^{-17}	9.2×10^{-16}	1.73×10^{-14}
30	3.16×10^{-18}	5.6×10^{-17}	8.5×10^{-16}	9.0×10^{-15}
40	9.3×10^{-18}	8.8×10^{-17}	6.3×10^{-16}	3.85×10^{-15}
50	1.46×10^{-15}	1.38×10^{-14}	1.12×10^{-13}	6.5×10^{-13}

size changes the slope of the dependence $\log\sigma_{el}-\log p_{O_2}$ from 1/4 to −1/6, as for undoped CeO_2; however, there is not any significant shift of $p^*_{O_2}$ to the low-pressure range. In the study by Pikalova,[132] the maximum value $p^*_{O_2}=3.98\times10^{-22}$ atm was obtained for $CeO_2-SmO_{1.5}$ at a dopant concentration of 30 mol.%, for $Ce_{0.8}Sm_{0.2}O_{1.9}$ (SDC20) at 750 °C the corresponding value was found to be 2.76×10^{-21} atm.

The concentration and temperature dependences of $p^*_{O_2}$ for the solid electrolyte $Ce_{1-x}Gd_xO_{2-\delta}$, found by Kudo and Obayashi [133] using the emf method are listed in Table 2. For this oxide system the minimum critical partial pressure in the medium-temperature range is obtained at a dopant concentration of 20 mol.% (1.24×10^{-18} atm, 700 °C); at high temperatures, the minimum value of $p^*_{O_2}$ corresponds to a dopant concentration of 40 mol.%.

Navarro *et al.*[134] compared the values of electronic conductivity found by the ion-blocking method for GDC10 and GDC20, as well as for CeO_2 doped with 18 mol.% gadolinium and 2 mol.% praseodymium. At 800 °C, the σ_{el} values (approximated to $p_{O_2}=1$ atm), were found to be 2.0×10^{-4}, 2.9×10^{-4}, and 1.5×10^{-4} S m^{-1}, respectively. Measurements of the dependence $\sigma_{tot}-p_{O_2}$ by the difference method yielded σ_{el} values equal to 4.4×10^{-4} (GDC10) and 1.7×10^{-4} (GDC20). The authors explained the difference in the results obtained by different methods by the fact that real systems exhibit deviations from the $p_{O_2}^{-1/4}$ dependence, because the vacancy concentration depends on the partial oxygen pressure.

Duncan and Wachsman [135] developed a generalized model of the functional dependence of defect concentration on the partial oxygen pressure for mixed conductors with fluorite and perovskite structures. Instead of a pair of dominant defects in the ranges of high, low, and intermediate partial oxygen pressures, considered in the simplifications according to the Brouwer method, the authors took into account defect triads in the electroneutrality equation and thus obtained a continuous description of conductivity dependences. The model was successfully applied when considering some experimental data on conductivity and non-stoichiometry.

The stability of electrolytes with a number of trivalent dopants (20 mol.%) and divalent calcium (10–50 mol.%) to reduction was investigated (using emf and thermogravimetry methods) by Arai and co-workers [136–138] (Fig. 12 *a*). According to their data, SDC20 is the most stable system with a trivalent dopant among the investigated ones ($p^*_{O_2}\approx9\times10^{-14}$ atm at 800 °C [136]). Pikalova *et al.*,[21,132] who used experimental dependences $\sigma_{tot}-p_{O_2}$ and the difference method, also obtained the minimum $p^*_{O_2}$ value for SDC20 (2.76×10^{-21} and 3.87×10^{-16} atm at 750 and

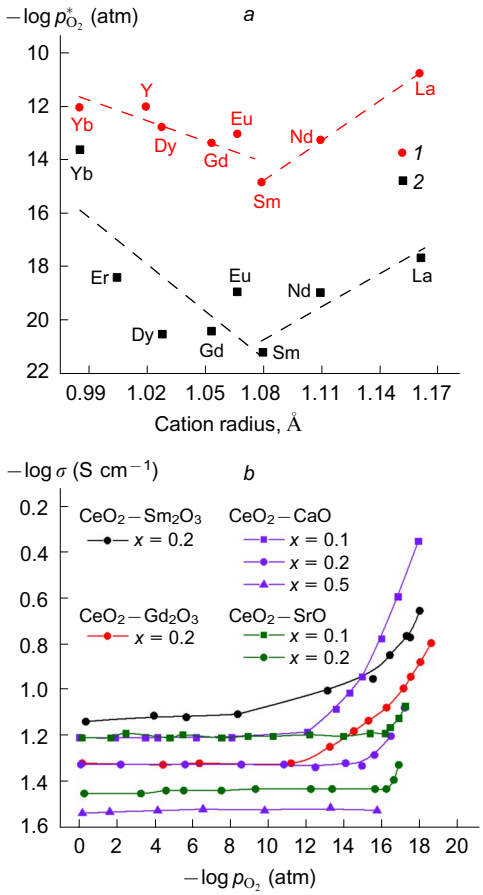


Figure 12. (*a*) Dependences of the critical partial oxygen pressure $p^*_{O_2}$ on the dopant cation radius for electrolytes $Ce_{0.8}M_{0.2}O_{2-\delta}$ at 800 (*1*) [136] and 750 °C (*2*) [132] and (*b*) dependences of conductivity on the partial oxygen pressure: $Ce_{0.8}M_{0.2}O_{2-\delta}$ (M = Sm, Gd),[136] $Ce_{1-x}Ca_xO_{2-\delta}$ (Ref. 137), and $Ce_{1-x}Sr_xO_{2-\delta}$ (Ref. 138). The figure was compiled by the authors based on the data of the aforementioned publications.

900 °C, respectively). The values of $p^*_{O_2}$ for CeO_2 doped with divalent cations are on the whole higher than those found for trivalent dopants (Fig. 12 *b*). For example, for $Ce_{0.8}Ca_{0.2}O_{1.8}$ and $Ce_{0.9}Sr_{0.1}O_{1.9}$ (compositions within dopant solubility limits), $p^*_{O_2}\approx10^{-17}$ atm at 800 °C. At higher dopant contents the shift of $p^*_{O_2}$ towards low partial oxygen pressures is most likely due to the grain boundary effects.

The data of theoretical calculations of $p^*_{O_2}$ by Steele [113] exceed the experimental results obtained in a number of the aforementioned studies. The calculated values of critical partial pressure for GDC electrolytes with dopant concentrations of 10 and 20 mol.% are almost the same in the temperature range of 800–1000 °C (*e.g.*, 3.51×10^{-17} and 6.63×10^{-17} atm at 800 °C), whereas with a decrease in temperature the difference increases, which is indicative of higher stability of GDC10 (1.49×10^{-30} atm) in comparison with GDC20 (1.51×10^{-27} atm) at 500 °C. The values of reduction reaction enthalpy for CeO_2, GDC10, and GDC20, calculated from the non-stoichiometry data [139,140], are, respectively, 9.2–9.8, 8.5–9.1, and 7.9–8.1 eV mol^{-1}; *i.e.*, Ce^{4+} is reduced more intensively with an increase in the Gd^{3+} content.

Electrochemical studies of a number of SOFCs with electrolytic membranes based on doped CeO_2 and different cathodes and anodes showed that the specific power

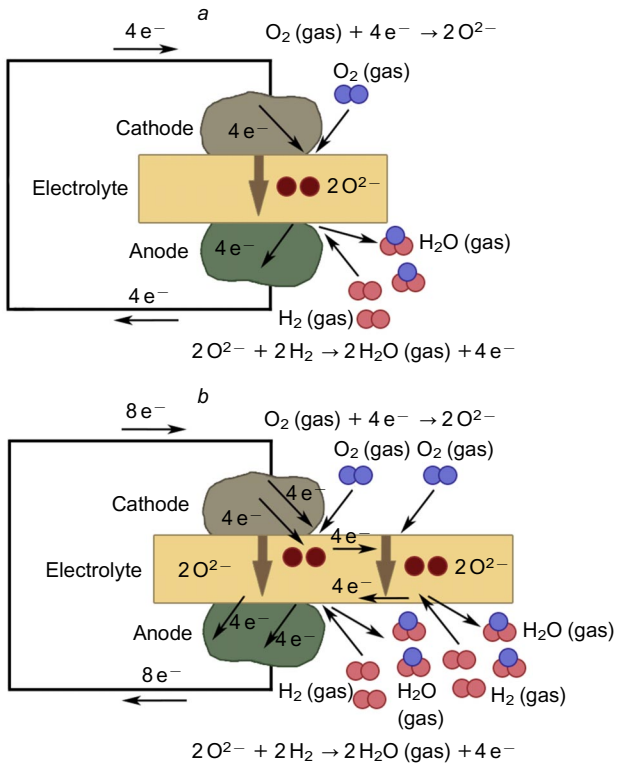


Figure 13. Schematic diagrams of operation of SOFCs (*a*) with a unipolar oxygen ionic conductor and (*b*) with an electrolyte having mixed conductivity. The figure is compiled by the authors based on the data of Ref. 142.

obtained at 700 °C is equivalent to the specific power generated by similar SOFCs with an YSZ electrolytic membrane at 900 °C.[141] The electron current in electrolyte depolarizes electrodes, thus facilitating expansion of the electrochemical reaction zone.[142] This effect manifests itself in the difference in the operation mechanisms of SOFCs based on a unipolar oxygen-ion conductor and SOFCs with an electrolyte having mixed conductivity (mixed ionic–electronic conductor (MIEC) (Fig. 13).

The presence of electron current leads to a decrease in the open circuit value (OCV_{MIEC}) according to the equation

$$OCV_{MIEC} = E_{th}\left(\frac{R_{el}}{R_{ion} + R_{\eta} + R_{el}}\right) \qquad (22)$$

where R_{el} and R_{ion} are, respectively, the resistances to electron and ion currents and R_Z is the polarization resistance; in correspondence with the Nernst equation,

$$E_{th} = \frac{kT}{4e}\ln\left(\frac{p_{O_2}^{(2)}}{p_{O_2}^{(1)}}\right) \qquad (23)$$

where 4e is the total transferred charge and $p_{O_2}^{(1)}$ and $p_{O_2}^{(2)}$ are the partial oxygen pressures in the cathode and anode channels, respectively.

A method for calculating the thermodynamic efficiency of SOFCs with an electrolytic membrane having mixed ionic–electronic conductivity was proposed and studied by Godickemeier and Gauckler.[141, 143] Expressions were derived for electron and ion currents through an MIEC cell, including the contribution of mixed electrolyte conductivity and the electrode (cathode and anode) overvoltage. The calculations were based on the results of Riess,[144] who solved the one-dimensional equation for the electron distribution in MIEC electrolyte using the electroneutrality condition and local thermodynamic equilibrium. The expressions for the electrode overvoltage are based on the Butler–Volmer equation. Experiments on a single SOFC with an SDC20-based electrolyte and $La_{0.94}Sr_{0.19}CoO_{3-\delta}$ (LSC) cathode and $Ni-Ce_{0.9}Ca_{0.1}O_{1.9-\delta}$ anode were performed to determine the necessary model parameters, specifically:

— dependences of the electronic and ionic conductivity on the partial oxygen pressure;

— electrochemical parameters of the cathode and anode overvoltage at different current densities and different temperatures;

— geometric parameters of the cell: electrolyte thickness and cross-sectional area.

The authors introduced the following parameters of SOFC cell efficiency:

— voltage efficiency (ratio of the voltage across the cell to the theoretical Nernst voltage under specified conditions);

— current or Faraday efficiency, defined as the ratio of the total current to the ion current.

The total SOFC cell efficiency was determined as the product of these parameters. The dependences of the cell efficiency and specific power density at a chosen electrolyte thickness (240 μm) and different temperatures (600, 700, 800 °C) were calculated. The dependences were non-monotonic, with maxima at different current densities. High efficiency and specific power were implemented in a narrow range of current densities. Dependences of the cell specific power and efficiency on the electrolyte thickness were presented; these plots could not be explicitly fitted by any analytical curves. As an example of optimized SOFC design, we report below the values of thermodynamic efficiency (E) and maximum attainable specific power density (N_{max}) for an SOFC with an SDC20-electrolyte, calculated based on the experimental dependences of the electrolyte conductivity on p_{O_2} at the aforementioned temperatures:

T, °C	600	700	800
E (%)	60	57	50
N_{max}, W cm^{-2}	0.09	0.24	0.45

For practical applications, the fuel utilization efficiency must be no less than 80%.[13] Thus, temperature must be reduced; however, to this end, one should modify significantly the electrical properties of electrolytic membrane, reduce the ohmic loss by decreasing the membrane thickness, and diminish the polarization of electrodes. Within the approach developed by Godickemeier and Gauckler,[143] the current–voltage characteristics and power of an SOFC with a thin-film (25 μm) MIEC electrolyte GDC10 were calculated by Steele.[113] It was shown that, with a decrease in temperature to 500 °C, OCV ≈ 1 V and power density of 400 mW cm^{-2} can be achieved theoretically, provided that the polarization resistance of anode and cathode does not exceed 0.2 Ω cm^2.

An analysis of the results of studying the structure and electrical properties of solid solutions showed that successful application of CeO_2-based materials in the SOFC technology is hindered by the following factors:

1) doping fluorite structure with a number of elements leads to the formation of a rather large number of vacan-

cies; beginning with a certain doping level (~10 – 20 mol.%), one can observe the formation of local ordered structures, due to which the ionic conductivity decreases;

2) the electrolyte microstructure and purity of grain boundaries, which form a barrier for ion transport even in materials with a minimum amount of impurities, play an important role; the application of CeO_2-based nanomaterials is limited by the occurrence of a large contribution of electronic conductivity, as compared with microscale materials;

3) the electronic conductivity, arising in materials in a reducing atmosphere, decreases the output of SOFCs based on CeO_2 electrolytes; the lattice changes caused by the reduction reaction may lead to mechanical destruction of the electrolyte.

Different approaches have been proposed to solve the aforementioned problems: structural modification of electrolytes, aimed at increasing the ionic conductivity and expanding the electrolytic domain; formation of composite materials; and design of barrier layers serving to block the electron current in the electrolyte. These methods are considered in the sections below.

3. Modification of the bulk properties of electrolytes based on CeO_2

3.1. Criteria of choosing elements for co-doping in order to improve the electrical and electrolytic properties of CeO_2 electrolytes

One can select several trends in structural modification of CeO_2-based solid electrolytes that are aimed at increasing the ionic conductivity, in particular, different co-doping strategies. The first trend is related to the concept of 'ideal' dopant with a critical ionic radius, whose introduction into a fluorite lattice causes neither expansion nor compression.[58, 59] Since the binding energy of defects depends on both their Coulomb attraction and the elastic strain field arising around a local structure, the maximum ionic conductivity can be reached by reducing the influence of these defects, caused by the difference in the ionic radii of the host and dopant ions.[98] As a criterion, the authors of a majority of experimental studies aimed at validating the critical radius concept chose the value $r_c = 1.038$ Å.[58] In particular, Omar *et al.*[145] studied electrolytes from the series $Lu_xNd_yCe_{1-x-y}O_{2-\delta}$ ($x + y = 0.05$, 0.10, 0.15, and 0.20). Dopants were chosen for each concentration so as to implement the equality $r_c = 1.038$ Å. With dopants chosen in this way, the positive elastic stresses formed by large Nd^{3+} ions are compensated with the negative elastic stresses formed by Lu^{3+} ($r = 0.977$ Å). However, the results obtained showed the conductivity of co-doped system to be much lower than the conductivity of $Nd_yCe_{1-y}O_{2-\delta}$ and only slightly exceed the conductivity of the $Lu_xCe_{17x}O_{2-\delta}$ system in the entire range of dopant concentrations.

The electrical properties of SDC20 with Y^{3+} and Ca^{2+} ions as co-dopants (for which the average dopant radius approaches r_c) were investigated in several studies.[146 – 148] Dudek[146] obtained maximum values of grain conductivity for $Ce_{0.8}Sm_{0.1}Y_{0.1}O_{1.9}$ and $Ce_{0.8}(Sm_{0.5}Ca_{0.5})_{0.2}O_2$, which were found to be, respectively, 8.16 and 7.31 mS cm^{-1} at 600 °C. Maximum grain boundary conductivity, almost equal to the bulk conductivity in the low-temperature range (7.62 mS cm^{-1} at 600 °C) and exceeding it in the high-temperature range, was also observed for $Ce_{0.8}Sm_{0.1}Y_{0.1}O_{1.9}$,. The electromotive force of the cell based on this electrolyte corresponds to the theoretical value; however, the study was performed in a narrow pressure range: from 0.21 to 10^{-5} atm. The application of sol – gel synthesis of $Ce_{0.8}Sm_{0.1}Y_{0.1}O_{1.9}$ made it possible to increase the electrical conductivity of electrolyte to 12.9 mS cm^{-1}.

A positive effect of co-doping with gadolinium and calcium on the grain boundary conductivity due to the neutralization of SiO_2-containing impurities was demonstrated in a number of studies.[149 – 152] In particular, a significant decrease in the grain boundary resistance upon introduction of CaO into $Ce_{0.85}Ge_{0.15}O_{1.925}$ (GDC15), containing 500 ppm SiO_2 (2.80 – 3.50 kΩ cm at 300 °C as compared with c 746.7 kΩ cm for the basic composition), was observed by Cho *et al.*[151] Even a greater effect of decreasing the grain boundary resistance (to 0.90 – 1.97 kΩ cm) was observed in the case of introduction of 1 mol.% SrO into GDC15.[153] When studying the $Ce_{0.8}(Sm_{17x}Ca_x)_{0.2}O_2$ system, Pikalova *et al.*[152, 154] found the maximum conductivity to be at $x = 0.2$ (13.71 mS cm^{-1} at 600 °C), mainly due to the increase in the grain boundary conductivity. However, despite the fact that the values $p^*_{O_2}$ for the CeO_2-CaO system are smaller than for the systems with trivalent dopants (see Fig. 12), narrowing of the electrolytic domain and increase in $p^*_{O_2}$ were observed on doping SDC20 with calcium. In particular, for $x = 0$, 0.2, and 0.4, the $p^*_{O_2}$ values were found to be, respectively, 2.76×10^{-21}, 5.05×10^{-18}, and 1.31×10^{-18} atm at 750 °C.[152]

Table 3. Structural, electrical, and electrolytic properties of electrolytes based on CeO_2.[154, 155]

Electrolyte	a, Å (see [a])	r_d, Å	σ, mS cm^{-1} (750 °C)	E_a, eV (350 – 600 °C)	E_a, eV (600 – 900 °C)	$p^*_{O_2}$, atm (750 °C)
CeO_2	5.4140	–	–	–	–	–
$Ce_{0.8}Sm_{0.2}O_{2-\delta}$	5.4363	1.079	50.23	0.88	0.76	9.05×10^{-22}
$Ce_{0.8}Nd_{0.2}O_{2-\delta}$	5.4507	1.109	55.86	0.88	0.79	7.50×10^{-20}
$Ce_{0.8}La_{0.2}O_{2-\delta}$	5.4752	1.160	35.98	0.86	0.80	2.24×10^{-18}
$Ce_{0.8}Dy_{0.2}O_{2-\delta}$	5.4114	1.027 [b]	25.54	0.97	0.91	3.49×10^{-21}
$Ce_{0.8}Gd_{0.2}O_{2-\delta}$	5.4262	1.053	17.13	0.93	0.92	3.36×10^{-19}
$Ce_{0.80}(Y_{0.5}Dy_{0.5})_{0.20}O_{2-\delta}$	5.4135	1.023 [b]	4.79	1.01	1.21	3.73×10^{-16}
$Ce_{0.80}(Sm_{0.5}Y_{0.5})_{0.20}O_{2-\delta}$	5.4235	1.049	13.63	0.96	1.10	2.20×10^{-16}
$Ce_{0.80}(Gd_{0.5}Y_{0.5})_{0.20}O_{2-\delta}$	5.4178	1.036 [b]	16.35	1.00	1.09	1.21×10^{-17}
$Ce_{0.80}(Sm_{0.5}Nd_{0.5})_{0.20}O_{2-\delta}$	5.4377	1.094	37.18	0.86	0.80	2.40×10^{-18}
$Ce_{0.80}(La_{0.5}Dy_{0.5})_{0.20}O_{2-\delta}$	5.4404	1.094	38.28	0.86	0.83	2.87×10^{-17}

$r_d(Y) = 1.019$ Å. [a] Unit cell parameter. [b] These r_d values are most close to r_c.

Comparative studies of the electrical properties of some electrolytes with one ($Ce_{1-x}M_xO_{2-\delta}$) and two [$Ce_{1-x}(M_{0.5}M'_{0.5})_xO_{2-\delta}$ ($x = 0.1-0.2$)] rare-earth dopants[154,155] showed that the electrical conductivity of co-doped systems is lower than that of basic ones (Table 3). No positive effect of co-doping on the electrolytic properties were found: the $p^*_{O_2}$ values for co-doped systems turned out to be larger than for basic electrolytes; co-doping with Y^{3+} ions led to the most pronounced narrowing of the electrolytic domain. No correlation between the conductivity maximum and electrolytic properties was observed when the dopant radius (or the average co-doping radius) approached the values of critical radii (1.038 and 1.024 Å). The found maxima of electrical and electrolytic properties for $Ce_{17x}M_xO_{2-\delta}$ correspond to the established tendencies and values for CeO_2 electrolytes (see Sections 2.2.2 and 2.3).

Since Gd^{3+} and Sm^{3+} are the most widespread and well-studied dopants for CeO_2, it is of interest to investigate their synergistic effect on the electrolyte properties.

Wang *et al.*[156] studied systematically the $Ce_{1-x}Gd_{x-y}Sm_yO_{2-0.5x}$ system, where $x = 0.15$ or 0.20; ($0 \leqslant y \leqslant x$). It was shown that, at a dopant content of 15 mol.% (total value), the electrical conductivity of three-component systems exceeds that of two-component ones. In particular, at 700 °C the electrical conductivity of $Ce_{0.85}Gd_{0.1}Sm_{0.05}O_{2-\delta}$ solid solution reached 46 mS cm^{-1}, which is superior than the best results obtained for binary systems with gadolinium (31.6 mS cm^{-1})[157] or samarium (41 mS cm^{-1}).[158] With an increase in the total dopant concentration to 20 mol.%, an increase in the electrical conductivity under co-doping was observed in the low-temperature range (< 500 °C), which may indicate a decrease in the formation efficiency of cation–vacancy associates. At the same time, in the high-temperature range, the electrical conductivity of a ternary system is the arithmetic mean of the values obtained for binary systems. Coles-Aldridge and Baker[159] observed a maximum of ionic conductivity for $Ce_{0.8}Sm_{0.1}Gd_{0.1}O_{1.9}$, equal to 18 mS cm^{-1} at 600 °C.

A comparative study of the electrical conductivity of GDC10 and systems with two ($SmO_{1.5}$ and $YO_{1.5}$) and four ($SmO_{1.5}$, $YO_{1.5}$, $DyO_{1.5}$ and $NdO_{1.5}$) co-dopants was performed[92] to establish the influence of multiple co-doping on the increase in the entropy of the system and decrease in the formation rate of vacancy associates. For the $(CeO_2)_{0.90}$. .$(GdO_{1.5})_{0.02}(SmO_{1.5})_{0.02}(YO_{1.5})_{0.02}(NdO_{1.5})_{0.02}(DyO_{1.5})_{0.02}$ system, the obtained values of electrical conductivity are 30% larger than for GDC10 (*e.g.*, at 600 °C they amount to 26.8 and 18.5 mS cm^{-1}, while at 800 °C they are 92.8 and 68.9 mS cm^{-1}, respectively). For the $Ce_{0.8}R_{0.2}O_{2-\delta}$ system, where R is a mixture of ten rare-earth elements from samarium to lutetium, the electrical conductivity is 20% higher than for the basic GDC20 composition; at 800 °C it is equal to 99.1 mS cm^{-1} and at 600 °C it is 25.0 mS cm^{-1}. The authors showed that the maximum electrical conductivity for two-component systems was obtained at a total dopant concentration of 15–16 mol.%; for multicomponent systems, the total dopant content of 10–12 mol.% is optimal for attaining the best electrical properties. With a further increase in the dopant content, the synergistic effect of co-doping was observed only at low temperatures, as well as for $Ce_{0.8}Gd_{0.2-x}Sm_xO_{2-\delta}$.[92]

The choice of dopants based on theoretical calculations of the binding energy during formation of local structures lies in the basis of another trend in the field of designing multicomponent systems based on CeO_2. In this case, the main purpose is to obtain the maximum concentration of possible sites with the same binding energy for oxygen diffusion. This energy equalization should attenuate the formation of the so-called vacancy traps and, correspondingly, exclude the formation of local structures. According to the data of Andersson *et al.*,[91] an ideal dopant with minimum cation–vacancy binding energy in the NN and NNN coordination shells should have an ionic radius close to that of Pm^{3+} (1.093 Å). The application of Pm^{3+} as a dopant is limited by its radioactivity. Co-doping with Sm^{3+} and Nd^{3+} at a molar ratio of 1 : 1 yields an average ionic radius maximally close to that of Pm^{3+} and a nearly minimum value of binding energy. Omar *et al.*,[145,160] who studied the series $Ce_{1-x}Sm_{x/2}Nd_{x/2}O_{2-\delta}$, showed that the maximum of ionic conductivity at 550 °C corresponds to $x = 0.15$; with a decrease in temperature, it shifts to lower concentrations. The ionic conductivity of $Ce_{0.85}Sm_{0.075}Nd_{0.075}O_{2-\delta}$ is 30% higher than the conductivity of $Ce_{0.9}Gd_{0.1}O_{2-\delta}$ (Ref. 157); it exceeds also the conductivity of basic electrolytes. The maximum values of electrical conductivity among the electrolytes doped with two REEs, obtained by Pikalova *et al.*[154] (see Table 3), refer to the samples with Sm and Nd dopants, or with La and Dy dopants taken in a molar ratio of 1 : 1, with an average dopant radius of ~1.094 Å; this is consistent with the concept of binding energy minimization. The associate formation enthalpy for $Ce_{1-x}Sm_{x/2}Nd_{x/2}O_{2-\delta}$ amounts to 0.02–0.05 eV,[145] whereas the minimum value for $Ce_{1-x}Nd_xO_{2-\delta}$, obtained by Stephens and Kilner[110] at $x = 0.3$, is ~ 0.08 eV. Li *et al.*,[161] who investigated the electrical properties of $Ce_{0.9}(Sm_xNd_{1-x})_{0.1}O_{2-\delta}$ ($x = 0$, 0.5, 1) and $Ce_{1-x}(Sm_{0.5}Nd_{0.5})_xO_{2-\delta}$ ($x = 0.05$, 0.10, 0.15, 0.20), observed a maximum of grain conductivity, 16 mS cm^{-1}, at 550 °C, dopant ratio of 1 : 1, and total dopant concentration of 10 mol.%. The positions of the maxima of grain boundary conductivity and the minimum of activation energy for $Ce_{0.9}(Sm_{0.5}Nd_{0.5})_{0.1}O_{2-\delta}$ are similar to those for the basic electrolyte $Ce_{1-x}Nd_xO_{2-x/2}$ (NDC) and correspond to 10 mol.% [20 mol.% for $Ce_{1-x}Sm_xO_{2-x/2}$ (SDC)]. The authors explained this fact by the elevated concentration of Nd^{3+} cations in the space-charge region due to the Sm^{3+} precipitation on grain boundaries, as was confirmed by the XPS method. For the co-doped system, the ΔH_m value is larger than for the conventional gadolinium-doped electrolytes (which served as a reference in almost all studies); however, the sum $\Delta H_m + \Delta H_a$ is smaller. This circumstance significantly reduces the conductivity activation energy at low temperatures in the systems considered here and other co-doped systems.[92,156]

The effect of increased ionic conductivity due to the suppression of the local ordering of oxygen vacancies by co-doping (which leads to the formation of local lattice strain because of the difference in the radii of REE dopants) is being discussed.[162–164] Nevertheless, it was confirmed by various research teams for a number of systems with such co-dopants as Nd–Dy,[165] Gd–Y,[166] La–Sm,[167] Gd–Nd,[168] Pr–La,[169] Pr–Nd,[170] Pr–Gd[171–173] and La–Dy.[174] The decrease in the formation efficiency of C-type structures at high dopant contents was proven experimentally, *e.g.*, by Artini *et al.*,[175] who applied synchrotron radiation diffraction analysis. Therefore, the possibilities of doping and obtaining a higher ionic conductivity by increasing the number of isolated vacancies are

expanded. However, it should be noted that there are very little data on the electrolytic domain of CeO_2 doped with two and more REEs, and this line of research may be rather promising.

3.2. Co-doping with REE and alkaline-earth or alkali metal cations. Effective index

Mori *et al.*[176, 177] proposed a strategy for improving the ionic conductivity of CeO_2-based materials in both reducing and oxidizing atmospheres, based on the effective-index theory. The effective index (EI) is determined from the ratio of the host and dopant ionic radii and the number of oxygen vacancies formed upon doping,

$$\mathrm{EI} = \frac{r_{\mathrm{cat}}}{r_{\mathrm{eff\,O}}}\,\frac{r_{\mathrm{d}}}{r_{\mathrm{h}}} \tag{24}$$

where r_{cat} is the average ionic radius of cation; r_{d} is the average ionic radius of dopant; r_{h} is the ionic radius of Ce^{4+}; and $r_{\mathrm{eff\,O}}$ is the effective ionic radius of oxygen, which is determined by the expression

$$r_{\mathrm{eff\,O}} = 1.4\left(\frac{2-\delta}{2}\right) \tag{25}$$

Here, 1.4 (Å) is the ionic radius of oxygen in CeO_2 and δ is the level of oxygen vacancies.

If the coordination number in the fluorite structure is 8, the ratio $r_{\mathrm{c}}/r_{\mathrm{eff\,O}}$ approaches unity, and, if the ratio $r_{\mathrm{d}}/r_{\mathrm{h}}$ is close to unity under these conditions, the cation – vacancy binding energy in the fluorite structure is minimized. It was shown by transmission electron microscopy that oxygen vacancies become less ordered in solid solutions with a large effective index (Fig. 14 *a*,*b*).[177] In particular, ordered regions up to 20 nm in size (shown by arrows in Fig. 14 *a*) were observed for $La_{0.175}Ce_{0.825}O_{1.912}$, whereas the size of ordered regions for $(La_{0.8}Sr_{0.2})_{0.175}Ce_{0.825}O_{1.895}$ and $(La_{0.75}Sr_{0.2}Ba_{0.05})_{0.175}Ce_{0.825}O_{1.891}$ did not exceed 3 – 5 nm. The decrease in the degree of vacancy ordering manifests itself in an increase in ionic conductivity (Fig. 14 *c*). The effect of suppressing the formation of cation – oxygen vacancy associates upon multidoping makes it possible to shift the maximum of electrical conductivity upon doping with trivalent dopants up to their content of 35 mol.%.[178]

We should also note the following effect occurring upon co-doping with cations of alkali and alkaline-earth metals: expansion of the electrolytic domain for the well-known simple solid solutions based on CeO_2 with trivalent dopants.[21, 132, 178 – 181] Co-doping with low-valence cations having a large radius causes lattice expansion and formation of additional migration channels for oxygen vacancies. For a majority of co-doped electrolytes, the ion transport number may reach 0.75 – 0.9 at a partial oxygen pressure of 10^{-21} atm.[180] Mori and Yamamura[179] showed that doping with Ca^{2+} or Cs^{+} cations (ionic radius 1.12 or 1.74 Å, respectively) increases significantly the oxygen ionic conductivity $Ce_{0.75}Sm_{0.25}O_{1.875}$ (SDC25) [at 800 °C, to 45.6 mS cm^{-1} for the basic electrolyte, to 109.5 mS cm^{-1} for $Ce_{0.75}(Sm_{0.5}Ca_{0.5})_{0.25}O_{2-\delta}$, and to 185.6 mS cm^{-1} for $Ce_{0.75}(Sm_{0.936}Cs_{0.06}Li_{0.004})_{0.25}O_{2-\delta}$]. The value of partial oxygen pressure characterizing the ionic conductivity plateau in the dependence of the total conductivity on p_{O_2} reached 10^{-7} atm at 800 °C for the basic electrolyte and 10^{-9} and 10^{-12} atm for co-doped electrolytes. It was shown[179,181] that the use of electrolytes co-doped with

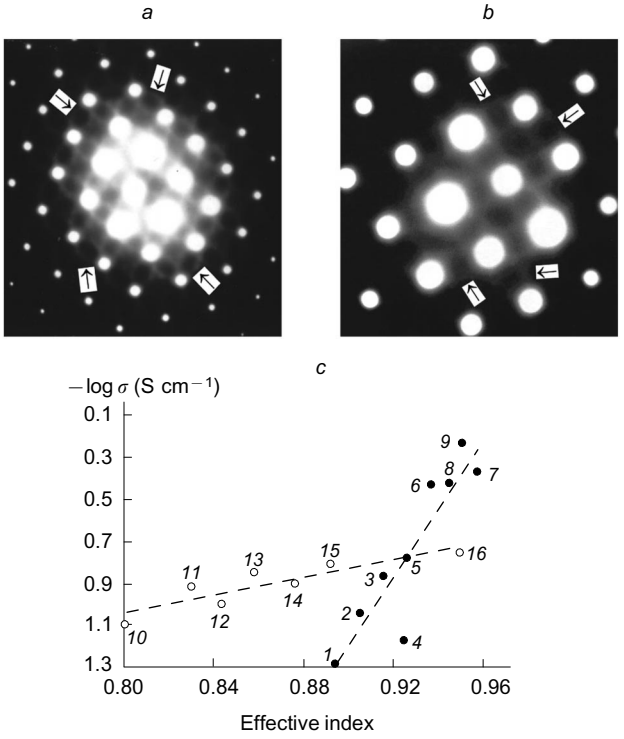


Figure 14. TEM images of (*a*) $La_{0.175}Ce_{0.825}O_{1.912}$ and $(La_{0.75}Sr_{0.2}Ba_{0.05})_{0.175}Ce_{0.825}O_{1.891}$ (*b*)[177] (arrows indicate local ordering) and (*c*) correlation between the effective index and conductivity for solid electrolytes[132] at 800 °C: (*1*) $Ce_{0.875}La_{0.125}O_{1.937}$, (*2*) $Ce_{0.825}(La_{0.8}Sr_{0.2})_{0.175}O_{1.895}$, (*3*) $Ce_{0.825}L_{0.175}O_{1.912}$, (*4*) $Ce_{0.8}La_{0.2}O_{1.9}$, (*5*) $Ce_{0.825}(La_{0.9}Sr_{0.1})_{0.175}O_{1.895}$, (*6*) $Ce_{0.825}(La_{0.8}Sr_{0.2})_{0.175}O_{1.895}$, (*7*) $Ce_{0.825}(La_{0.6}Sr_{0.4})_{0.175}O_{1.895}$, (*8*) $Ce_{0.825}(La_{0.77}Sr_{0.2}Ba_{0.03})_{0.175}O_{1.891}$, (*9*) $Ce_{0.825}(La_{0.75}Sr_{0.2}Ba_{0.05})_{0.175}O_{1.891}$ (filled circles);[177] at 750 °C: (*10*) $Ce_{0.8}(Sm_{0.5}Y_{0.5})_{0.2}O_{2-\delta}$, (*11*) $Ce_{0.8}Sm_{0.2}O_{2-\delta}$, (*12*) $Ce_{0.8}(Sm_{0.5}Nd_{0.5})_{0.2}O_{2-\delta}$, (*13*) $Ce_{0.8}Nd_{0.2}O_{2-\delta}$, (*14*) $Ce_{0.8}(Gd_{0.75}Sr_{0.2}Ba_{0.05})_{0.2}O_{2-\delta}$, (*15*) $Ce_{0.8}(Sm_{0.75}Sr_{0.2}Ba_{0.05})_{0.2}O_{2-\delta}$, (*16*) $Ce_{0.8}(La_{0.75}Sr_{0.2}Ba_{0.05})_{0.2}O_{2-\delta}$ (open circles). Figures *a* and *b* are published with permission of IOP Publishing.

Table 4. Experimental values of electrical conductivity in air and critical partial pressure, obtained by the difference method, for solid solutions based on CeO_2, and calculated values of effective index.[21, 132]

Composition	σ, S cm^{-1} (900 °C)	$p^*_{O_2}$, atm (750 °C)	EI
$Ce_{0.8}Sm_{0.2}O_{2-\delta}$	0.124	2.76×10^{-21}	0.830
$Ce_{0.8}Nd_{0.2}O_{2-\delta}$	0.145	7.50×10^{-20}	0.858
$Ce_{0.8}La_{0.2}O_{2-\delta}$	0.098	2.20×10^{-18}	0.906
$Ce_{0.8}(Sm_{0.8}Ca_{0.2})_{0.2}O_{2-\delta}$	0.155	5.05×10^{-18}	0.846
$Ce_{0.8}(Sm_{0.5}Ca_{0.5})_{0.2}O_{2-\delta}$	0.127	1.31×10^{-18}	0.872
$Ce_{0.8}(Sm_{0.8}Sr_{0.2})_{0.2}O_{2-\delta}$	0.162	3.30×10^{-19}	0.873
$Ce_{0.8}(Sm_{0.7}Sr_{0.3})_{0.2}O_{2-\delta}$	0.151	9.98×10^{-23}	0.895
$Ce_{0.8}(Sm_{0.5}Y_{0.5})_{0.2}O_{2-\delta}$	0.072	2.20×10^{-16}	0.802
$Ce_{0.8}(La_{0.5}Dy_{0.05})_{0.2}O_{2-\delta}$	0.111	1.21×10^{-17}	0.843
$Ce_{0.8}(Sm_{0.5}Nd_{0.5})_{0.2}O_{2-\delta}$	0.100	2.40×10^{-18}	0.844
$Ce_{0.8}(Gd_{0.75}Sr_{0.2}Ba_{0.05})_{0.2}O_{2-\delta}$	0.126	5.05×10^{-18}	0.876
$Ce_{0.8}(Sm_{0.75}Sr_{0.2}Ba_{0.05})_{0.2}O_{2-\delta}$	0.161	2.76×10^{-23}	0.892
$Ce_{0.825}(La_{0.75}Sr_{0.2}Ba_{0.05})_{0.175}O_{2-\delta}$	0.172	6.58×10^{-24}	0.951

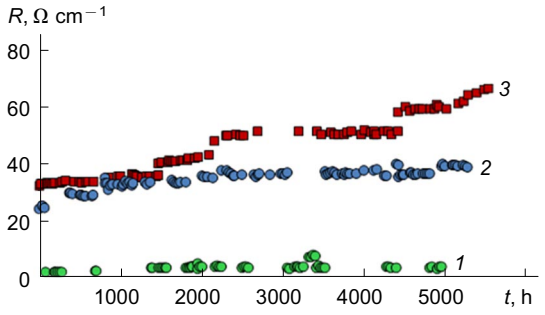


Figure 15. Time dependences of the resistivity (at 800 °C) of $Ce_{0.825}(La_{0.75}Sr_{0.2}Ba_{0.05})_{0.175}O_{2-\delta}$ in hydrogen atmosphere (*1*) and air (*2*) and $Ce_{0.8}Sm_{0.2}O_{2-\delta}$ in air (3). The figure is compiled by the authors based on the data of Ref. 132.

cations of different valences makes it possible to increase the output power of electrochemical cell by a factor of 2.5 – 3.

As was shown in our work [132] (Table 4), the proposed criterion of effective index can be used to make a preliminary choice of co-dopants. Studies of time stability showed that the electrolyte $Ce_{0.75}(Sm_{0.936}Cs_{0.06}Li_{0.004})_{0.25}O_{2-\delta}$ with an effective index maximally close to unity has an enhanced stability to ageing in comparison with the conventional electrolyte SDC20 in both oxidizing and reducing atmospheres (Fig. 15).[132]

Nevertheless, to validate the criterion, it is necessary to expand the series of compositions studied, apply different methods for investigating the electrolytic properties (emf method, Hebb – Wagner polarization method, *etc.*), and test electrolytes under SOFC working conditions.

3.3. Composite electrolytes based on doped CeO_2 and protonic conductors

During the last decade, the study of proton-conducting oxides has become a guideline in high-temperature electrochemistry all over the world.[182 – 185] The interest in these materials (in particular, cerates and barium cerate-zirconates) is related to their high conductivity and low activation energy at low temperatures (450 – 600 °C). In this context, it is of interest to consider the composite electrolytes based on protonic conductors and doped ceria, because the latter, in contrast, demonstrates high conductivity activation energy at relatively low temperatures. The effect of increasing OCV and output (in particular, at high temperatures) of an SOFC with an electrolytic membrane SDC20 and a thin (from 2 to 10 μm) $BaCe_{1-x}Sm_xO_{3-\delta}$ layer, obtained as a result of interaction between BaO and electrolyte during sintering (1500 – 1600 °C), was observed by Hirabayashi *et al.*[186] In particular, for an SDC20 electrolyte layer 0.5 mm thick, the maximum SOFC power was 170 mW cm^{-2} at 800 °C (195 mW cm^{-2} in the case of electrolyte with coating). At 900 °C the output of SOFC with SDC20 was reduced to 85 mW cm^{-2} because of the electronic-current short circuit, whereas a maximum value was observed for the electrolyte with a coating: 255 mW cm^{-2}. However, enhanced electrode polarization was observed; this effect is caused by the narrowing of electrochemical reaction zone from the anode side, with the electronic current blocked by a protonic layer.

In 2010 – 2011, three research teams, headed by Gopalan (India), L.Zhang (China), and Sun (China),[187 – 190] were involved in intense study of the properties of composite materials $BaCeO_3 - CeO_2$. A number of experiments were performed in Russia.[191, 192] An analysis of the data obtained revealed several tendencies:

— joint use of materials based on ceria and barium cerate leads to an increase in low-temperature conductivity,

— effect of electron current blocking in a composite electrolyte arises,

— OCV increases,

— the thermodynamic stability of electrolyte in reducing and CO_2 atmospheres increases.

Recently Sun *et al.*[193] obtained the highest power (352 mW cm^{-2}) at 700 °C for an SOFC with a composite electrolyte. The problem of strong polarization of electrodes contacting with composite electrolyte remains apparently unsolved, due to which higher powers cannot be generated at OCV close to those for proton-conducting electrolytes. Thus, to advance in this direction, it is necessary to combine the modification of electrolyte properties with search for compatible high-efficiency anode and cathode materials.

4. Technologies and methods for forming multilayer structures of SOFCs and thin-film electrolytes based on ceria

The variety of the methods applied in the SOFC technology to form functional (including multilayer) materials was presented in review,[194] where the design features of fuel cells are also described, the characteristics of applied materials (in particular, ceria-based electrolytes) are presented, generalized data on the output of SOFCs with thin-film electrolytes are reported, and the issues of SOFC commercialization and realization are discussed. A fairly complex technological equipment for carrying out pulsed laser deposition of thin films was described.[195] The issues of realization of ceramic technologies in the manufacture of thin-film (including multilayer) SOFC structures were discussed.[196] Advantages of electrophoretic deposition (EPD) from suspensions of weakly aggregated nanopowders, obtained by the laser evaporation – condensation method, were noted in the review by Pikalova and Kalinina.[197] Specific features of preparation of stable suspensions, choice of dispersion media, deposition regimes of the EPD method, and results of experimental and theoretical studies of the mechanisms of deposition in formation of SOFC electrolytic and electrode structures were considered by Kalinina and Pikalova.[198] Different debated models of the particle and ion transport and conjugated electrochemical reactions in a colloidal system, ways of carrying out EPD in aqueous media (using, in particular, dc and pulsed currents), and methods for controlling the dispersed composition of suspensions were described.[199] The key EPD parameters, as applied to SOFC fabrication, were presented in review by Aznam *et al.*[200]

Ceramic technologies have been widely used for a long time to form SOFC layers. These technologies include such methods as slip casting, screen printing, and calendering, which call for sintering at fairly high temperatures. This process may lead to the formation of nonconducting phases and delamination of SOFC multilayer structure.[201] Therefore, it is necessary to choose appropriate sintering regimes or use sintering additives (in particular, nanopowders) reducing the sintering temperature.

Oh *et al.*[202] noted the general problem of implementing thin-film technologies in SOFC: one must provide thermodynamic and thermomechanical stability of thin-film elec-

trolyte. Under SOFC operation conditions, NiO is reduced to Ni on the anode, and additional pores arise in it, which may violate the electrolyte integrity, especially in SOFCs with a carrier anode. At the same time, macroscopic defects can be formed in a thin-film electrolyte in which the grain size exceeds the electrolyte thickness or the size of pores in the electrode layer. To reduce the grain size, one must decrease the sintering temperature of SOFC functional layers. Using spin coating of suspensions of YSZ and GDC10 nanoparticles (with particle sizes of 20 and 10 nm, respectively), Oh *et al.*[202] obtained a bilayer gas-tight electrolyte YSZ/GDC10 with layers 100 and 400 nm thick, respectively, at a relatively low joint sintering temperature: no more than 1100 °C. The SOFC cell demonstrated a power density of 1.3 W cm^{-2} at 650 °C and an open circuit value of ~1.0 V.

The studies devoted to EPD of ceria-based electrolytes have been fragmentally presented in literature; they describe mainly the results of formation of single-layer CeO_2 electrolytes doped with samarium (SDC)[203, 204] and gadolinium (GDC),[205] 8 – 20 μm thick. A significant problem was the low sinterability of cerium electrolyte; for this reason, long-term sintering was performed at temperatures up to 1600 °C.[203] Nevertheless, the authors could not avoid crack formation in the SDC electrolyte, which may result in low power density: 60.6 mW cm^{-2} (700 °C).

A well-known way to increase the power of an SOFC with a membrane having mixed oxygen ionic and electronic conductivity is to apply a bilayer solid electrolyte, in which one of the layers has dominantly ionic conductivity and blocks the electron charge transfer. Matsuda *et al.*[206] considered a layer of ion conductor YSZ as a blocking layer from the anode side. It was shown that the transition to a bilayer electrolyte, in which one layer blocks the electronic conductivity of CeO_2, increases the cell efficiency in comparison with cells having single-layer electrolytes. A power density of 0.7 W cm^{-2} (700 °C) and a large value OCV = 1.1 V (700 °C) were obtained for a cell with YSZ/SDC20 electrolyte. However, delamination between YSZ and GDC layers after sintering was also observed. Kim *et al.*[207] proposed a technique of forming a dense two-layer YSZ/GDC electrolyte with a simultaneous decrease in the sintering temperature of layers. According to this technique, after depositing electrolyte layers by dip-coating, isostatic pressing at 300 MPa and sintering at 1250 °C were performed. The decrease in the sintering temperature made it possible to avoid undesirable interaction between YSZ and GDC with the formation of insulating phase $(Ce,Zr)O_2$, which arises at temperatures above 1350 °C. The isostatic pressing excluded the porosity of GDC layer and its delamination with YSZ.

Physical methods for synthesizing thin-film electrolytes — magnetron sputtering and pulsed laser deposition (PLD) — have become very popular. The application of these methods makes it possible to avoid high-temperature sintering after forming layers and weaken the interaction between CeO_2 and ZrO_2. Fairly high power density (1.07 W cm^{-2} at 750 °C) was obtained by Solovyev *et al.*[208] on a cell with single-layer electrolyte GDC10 (5 – 7 μm), formed with the aid of high-power reactive magnetron sputtering. Using PLD to form bilayer thin-film electrolyte YSZ (5 – 10 μm)/SDC20 (3 μm), Lu *et al.*[209] could increase significantly the power density: to 1.4 W cm^{-2} at 750 °C. The output was improved due to the higher density of layers of the bilayer electrolyte formed by PLD, in comparison with the electrolytes prepared using screen printing (Fig. 16 *a*). The ohmic resistances of the cell with a SDC20 layer formed by conventional screen printing and the cell with a laser-deposited layer were found to be 0.16 and 0.08 Ω cm^2, respectively. Yang *et al.*[210] applied PLD to fabricate a bilayer electrolyte $Zr_{0.9}Sc_{0.1}O_{1.9}$ (SSZ) (1 μm)/SDC20 (5 μm) with the following characteristics: OCV = 1 V and power density 1.6 W cm^{-2} at 700 °C. Despite the advantages of sputtering and deposition technologies, they have significant drawbacks: need for expensive equipment and complexity of scaling when being adapted to commercial production. The long-term stability of thin-film structures must also be studied.

A separate direction in the development of SOFC technology is the design of vertically aligned nanocomposites (VANs), which have a potential for increasing the SOFC output. The results of measuring the characteristics of an SOFC cell with this structure (YSZ/GDC10), obtained by PLD, were reported by Su *et al.*[211] An increase in the power density of an SOFC cell with a VAN structure by a factor of 1.9 relative to a cell with horizontally aligned

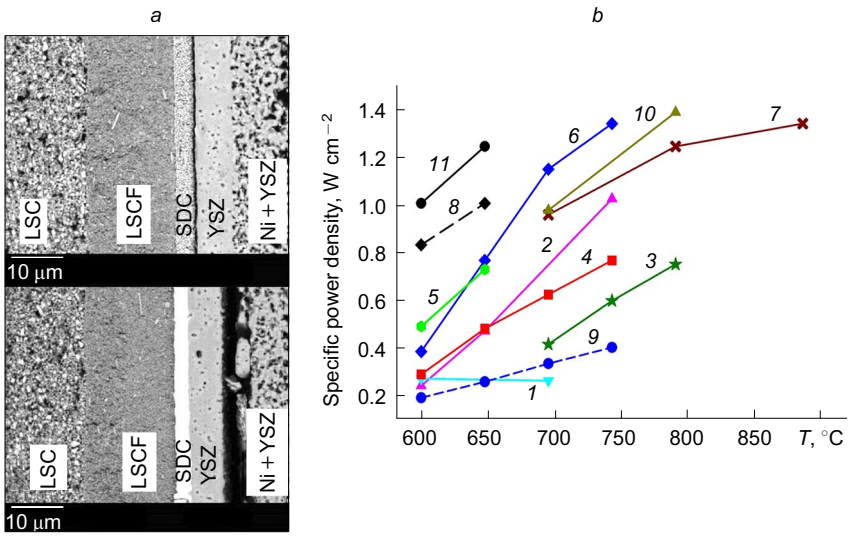


Figure 16. (*a*) SOFC microstructures obtained when forming a bilayer YSZ/SDC20 electrolyte by screen printing (upper part) and PVD (lower part)[209] and (*b*) temperature dependences of the specific power density of SOFCs with a thin-film electrolyte: (*1*) a single-layer SDC20,[204] (*2*) a single-layer GDC10,[208] (*3*) YSZ/YSZ-GDC10 with a VAN structure,[211] (*4*) electrolyte with an intermediate barrier layer GDC10/BCG/GDC10,[212] (*5*) with a barrier layer from the cathode side GDC10/YCSB,[213] (*6*) and with a barrier layer from the anode side YSZ/SDC20,[209] (*7*) YSZ/GDC10,[214] (*8*) NiO – BZCY/SDC20,[215] (*9*) BZCY/SDC20,[216] (*10*) YSZ/GDC10,[217] and (*11*) YSZ/GDC10.[202] The designations are as follows: BCG is $BaCe_{1-x}Gd_xO_3$, YCSB is $(Bi_{0.75}Y_{0.25})_{1.86}Ce_{0.14}O_{3-\delta}$, and BZCY is $BaZr_{0.1}Ce_{0.7}Y_{0.2}O_{3-\delta}$. The figure was compiled by the authors based on the data of aforementioned publications.

layers was demonstrated. However, the specific power density obtained by Su *et al.*[211] did not show any real advantage of VAN structures relative to SOFCs with single- and bilayer GDC10-based electrolytes obtained by other methods (Fig. 16 *b*). Hence, the study of the mechanisms of increasing the ionic conductivity in nanoheterostructures must be continued.

Many experts consider also protonic conductors based on $BaCeO_3$ as potential materials for the blocking layer from the anode side. These conductors have a higher ionic conductivity as compared with YSZ (especially in the low-temperature region) because of their lower activation energy ($\sim$0.6 eV). For example, Sumi *et al.*[218] investigated the multilayer electrolyte GDC10/BCY/GDC10 (BCY indicates the composition $BaCe_{0.8}Y_{0.2}O_{3-\delta}$) in a microtubular SOFC with a carrier anode. They obtained values OCV = 0.84 – 1.02 V and maximum of the specific power density up to 1.02 W cm^{-2} at temperatures in the range of 500 – 700 °C.

Some researchers[213, 219 – 222] considered the possibility of applying ionic conductors based on bismuth oxide, stabilized by erbium or yttrium, as materials of a barrier layer for a CeO_2-based electrolyte from the cathode side. The maximum power density obtained with this method was found to be 1.95 W cm^{-2} at 650 °C and OCV $\approx$ 1.0 V. Incorporation of the high-conductivity oxide Bi_2O_3 (730 mS cm^{-1} at 800 °C) into a bilayer electrolyte, along with the general decrease in ohmic resistance, makes it also possible to decrease the polarization resistance due to the enhancement of carrier transport at the cathode/electrolyte interface. In addition, in the case of a barrier layer from the cathode side, the influence of partially reduced CeO_2 on the anode depolarization is retained, which on the whole allows for high specific power densities. However, crucial factors for cells of this type are the thickness of layers[221] and long-term stability of their characteristics. The influence of the decrease in thickness of bilayer electrolyte YSZ/GDC from 8 to 2.5 μm and PrO_x infiltration into the cathode LSCF – GDC (LSCF stands for the composition $La_{0.6}Sr_{0.4}Co_{2.0}Fe_{0.8}O_{3-\delta}$) on the output of a single SOFC with a carrier anode NiO – YSZ was investigated by Park and Barnett.[223] The YSZ film was obtained by slip casting on the carrier anode, preliminary sintering at 1150 °C, and subsequent deposition of a GDC layer by dip-coating. Final sintering was performed at 1250 °C. Low sintering temperature was attained by applying sintering additive Fe_2O_3. The authors showed that a decrease in the film thickness not only reduces the ohmic resistance of electrolyte but changes also the polarization characteristics of electrodes. Due to the partial gas permeability of thin-film electrolyte (2.5 μm), the humidity of anode gas mixture increases, which reduces significantly the polarization resistance of the cermet anode. The insignificant increase in the cathode polarization due to the formation of water vapour was compensated as a result of its activation by praseodymium oxide. In sum, the following values of the specific power density were obtained: 2.38 W cm^{-2} (at 800 °C) and 0.95 W cm^{-2} (at 650 °C). The activation effect is most pronounced at low temperatures. Indeed, the increase in power in comparison with the power for an SOFC with a 8 μm film and unactivated electrodes is 74% at 800 °C and 136% at 600 °C.

Bilayer electrolytes and their fabrication methods were recently reviewed in detail.[224] The most characteristic

Table 5. SOFC characteristics obtained using different electrolyte fabrication technologies.

SOFC structure: anode/electrolyte/cathode	OCV, V (T, °C)	Specific power density, W cm^{-2}	ASR,[a] Ω cm^{-2} (°C)	Ref.
Technologies of vacuum deposition and precipitation				
High-power pulsed reactive magnetron sputtering of GDC *on the* NiO – YSZ *carrier anode*				
NiO – YSZ/GDC10 (5 – 7 μm)/LSC	0.77 – 0.80 (600 – 750)	0.25 (600)	–	208
		0.49 (650)	–	208
		1.07 (750)	–	208
Screen printing of SDC *on the* NiO – YSZ/YSZ *half cell*				
NiO – YSZ/YSZ ($\sim$5 – 10 μm) – SDC20 ($\sim$3 μm)/LSCF – LSC	$\sim$1.1 (600 – 750)	0.96 (750)	0.51 (750)	209
		0.68 (700)	0.68 (700)	209
		0.46 (650)	1.16 (650)	209
		0.26 (600)	2.45(600)	209
Pulsed laser deposition of SDC *layer on the* NiO – YSZ/YSZ *half cell*				
NiO – YSZ / YSZ ($\sim$5 – 10 μm) – SDC20 ($\sim$ 3 μm)/LSCF – LSC	$\sim$1.1 (600 – 750)	1.4 (750)	0.55 (750)	209
		> 1.2 (700)	0.67 (700)	209
		> 0.8 (650)	1.18 (650)	209
		> 0.4 (600)	2.13(600)	209
Successive pulsed laser deposition of YSZ, VAN *structure* YSZ/GDC, GDC *on the* NiO – YSZ *carrier anode; annealing of SOFC structure at 1150 °C (2 h)*				
NiO – YSZ/YSZ (1.5 μm) – VAN YSZ/GDC10 (4.5 μm)/LSC	1.04 (700)	0.432 (700)	–	211
	–	0.623 (750)	–	211
	–	0.783 (800)	$\sim$0.26 (800)	211

Table 5 (continued).

SOFC structure: anode/electrolyte/cathode	OCV, V (T, °C)	Specific power density, W cm^{-2}	ASR,[a] Ω cm^{-2} (°C)	Ref.
Technologies of vacuum deposition and precipitation				
Magnetron sputtering of YSZ – GDC *on the* NiO – YSZ *carrier anode, electrolyte sintering at 1100 °C*				
NiO – YSZ/YSZ – GDC10 (10 μm)/LNO (without activation)	~1.05 (800)	0.7 (800)	–	214
	~1.1 (700)	0.3 (700)	–	214
NiO – YSZ/YSZ – GDC10 (10 μm)/LNO (with activation of electrodes)	~1.05 (800)	1.3 (800)	–	214
	~1.1 (700)	1.0 (700)	–	214
Pulsed laser deposition of ESB layer on the SDC20 electrolyte; deposition of the ESB layer on the SDC20 electrolyte by dip-coating				
Pt/SDC – ESB/(Au, Ag) – ESB, thickness ratio of SDC20 and ESB:				
1.6 mm : 0.8 μm	0.62 (600), 0.60 (800)	–	–	221
1.76 mm : 1.3 μm	0.65 (600), 0.57 (800)	–	–	221
1.5 mm : 9 μm	0.82 (600), 0.65 (800)	–	–	221
1.5 mm : 22 μm	0.95 (600), 0.80 (800)	–	–	221
Successive PLD of YSZ, GDC10, GSC *layers on the* NiO – YSZ *carrier anode*				
NiO – YSZ/YSZ – GDC10/GSC, thickness ratio of YSZ and GDC10:				
1.9 μm : 5 μm	~0.9 (600)	0.310 (600)	–	225
2.7 μm : 5 μm	–	0.325 (600)	–	225
3 μm : 5 μm	–	0.400 (600), 0.450 (650), 0.500 (700)	–	225
3.5 μm : 5 μm	–	0.350 (600)	–	225
Ceramic technologies				
Slip casting/rolling, final sintering at 1450 °C				
Anode NiO – GDC10, electrolyte/cathode versions:				
GDC10 (20 μm) – ESB (10 – 12 μm)/LSM – ESB	0.808 (650)	0.38 (650)	0.17 – 0.85[b] (600)	213
GDC10 (20 μm) – YCSB (10 – 12 μm)/LSM – YCSB	0.833 (650)	0.76 (650), 0.51 (600)	0.22 – 0.20[b] (600)	213
GDC10 (20 μm) – YCSB (10 – 12 μm)/BRO7 – YCSB	0.853 (650)	0.68 (650)	0.18 – 0.19[b] (600)	213
Co-pressing of the anode and electrolyte layers, sintering at 1350 °C (5 h)				
NiO – SDC20/NiO – BZCY (50 μm) – SDC20 (15 μm)/	1.01 (600)	0.868 (600)	–	215
SSC – SDC20	1.0 (650)	~1.05 (650)	~0.15 (650)	215
Co-pressing of the anode and electrolyte layers, sintering at 1400 °C (5 h)				
NiO – SDC20/BZCY (11 μm) – SDC20 (19 μm)/SSC – SDC20	1.09 (550)	0.127 (550)	0.90(550)	216
	1.07 (600)	0.197 (600)	0.68(600)	216
	1.04 (650)	0.267 (650)	0.55(650)	216
	1.0 (700)	0.347 (700)	0.43(700)	216
	0.96 (750)	0.418 (750)	0.35 (750)	216
Calendering, sintering at 1250 °C (4 h)				
NiO – YSZ/YSZ (~5 μm) – GDC10 (~5 μm)/	~1.10 (700 – 800)	1.02 (700)	0.106 (700)	217
(LSCF – GDC10) / LSCF		1.45 (800)	0.046 (800)	217
Co-pressing of the anode and SNDC electrolyte layers, sintering at 1400 °C (5 h); Deposition of the ESB electrolyte by drop coating, sintering at 800 °C (10 h)				
NiO – SNDC/SNDC (~5 μm) – ESB (~5 μm)/PBM – ESB	0.986 (400)	0.986 (400)	16.708 (400)	222
	0.945 (500)	0.945 (500)	0.091(500)	222
	0.853 (600)	0.853 (600)	0.074 (600)	222
	0.801 (650	0.801 (650)	0.027 (650)	222
Co-pressing of the anode and electrolyte layers, sintering at 1350 °C (5 h)				
NiO – GDC10/GDC10 (26 μm) / SSC – GDC10	1.01 (400)	0.10 (400)	–	226
	0.92 (500)	0.40 (500)	1.822 (500)	226
	0.85 (600)	0.75 (600)	0.329 (600)	226

Table 5 (continued).

SOFC structure: anode/electrolyte/cathode	OCV, V (T, °C)	Specific power density, W cm^{-2}	ASR,[a] Ω cm^{-2} (°C)	Ref.
Solution and colloidal technologies				
Spin coating, final cell sintering at 950 °C (2 h)				
NiO – YSZ/AFL/YSZ (100 nm)/GDC10 (400 nm)/	~1.0 (500 – 650)	~1.05 (600)	–	202
GDC10 – LSCF		~1.3 (650)	0.038 (650)	202
Electrophoretic deposition on the Ni – SDC20 *carrier anode, sintering at 1600 °C (10 h)*				
NiO – SDC20/SDC20 (20 μm)/Pt	0.63 (700)	0.0606 (700)	–	203
	–	0.0713 (800)	–	203
Electrophoretic deposition on the NiO – SDC20 *carrier anode with a graphite conductive sublayer, sintering at 1400 °C (25 h)*				
NiO – SDC20/SDC20 (8 μm)/LSC	~0.65 – 0.70	0.281 (600)	0.064 (600)	204
	(600 – 700)	0.272 (700)	0.035 (700)	204
Successive EPD of NiO – GDC10/GDC10/LSCF – GDC10 *layers on a graphite rod, co-sintering at 1500 °C*				
NiO – GDC10 (110 μm)/AFL/NiO – GDC10 (9 μm)/	~0.7 (600)	0.42 (600)	–	205
GDC10 (10 μm)/LSCF – GDC10 (37 μm)	–	0.35 (650)	–	205
	~0.6 (700)	0.25 (700)	–	205
Successive EPD of YSZ *and* SDC20 *layers on the* NiO – YSZ *carrier anode, co-sintering at 1400 °C (2 h)*				
NiO – YSZ/YSZ (4 μm) – SDC20 (1 μm)/LSCF (30 μm)	~1.1 (700)	~0.7 (700)	~0.2 (700)	206
Deposition of the AFL, YSZ, GDC10 *on the* NiO – YSZ *carrier anode by dip coating in combination with isostatic pressing*				
NiO – YSZ/AFL/YSZ – GDC10/LSCF – LSC, compacting pressure:				
0 MPa	0.965 (600)	0.194 (600)	1.632 (600)	207
100 MPa	1.094 (600)	0.834 (600)	0.609 (600)	207
200 MPa	1.103 (600)	0.912 (600)	0.570 (600)	207
300 MPa	1.107(600),	0.938 (600),	0.549 (600),	207
	1.097 (650)	1.251 (650)	0.535 (650)	
Spin coating of GDC10, BaO7GDC10, GDC10 *on the* NiO – YSZ *carrier anode, synthesis of intermediate the BCG layer from oxides during sintering*				
NiO – SDC/GDC10 (22 μm) – BCG (7 μm)/	0.820 (750) – 0.998 (550)	0.2 (550)	–	212
GDC10 (10 μm)/SSC		0.3 (600)	–	212
		0.65 (700)	–	212
		0.80 (750)	–	212
Deposition of the YSZ *film on the* NiO – YSZ *carrier anode by slip casting with preliminary sintering at 1150 °C; subsequent deposition of the* GDC10 *film by dip ping, co-sintering at 1250 °C*				
NiO – YSZ/YSZ – GDC10/LSCF – GDC10; electrolyte thickness:				
8 μm	1.110 (600)	0.24 (600)	1.93 (600)	223
	1.094 (700)	0.68 (700)	1.10 (700)	223
	1.076 (800)	1.34 (800)	0.79 (800)	223
Deposition of the YSZ *film on the* NiO – YSZ *carrier anode by slip casting with preliminary sintering at 1150 °C; subsequent deposition of the* GDC10 *film by dip coating, co-sintering at 1250 °C*				
NiO – YSZ/YSZ – GDC10/LSCF – GDC10; electrolyte thickness:				
2.5 μm	1.093 (600)	0.38 (600)	0.76 (600)	223
	1.074 (700)	1.20 (700)	0.41 (700)	223
	1.052 (800)	1.27 (800)	0.22 (800)	223
2.5 μm (activation of PrO_x cathode)	–	0.52 (600)	0.52 (600)	223
	–	1.47 (700)	0.27 (700)	223
	–	2.38 (800)	0.22 (800)	223

Note. Designations: ESB is $Er_{0.4}Bi_{0.16}O_3$, BCG is $BaCe_{1-x}Gd_xO_3$, GSC is $Gd_{0.5}Sr_{0.5}CoO_3$, BRO7 is $Bi_2Ru_2O_7$, SNDC is $Sm_{0.075}Nd_{0.075}Ce_{0.85}O_{2-\delta}$, PBM is $Pr_{0.5}Ba_{0.5}MnO_{3-\delta}$, SSC is $Sm_{0.5}Sr_{0.5}CoO_3$, and AFL is anode functional layer. [a] Total polarization resistance per cell unit area (area specific resistance). [b] The second value shows the ASR degradation after 50 h.

results of implementing thin-film technologies in SOFCs are listed in Table 5. It should be noted that, without application of blocking layers in cells with thin-film electrolytes, the OCV obtained is on the order of 0.6 – 0.7 V, depending on temperature, whereas the application of the barrier layer from the cathode and anode sides may increase OCV to 1 V or even more.

5. Theoretical approaches to modelling SOFCs with an electrolytic membrane based on a mixed conductor

SOFC simulation allows one to choose deliberately ways to increase the energy efficiency of developed electrochemical devices by determining the necessary combination of transport and electrochemical properties of materials, their microstructure, thickness of SOFC layers, cell geometry, *etc*.[13] In practice, an empirical approach is generally used, which is based on estimation of the operability of electrochemical cell breadboards. As a result, it is difficult to interpret and understand the relationships and quantitative regularities between the actually determined SOFC parameters and the implemented mechanisms of charge and mass transfer. To represent correctly the operation of SOFCs, it is necessary to develop theoretical models of the processes occurring in them at different levels: quantum-mechanical level for describing the electronic structure; mesoscopic level, concerning the influence of microstructure and morphology and materials; and macroscopic or continuum level, at which the corresponding layers of SOFC are presented as continuous media with effective averaged parameters.

Along with electrochemical reactions, related processes of heat- and mass transfer occur also in SOFC, as a result of which thermomechanical stresses arise in the SOFC solid structure. These stresses are caused by the difference in the coefficients of thermal expansion (CTEs) of materials and occurrence of temperature gradients, as well as the time-dependent processes of changes in temperature.[227] The state of the SOFC structure is significantly affected by the mechanical stresses arising as a result of the expansion of materials, caused by the partial oxygen pressure gradient.[228]

At the microscopic level, DFT, quantum chemistry, and molecular dynamics methods are applied, due to which one can perform *ab initio* quantum-mechanical simulation of electrochemical reactions and determine the electronic structure of condensed systems, the catalytic activity of reacting particles, the interaction and diffusion of defects, the conductivity of materials, and their coefficients of thermal expansion.[229, 230]

5.1. Continuum and phenomenological models of the processes occurring in SOFCs

In contrast to the microscopic description of processes at the level of individual particles and point defects in crystal, macroscopic SOFC models are based on the concept of individual layers in the form of an idealized continuous medium with averaged effective parameters, whose values are determined either experimentally or on the basis of microscopic models. The emphasis of Adler's review[231] is on the key aspects related to electrode processes, which determine to a great extent the SOFC output. One can select the following types of electrodes with significantly different factors determining the SOFC output and limiting the stages of charge and mass transfer processes:

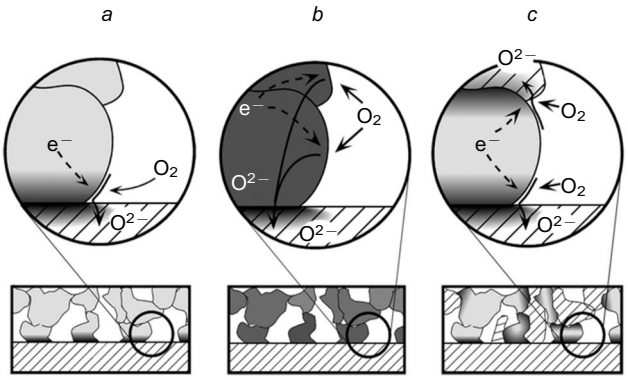


Figure 17. Schematic diagrams of electrode reactions for electrodes based on (*a*) electronic and (*b*) mixed conductors and (*c*) a composite electrode based on electronic and ionic conductors.[231] Published with permission of American Chemical Society.

— electrodes with electronic conductivity, whose efficiency is determined by the three-phase boundary region (Fig. 17 *a*);

— electrodes with mixed (oxygen ionic and electronic) conductivity, whose efficiency is determined by the surface exchange and diffusion of oxygen ions in the electrode material (Fig. 17 *b*);

— composite electrodes consisting of mixtures of electronic (electrode material) and ionic (electrolyte) conductors (Fig. 17 *c*); these mixtures are applied to increase the electrochemical activity of electrode with basically electronic conductivity and expand the three-phase boundary region.

The cathode reaction is described in terms of the concept of three-phase boundary: the region at the electrolyte/cathode/gas boundary in which the oxygen reduction reaction is implemented. The concept of three-phase boundary was proposed for the first time by Schmid[232] when studying the mechanism of H_2 oxidation on a platinum electrode. A characteristic feature of these electrodes is the significant role of the exchange with the gas medium and diffusion, which gave grounds to call them gas-diffusion electrodes. For example, the reaction of oxygen reduction on porous platinum electrodes with YSZ electrolyte includes several interrelated limiting stages: adsorption of molecular oxygen on the electrode surface, its dissociation, and surface diffusion to the Pt/YSZ interface. As was noted in review,[231] when the role of diffusion is decisive, one cannot relate the kinetics of electrode reaction to only the length of three-phase boundary, because the electrochemical reaction and diffusion are jointly limiting stages in this case.

The increase in efficiency and optimization of the microstructure of electrode (especially cathode) materials should be directed at expanding the region in which the electrode reaction occurs by choosing an appropriate electrode material and a certain combination of microstructure parameters (morphology, size of grains and pores, porosity) with the electrode layer thickness. In this context, we should note the study by Kleitz,[233] who described a structure with a double electrode layer, consisting of a highly porous gas-permeable current collector with a high conductivity and a thin dense layer with mixed conductivity, contacting with the electrolyte layer. On the one hand, the dense electrode layer should be sufficiently thin to make low its resistance to the transverse diffusion

flux of oxygen ions. On the other hand, its resistance to the electron current along the layer (*i.e.*, parallel to the electrode/electrolyte interface) must be low as well. The following expression was obtained for the voltage drop (U_R) caused by the ohmic resistance to the electron current in the plane of thin dense electrode layer:

$$U_R = \frac{1}{4}\,\frac{\rho_{el}\, i}{h_{el}}\, r_p^2 \qquad (26)$$

where i is the ion current density through the electrode/electrolyte interface; h_{el} and ρ_{el} are, respectively, the thickness of the dense thin-film material of electrode layer and its resistivity to the electron current; and r_p is the average radius of pores at the interface between the dense and porous electrode layers. In the case of high electronic conductivity of electrode material (>100 S cm^{-1}), the additional overvoltage U_R is rather low, but at an electrical conductivity of ~ 0.1 S cm^{-1} it affects significantly the electrode reaction kinetics.

Currently, the kinetics of the electrode reaction of oxygen reduction on porous MIEC electrodes is most often described within the Adler – Lane – Steel (ALS)[234] model. The processes occurring on electrodes contribute to the cell chemical impedance, which is determined jointly by the limiting stages of oxygen surface exchange and bulk diffusion of oxygen ions in the porous electrode. A modified model of the impedance of composite electrodes was presented by Mortensen *et al.*[235] More generalized theoretical models take into account the internal microstructure of electrodes, which can be presented, *e.g.*, as a system of cylindrical or cubic pseudoparticles.[236, 237] The researchers from the group headed by Ivers-Tiffée[238] are developing the relaxation time distribution method for analyzing the electrode response. The state of the art of this method as applied to the analysis of electrochemical impedance spectroscopy data was reviewed briefly by Gavrilyuk *et al.*[239] The authors described the theoretical fundamentals of the method; considered different ways to solve the Fredholm equation of the first kind with application of the Tikhonov regularization method; and demonstrated (based on numerical experiments) the high resolution of the method, in particular, when processing 'noisy' impedance spectra. The development of the theoretical basis of this method was reported by Boukamp and Rolle.[240]

A comparative analysis of different model representations of the MIEC-cathode microstructure[241] showed that the microstructure affects significantly the electrode kinetics near electrode/electrolyte interface, when the size of electrochemical reaction zone becomes comparable with the characteristic size determining its microstructure or even smaller. Far from the interface the porous microstructure can be described by averaged parameters, as in the ALS model.

5.2. Development of macroscopic continuum models of SOFC with a solid electrolyte having mixed conductivity

The charge transfer in an SOFC with an MIEC-electrolyte was described for the first time by Choudhury and Patterson[242] using the approaches, developed in the Wagner theory, which considers the diffusion of oxygen ions under the action a chemical potential gradient during metal oxidation. On the assumption of local electroneutrality, the authors derived integral equations to calculate the voltage across a cell with solid-oxide electrolyte under conditions of constant difference in the chemical potentials of the cathode and anode. The current – voltage characteristics and distribution of chemical potential in the electrolyte layer were found; the electrode polarization was disregarded in that model. The theoretical models of transport processes occurring in SOFCs with an MIEC electrolyte were further developed by Tannhauser,[243] who analyzed the one-dimensional transport of oxygen vacancies and electrons in electrolyte CeO_2 doped with Ca^{2+} ions. An electrolytic material in thermodynamic equilibrium with a gas medium having a certain partial oxygen pressure was considered and relations between the theoretical Nernst voltage and the voltage across the cell with allowance for electron current leakage were established.

The following expression was derived for the open-circuit value:

$$\mathrm{OCV} = \mathrm{E_{th}} - \frac{kT}{e}\ln\left(1 + \frac{\sigma_{el}^{(1)}}{\sigma_{ion}^{(0)}}\right) \qquad (27)$$

where E_{th} is the voltage determined from the Nernst formula (23), $\sigma_{el}^{(1)}$ is the electronic conductivity of electrolyte material from the anode side at a partial oxygen pressure $p_{O_2}^{(1)}$, and $\sigma_{ion}^{(0)}$ is the average ionic conductivity of electrolyte. The cell energy efficiency decreases with an increase in the partial electronic conductivity in the electrolyte.

In the studies by Riess,[144, 244] on the assumption of constant ion concentration in the electrolyte layer, dependences of electron concentration and current density on the external voltage across a cell operating under steady-state conditions were obtained by solving the differential equations for carrier transport. It was shown that the electron concentration in the electrolyte layer decreases monotonically from the fuel to oxygen electrode (Fig. 18). An increase in the voltage across the cell leads to a decrease in the ion current and an increase in the electron current; the efficiency of MIEC electrolyte cell will be maximum at a certain optimal voltage across the electrodes:

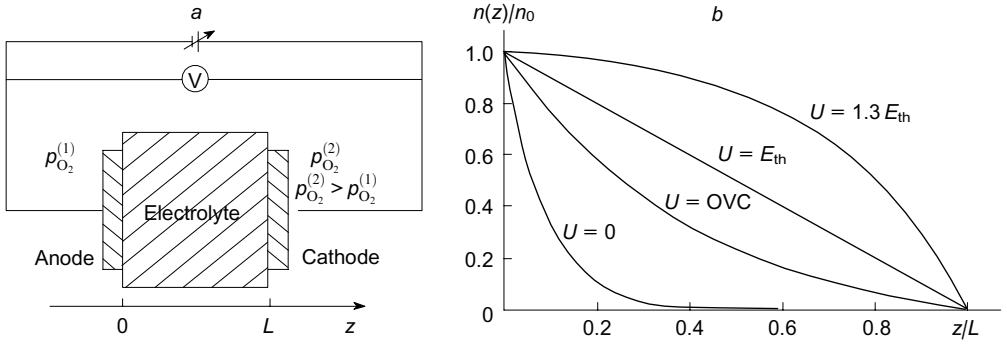


Figure 18. (*a*) Schematic of an SOFC with a single-layer MIEC electrolyte of thickness L and (*b*) depth distributions of electron concentration $n(z)$ in the electrolyte layer at different voltages (U) and a temperature of 800 °C.[144] Published with permission of IOP Publishing.

$$U_{max} \approx \frac{E_{th}}{2} \quad (27a)$$

To satisfy this condition, the open-circuit voltage must exceed $E_{th}/2$; in this case, the electron current through the MIEC-electrolyte layer is blocked. Electron current blocking can also be provided by forming regions of electronic conductivity near the anode (n region), hole conductivity near the cathode (p region), and ionic conductivity (i region) in the central part of electrolyte.

More general one-dimensional models take into account the nonuniform distribution of ion concentration in the electrolyte layer along the charge transfer path. For example, Duncan *et al.*[245,246] described the charge transfer in an SOFC structure using the Nernst – Planck equation in the continuous-medium approximation and the Butler – Volmer equation for the overvoltage across the electrode; this approach made it possible to determine the influence of current density on the values of activation and ohmic overvoltage. It was established that the cathode overvoltage becomes determining with a decrease in the SOFC working temperature and that the OCV sharply drops with a decrease in the electrolyte thickness because of the increase in the leakage current (Fig. 19). At the same time, the ohmic losses increase with an increase in the electrolyte thickness. Therefore, one can determine the optimal thickness of electrolyte with mixed conductivity ($\sim$7 μm) corresponding to the maximum generated SOFC power.

A more complicated theoretical model was developed by Shen *et al.*[247,248] for the case of two-dimensional spatial distribution of flows in an SOFC cell. Transport processes in the cell both along the gas channels through which reagents (hydrogen and oxygen) are fed and in the transverse direction, along which the ion and electron charges are transferred. The developed models made it possible to determine the influence of parameter distribution both along the gas flow directions in the anode and cathode channels and across the SOFC planar structure. Dependences of the electron leakage current on the voltage across the cell at different velocities of supplied gas flows were obtained. The leakage current increased with an increase in voltage; however, according to the simulation results, the influence of the flow velocity on the leakage current turned out to be insignificant. There may be some influence of fuel flow velocity in the anode channel: slowing down the flow leads to a decrease in the leakage current.

A fuel cell containing a two-layer electrolyte, with a layer blocking the electron leakage current, was studied by Virkar[249] using the equivalent electric circuit method. The ion and electron charge transfer is considered under the local equilibrium conditions, at which there is a correspondence between the oxygen chemical potential (μ_{O_2}) and local partial oxygen pressure at each point of electrolyte:

$$\mu_{O_2} = \mu^{\circ}_{O_2} + kT \ln p_{O_2} \quad (28)$$

where $\mu^{\circ}_{O_2}$ is the standard value of oxygen chemical potential.

In the general case the carrier flow is due to the presence of electrochemical potential gradient. It was assumed that there is no chemical potential gradient for electrons, and they are transported only under the action of electric potential gradient, whereas the oxygen ion flux is due to the gradients of both p_{O_2} and electric potential. A case with a layer of electrolyte with mixed electronic – ionic conductivity (for example, based on CeO_2), located at the cathode side, and a blocking layer of electrolyte with mainly ionic conductivity (*e.g.*, YSZ), at the anode side, was considered. The equivalent electric circuit method was used to obtain the expression for partial oxygen pressure at the interface between the blocking layer and MIEC electrolyte. The corresponding value p_{O_2} at the interface in the case of open circuit in the absence of essential electronic conductivity in the blocking layer is determined by the partial pressure from the side of air electrode (cathode). In the general case, the larger the ratio of the electronic conductivity of MIEC electrolyte to that of the blocking layer, the higher the partial oxygen pressure at their interface. The high partial pressure at the interface provides thermodynamic stability of the MIEC electrolyte; therefore, along with high ionic conductivity, there must be rather high electronic conductivity of electrolytic material from the side of air electrode (the latter can be obtained, in particular, by introducing transition metal additives, see Section 2.2.1). It was shown that, when the influence of the polarization resistance of electrodes is weak, the generated cell specific power is maximum if the total resistance of bilayer electrolyte to ion current is equal to the load resistance. Within this model the maximum power monotonically increases with a decrease in the blocking layer thickness at a constant total thickness of bilayer electrolyte, while the partial oxygen pressure at the interface between electrolytic layers decreases (Fig. 20). Thus, there arises an actual limitation on the degree of decreasing the blocking layer thickness in comparison with the total thickness of electrolyte to provide thermodynamic stability of the latter.

The influence of partial oxygen pressure on the electronic conductivity was disregarded;[249] it was taken into account later by Marques and Navarro.[250] As a result, the influence of ionic conductivity, thickness of layers, and

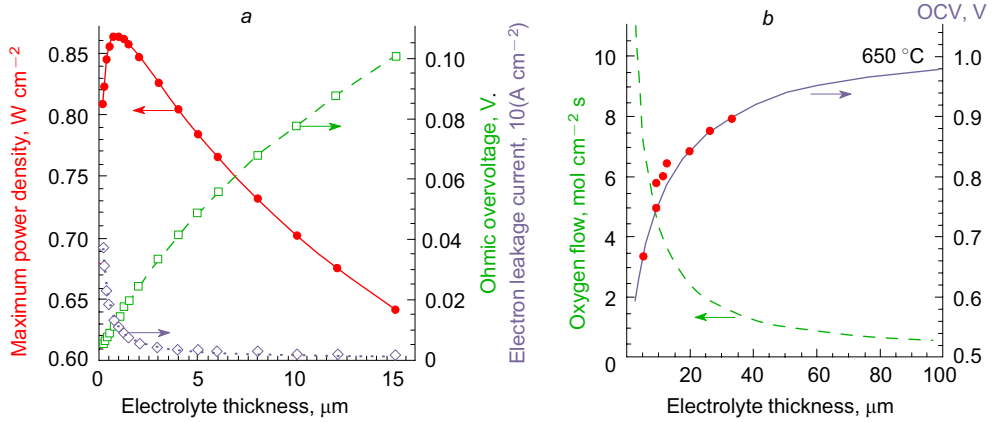


Figure 19. Calculated dependences of (*a*) maximum power density, electron leakage current, and ohmic overvoltage and (*b*) OCV and oxygen flow on the electrolytic-membrane thickness.[246] Published with permission of Elsevier.

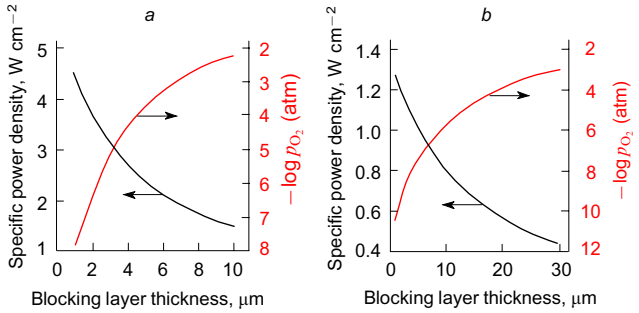


Figure 20. Dependences of maximum power density and partial oxygen pressure at the boundary between electrolytic layers on the blocking layer thickness at fixed total thicknesses of (*a*) 30 and (*b*) 130 μm.[249] Published with permission of IOP Publishing.

blocking layer position (from the anode or cathode side) on the open circuit voltage, distribution profile of partial oxygen pressure, and oxygen ion flux were determined.

Wang *et al.*[251] presented simulation results for bilayer electrolyte BZCY/SDC20. A one-dimensional numerical SOFC model with SDC electrolyte and blocking BZCY layer was developed on the basis of the Nernst – Planck equation of ion and electron transport of n and p types under gradients of electrical and chemical potentials. The authors used the following simplifications:

— the ionic conductivity of electrolyte is independent of partial oxygen pressure; the dependence of the electronic conductivity of n and p types on the partial oxygen pressure is described by a power law;

— the main contribution is from the activation and ohmic polarization, the concentration polarization is absent; and the temperature distribution in the cell is uniform;

— charge carrier fluxes are directed perpendicular to the BZCY/SDC interface;

— the flux value does not change along the interface.

The formulation of transport equations is due to the charge conservation condition and the dependence of flux on the electrochemical potential gradient. The activation losses on electrodes are taken into account within the model in the Butler – Volmer equation. The transport equations were solved with allowance for the constant electric potential difference between the outer anode and cathode surfaces. The solution was performed by the finite-element method using the Comsol Multiphisics 5.2 software. As a result, the following cell parameters were found: OCV, specific leakage currents, current – voltage characteristics, specific power density at a voltage of 0.7 V, electrochemical efficiency, and distribution of partial oxygen pressure. The calculations were carried out for different working temperatures and thickness ratios for the main and barrier layers; hence, the calculation results can be used to optimize the design of cells having a barrier layer doped with barium cerate and ceria-based electrolyte. The authors performed a comparative analysis of two SOFC configurations.

Configuration 1 — the barrier layer is located from the anode side: anode (500 μm)/BZCY (19 μm)/SDC (11 μm)/cathode (40 μm).

Configuration 2 — the barrier layer is located from the cathode side: anode (500 μm)/SDC (11 μm)/BZCY (19 μm)/cathode (40 μm).

It was found that the OCV is higher and the leakage current is lower in configuration 1 as compared with configuration 2. Lowering temperature led to an increase

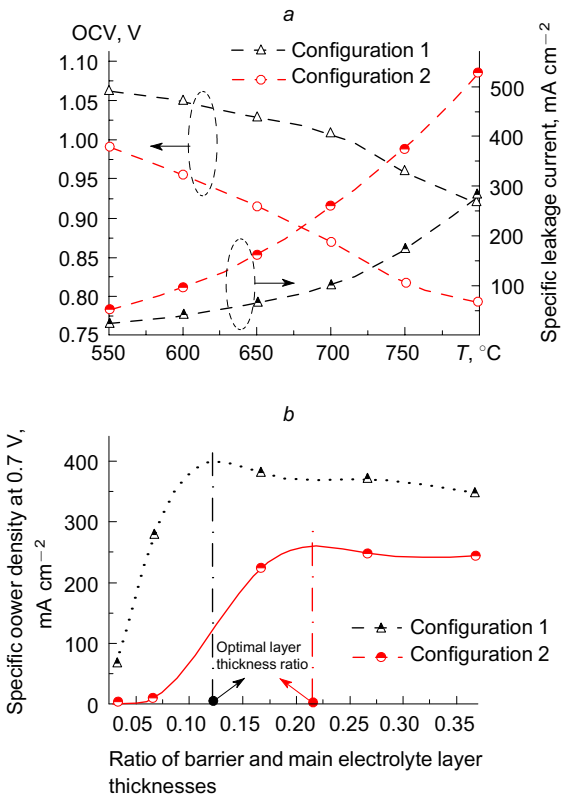


Figure 21. (*a*) Temperature dependences of OCV and leakage current and (*b*) dependences of power density (at 0.7 V) on the layer thickness ratio for bilayer electrolyte BZCY/SDC in cell configurations 1 and 2.[251] Published with permission of Elsevier.

in leakage current and a decrease in OCV. Thus, with an increase in temperature, configuration 1 generates higher specific power, because the lower OCV plays an important role in configuration 2 (Fig. 21 *a*). The optimal thickness ratios for the main and barrier electrolyte layers at which the cell specific power is maximum are, respectively, 0.12 and 0.22 for the first and second configurations (Fig. 21 *b*).

The problem of electron current leakage in electrolytes with mixed conductivity can be solved by applying composite electrolytes, *e.g.*, a mixture of oxygen-conducting particles based on cerium oxide and particles blocking the electronic conductivity, in particular, $BaCe_{0.8}Sm_{0.2}O_{3-\delta}$ (BCS). A material blocking electronic conductivity can be applied in the form of an insulating shell on oxygen-conducting cerium oxide particles. Ma *et al.*[252] performed a numerical simulation of charge transfer in a core/shell composite structure using the spherical shell model. They used the Nernst – Planck transport equation to describe the flux of ions, electrons, and protons; the stochastic Monte Carlo method to simulate the random particle distribution (Fig. 22 *a*), and the core/shell model to calculate conductivity (Fig. 22 *b*). The proton transport number, open circuit voltage, leakage currents, and generated power depend on the volume fraction of BCS particles (Fig. 22 *c*). When the blocking shell consists of small BCS particles with protonic conductivity, surrounding larger particles of MIEC electrolyte SDC20, the SOFC parameters are significantly affected by the contact angle between contacting SDC20 particles (Fig. 22 *b*). With an increase in this angle and, correspondingly, the contact area between particles, the leakage current increases and OCV decreases.

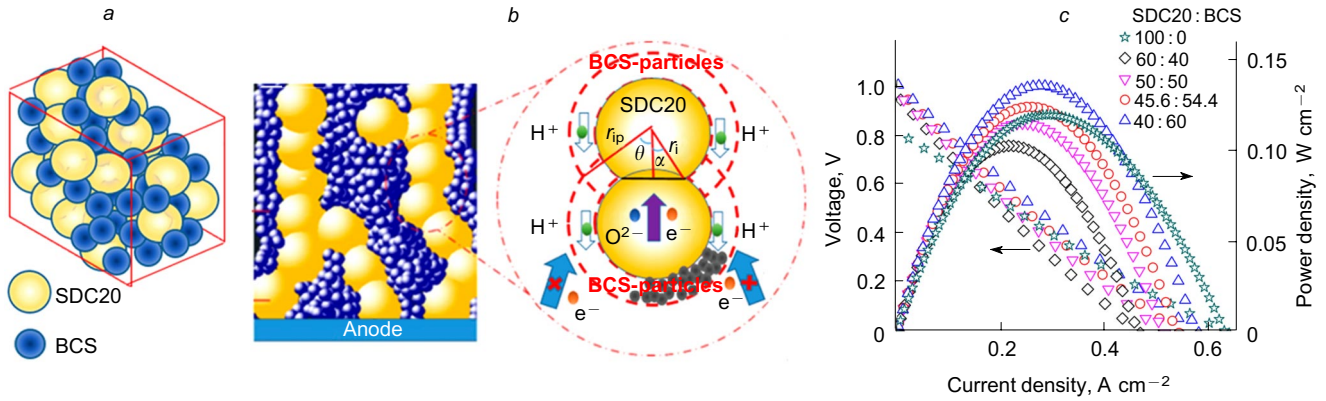


Figure 22. (*a*) Model of random particle distribution in composite electrolyte SDC20/BCS, (*b*) directions of electron, oxygen ion, and proton transport in the core/shell model (r_i is the radius of SDC20 particle and r_{ip} is the radius of SDC20 particle with a BCS shell), and (*c*) theoretical current–voltage and power characteristics (at 600 °C) for composite electrolyte SDC20/BCS of different compositions.[252] Published with permission of American Chemical Society.

Thus, the above review of theoretical models describing the processes occurring in SOFCs with a mixed-conductivity electrolyte showed that one can increase the generated power of SOFCs and provide their operational stability by complex optimization of the microstructural, electrochemical, and transport characteristics of both the porous electrode materials and the electrolyte material. It is of interest to develop further the theoretical models and methods of numerical simulation of the electrochemical reactions occurring in SOFC and the corresponding heat- and mass exchange processes using the methods of computational hydrodynamics, kinetic theory, and lattice Boltzmann equations.[253, 254]

6. Nanocomposites based on electrolytes with mixed conductivity

It was shown in the previous Sections that, when passing to the low-temperature range (< 600 °C), the conductivity activation energy in solid electrolytes based on CeO_2 increases significantly due to the formation of vacancy associates, and the grain boundary resistance rises significantly as well. Thus, to provide successful operation of CeO_2 electrolytes in low-temperature devices, along with doping (aimed at modifying the bulk properties of material), one must increase the grain boundary and interface conductivity. Nanomaterials have undoubted advantages in this context. However, single-phase nanomaterials based on CeO_2 are characterized by enhancement of not only ionic but also electronic conductivity, which is a hindrance for their use as SOFC electrolytes.[115, 254, 255] Therefore, the design of nanocomposites has become an object of special interest for some research teams. In particular, intense studies of nanocomposites based on ceria and different salts of alkali metals have been performed for the two last decades. Among them, of particular interest are the carbonate systems referred to as 3C (Ceria Carbonate Composite) materials in the literature. The works aimed at designing these composite systems, analyzing their properties, and applying them in low-temperature SOFCs, as well as the the studies devoted to the discussion of the conductivity mechanisms and problems of stability of these materials, were considered in detail in reviews.[256 – 260] Currently, studies aimed at applying materials based on salts and ceria in the SOFC technology are performed by several research teams from China, Sweden, Finland, India, France, and Portugal. In Russia, to the best of our knowledge, investigations of different salt composites were performed mainly for systems with an inert oxide phase,[261 – 263] whereas publications on salt ceria-based composites are absent.

6.1. Composition and structure of salt nanocomposites

An analysis of foreign publications showed that both singly doped and co-doped electrolytes with a high ionic bulk conductivity are used as a solid-phase cerium-containing phase to obtain nanocomposites: $Ce_{0.8}Sm_{0.2}O_{1.9}$,[264 – 267] $Nd_{0.2}Ce_{0.8}O_{1.9}$,[267] $Ce_{0.9}Gd_{0.1}O_{1.95}$ and $Ce_{0.8}Gd_{0.2}O_{1.9}$,[268 – 270] $Ce_{0.9}Eu_{0.1}O_{2-\delta}$,[271] $Ce_{0.85}Er_{0.15}O_{2-\delta}$, $Ce_{0.85}La_{0.15}O_{2-\delta}$, $Ce_{0.95}Sr_{0.05}O_{2-\delta}$,[272, 273] $Ce_{0.95}Ca_{0.05}O_{2-\delta}$,[274, 275] $Ce_{0.8}Gd_{0.05}Y_{0.15}O_{1.9}$,[276] $Ce_{0.8}Sm_{0.1}Nd_{0.1}O_{1.9}$[277] and $Ce_{0.8}Sm_{0.2-x}Ca_xO_{2-\delta}$.[278, 279] The electrical properties of composites are determined mainly by the salt component properties. The key factors are the composition,[280, 281] salt percentage in the composite,[282, 283] and its formation temperature.[284] Synthesis of composite ceria-based electrolytes is performed using, along with carbonates, chlorides[285, 286] and sulfates;[287, 288] however, the number of such studies is much smaller.

Salt nanocomposites can be fabricated in different ways. The most widespread technique is the two-step method, in which a ceria-based electrolyte is first synthesized and then mixed with a salt (or separately prepared mixture of salts), after which a composite is formed by pressing with subsequent annealing and quenching (or without it) or by hot pressing. The one-step method of fabricating a composite (one-pot synthesis) implies simultaneous coprecipitation of all its components, synthesis and grinding, and further sample formation and sintering. Impregnation method is also used, in which a salt component is introduced into a porous electrolytic matrix to form a nanocomposite.

As an example, Fig. 23 *a* – *c* presents structure micrographs of typical composite SDC20 – LNC52/48 [LNC52/48† corresponds to the composition $(Li_{0.52}Na_{0.48})_2CO_3$] with different carbonate phase contents, obtained by the conventional two-step method with a final sintering temperature of 650 °C.[289] Nanoparticles of SDC electrolyte, synthesized by hydroxide coprecipitation, are uniformly distributed in the nanocomposite; particle – par-

† Hereinafter the slash indicates a molar ratio of components in a binary salt.

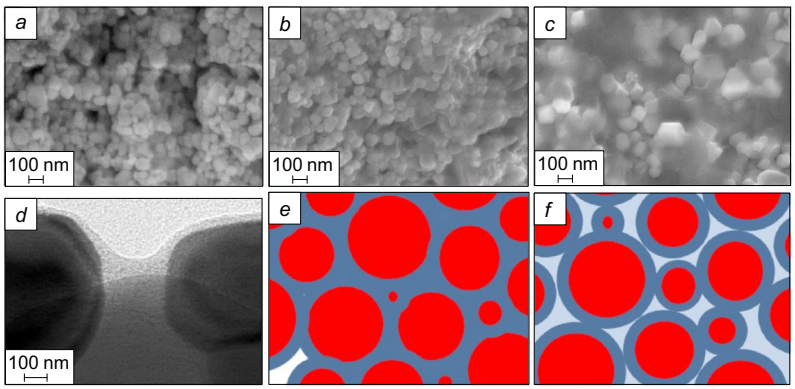


Figure 23. (*a* – *d*) Micrographs of composite SDC20 – LNC52/48 with carbonate phase contents of (*a*) 30, (*b*) 50, and (*c*) 60 vol.% and (*d*) particle with a core/shell structure in the composite. (*e*, *f*) Schematic structures of composites with (*e*) subcritical and (*f*) supercritical carbonate phase content.[289] Published with permission of Elsevier.

ticle voids are filled with carbonate. The carbonate shell with a thickness of ~ 6 nm is rigidly connected with SDC particle [Fig. 23 *d*, carbonate content 50 vol.% (25 wt.%)]. With an increase in the carbonate volume fraction the shell thickness continues to increase until reaches a critical value, depending on the interphase interaction force (Fig. 23 *e*). A composite with a high carbonate content has a three-dimensional structure with randomly distributed electrolyte particles, coated by a dense amorphous salt shell (core/shell structure); the voids between them are filled with the unbound carbonate phase (Fig. 23 *f*).

Comparative X-ray diffraction studies performed by different authors showed that the salt phase is mainly in the amorphous state at room temperature and, only when the carbonate content exceeds the critical value, weak peaks of a crystalline carbonate phase arise in X-ray diffraction patterns. Strong interphase interaction in salt ceria-based composites was confirmed using IR spectroscopy in a number of studies. In particular, IR spectra of carbonate composites exhibit splitting of the absorption band with a frequency of ~ 1450 cm^{-1}, which is characteristic of carbonate.[281, 290]

6.2. Modelling of the transport properties of salt composites

The generally accepted explanation of the increase in the conductivity of 3C composites is based on Mayer's theory of space charge regions.[291 – 293] The surface of cerium nanoparticles has an enhanced chemical activity, which manifests itself in the surface reduction of Ce^{4+} to Ce^{3+} and occurrence of different oxygen species (O_2^-, O^- and O^{2-}) on the surface. The latter actively interact with mobile carbonate cations, which results in their adsorption on the surface of cerium particles (Fig. 24). The electroneutrality of the system is provided by the formation of cation vacancies in the carbonate phase, which make it negatively charged. However, in view of the Coulomb interaction with positively charged interface, vacancies are concentrated in a thin Debye layer (~ 2 – 10 nm) near the particle surface, thus forming superionic conductivity channels. Having described interaction within a simple Coulomb model, Zhu *et al.*[291] estimated the mobility activation energies for O^- and O^{2-} in the interfacial region, which were found to be 0.2 and 0.1 eV, respectively (as compared with 1.0 eV for the bulk conductivity).

However, the multi-ion interaction in real systems may lead to some increase in the ionic conductivity activation energy. On the whole, the total conductivity of composites at temperatures above the superionic transition temperature does not exceed the conductivity of salt systems. For this reason, some researchers were doubtful about good prospects of composites.[294] At the same time, many studies confirmed the increase in the partial values of protonic and oxygen ionic conductivity in 3C composites in comparison with the reference solid electrolyte based on CeO_2, with simultaneous blocking of electronic conductivity. Due to this, one can use composite membranes in low-temperature SOFCs, reaching power density > 1 W and OCV > 1 V in the temperature range of 500 – 600 °C, *i.e.*, below the working temperatures of FCs based on molten carbonates (650 °C); this approach may help to solve the problem of electrode degradation.[258] Ricca *et al.*[295, 296] proposed a special strategy to form nanocomposites with predicted properties, which combines experimental investigations of their electrical properties and structure simulation by the

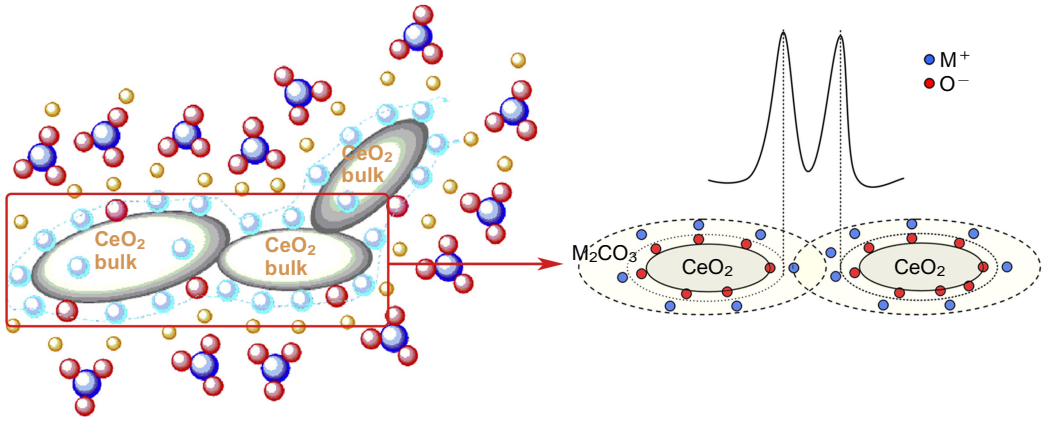


Figure 24. Schematic diagram of interaction between oxygen ions on the surface of particle of electrolyte (based on doped ceria) and carbonate phase cations. The sinusoid shows the change in the electric field at the boundary between two solid-phase particles. The figure was compiled by the authors based on the data of Ref. 291.

DFT method; it was applied to salt systems with a number of solid electrolytes.

6.3. Experimental study of the electrical properties of salt composites

A detailed review of the methods for studying the ionic conductivity of carbonate composite electrolytes (ac and dc measurements, analysis of gas composition in a cell with separated gas space), influence of atmosphere and measuring cell configuration, nature of electrodes and their configuration on sample, and many other parameters was presented by the research team of Lund and co-workers.[297] The authors noted that in most cases the total conductivity of composites was measured using ac impedance spectroscopy. The temperature dependences of the total electrical conductivity of a composite based on SDC20 with an optimal content of the carbonate phase LNC52/48 (50 vol.%) are presented in Fig. 25 *a*, which shows also the temperature dependences of the electrical conductivity of basic components and the theoretical electrical conductivity of composite, calculated from the phenomenological equations for the electrical conductivity of microscopically inhomogeneous materials.[298] In the temperature range of 500 – 650 °C, the experimental values of total conductivity are below the calculated ones. The authors explained this discrepancy by the decrease in the average migration rate of metal ions in a winding medium with randomly distributed solid electrolyte particles. At the same time, in the temperature range of 450 – 500 °C, the experimental values of the total conductivity of composite exceeded the theoretical ones, obtained with interphase interaction disregarded. This feature is explained as follows: due to the strong interphase interaction, the shell carbonate remains in the amorphous state even at temperatures below the melting point (49 °C), thus providing high mobility of charged particles. It should be noted that the transition temperatures (T_{trans}) in composites with binary and ternary salts are generally 20 – 30 °C below the melting temperatures (T_{melt}) of these salts or are equal to them, whereas in the case of simple salts the T_{trans} values for salt composites based on doped ceria are much lower than T_{melt} and T_{trans} for similar systems with CeO_2 (Ref. 299) and other oxide additives.[300]

The partial conductivity in salt composites is conventionally measured by the dc four-probe method.[297] The temperature dependences of the oxygen ionic and protonic conductivities, obtained by this method for LNC52/48 (composite SDC with 50 vol.% carbonate)[289] in oxygen and hydrogen atmospheres are presented, respectively, in Fig. 25 *b*,*c*. The experimental values exceed the theoretical ones, found disregarding the interphase interaction: by a factor of 10 for the protonic conductivity and twice as high for the oxygen ionic conductivity.

Having studied the concentration dependences of the oxygen ionic and protonic conductivities, the authors demonstrated that the conductivities of both types increase until the content of volume fraction reaches a critical value, equal to 43 – 45 vol.%, and then decrease with a further increase in the carbonate content. To calculate the conductivity of composite in the subcritical state, when it can be considered as a 3D structure with randomly packed spherical particles of the same type (see Fig. 23 *e*), the authors used the single-particle approximation of the Maxwell – Garnett effective-medium theory.[301] The electrical properties of composites with a carbonate content above critical are described within the Bruggeman model for a heterogeneous medium with randomly distributed particles of two types in the Landauer modification.[302, 303] The values of oxygen ionic and protonic conductivity of the surface layer (~6 nm thick) coating SDC crystallites were estimated by the authors within the aforementioned models to be, respectively, 46.0 and 97.0 mS cm^{-1} at 650 °C, which exceeds the corresponding values for the LNC phase — molten binary salt Li_2CO_3 – Na_2CO_3 (12.0 and 8.0 mS cm^{-1}) and the SDC phase (11.0 and 10^{-3} mS cm^{-1}).

For the SDC20-based nanocomposites, the highest values of total conductivity in air (at 550 °C) were obtained for compositions with 20 wt.% LNC52/48 (440 mS cm^{-1})[304] and 30 wt.% $(Li_{0.321}Na_{0.334}K_{0.345})_2CO_3$ (410 mS cm^{-1}).[305] Large values of total conductivity were also observed for a composite obtained by impregnation of LNC52/48 into a ceramic matrix SDC20 (up to 530 mS cm^{-1} at a carbonate content of 40 vol.%).[306, 307]

On the whole, the results of measuring conductivities, including partial ones, performed by different research teams and even obtained for similar systems, differ significantly. Until now, the question about the dominance of a particular conductivity type in these systems is debated: either this is oxygen ionic conductivity, which is intrinsically inherent in composite components, or protonic conductivity, which is due to external factors. In particular, Wang and co-workers[274, 308, 309] showed that the protonic conductivity in some composites based on SDC and $Ce_{0.8}Ca_{0.2}O_{1.8}$ (CDC) with different sodium carbonate (NC) contents

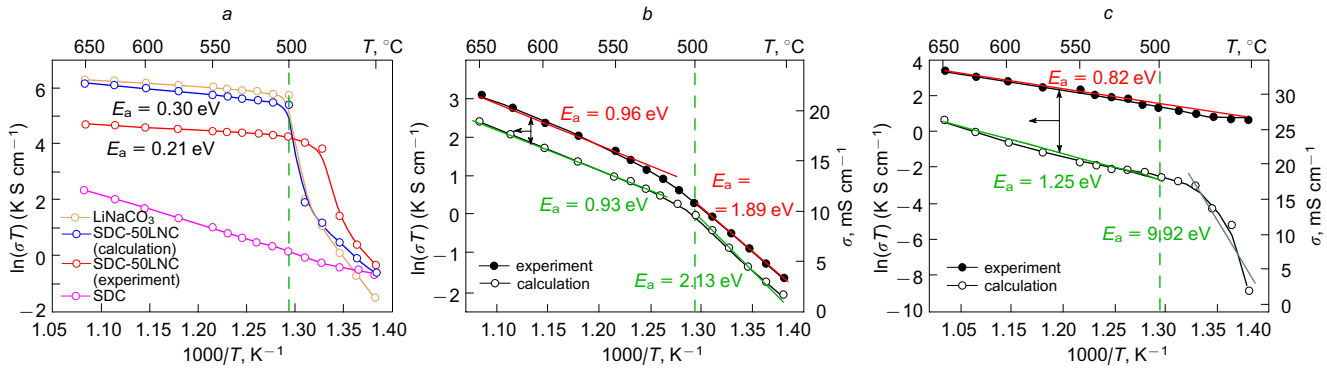


Figure 25. Experimental and theoretical (calculated) temperature dependences of the (*a*) total and partial (*b*) oxygen ionic and (*c*) protonic conductivities of composite SDC20 with 50 vol.% LNC52/48.[289] Published with permission of Elsevier.

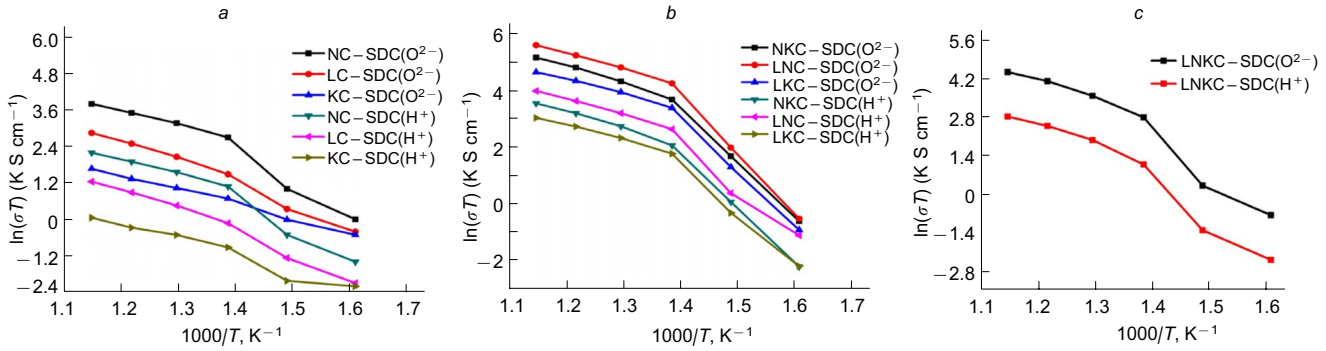


Figure 26. Arrhenius dependences of partial conductivity, measured in oxygen- and hydrogen-containing media, for composites based on SDC20 with (*a*) single, (*b*) binary, and (*c*) ternary salts.[312] See text for phase designations. Published with permission of American Chemical Society.

(σ_{H^+}), measured in a reducing atmosphere (specifically, in hydrogen or hydrogen-containing mixtures), exceeds greatly the oxygen ionic conductivity ($\sigma_{O^{2-}}$) measured in air or oxygen (for example, for composite SDC20 with 10% NC, the values of σ_{H^+} and $\sigma_{O^{2-}}$ at 500 °C are, respectively, 0.063 and 0.004 S cm^{-1}). The authors proposed an empirical model of increasing the protonic conductivity in carbonate composite, which they referred to as the Swing Model. The protons arriving at the composite electrolyte placed in a reducing medium (from the anode side of SOFC) can form metastable hydrogen bonds with oxygen ions on the SDC surface during interaction with CO_3^{2-} groups. An increase in temperature above the critical point (at which carbonate becomes amorphous) leads to enhanced vibrations of C – O bond (stretching and bending) and increases mobility and rotation of CO_3^{2-} groups. These motions provide fast break and formation of hydrogen bonds in the carbonate shell and enhance proton transport, whose driving force is the proton concentration gradient. Carbonate ions play a role of a bridge, providing proton motion from one bond to another. The authors explained the possibility of this mechanism by the presence of oxygen pairs on the cerium surface with a bond length close to that in CO_3^{2-} groups. Therefore, when oxygen pairs on the cerium surface form bonds with protons, the latter can easily be transported *via* break of the metastable H – O bonds. The carbonate shell plays a multiple role: acts as a phase retaining electrolyte in the nanoscale state and a phase facilitating the proton transport; it also blocks electronic conductivity (the value measured by the authors using the Hebb – Wagner polarization method in a gas mixture (5% H_2 + 95% N_2) was 0.2 mS cm^{-1} at 550 °C, *i.e.*, ~0.3% of the level of protonic conductivity at this temperature (63 mS cm^{-1}).

The swing model turned out to be inefficient for systems with binary and ternary salts, which do not exhibit such a large difference in the oxygen ionic and protonic conductivities. In particular, the σ_{H^+} value for the composite SDC20 with 20 wt.% binary salt LNC66.7/33.3, measured in hydrogen, is approximately twice as large as $\sigma_{O^{2-}}$ (40 and 18 mS cm^{-1}, respectively, at 550 °C).[310] For SDC20 composites with different contents of binary salt LNC52/48, the σ_{H^+} value measured by the four-probe method exceeds only slightly[289] $\sigma_{O^{2-}}$ (or is even lower).[311]

Ali *et al.*[312] investigated composites with different salts obtained by the one-step method: Na_2CO_3 – SDC20 (NC – SDC), K_2CO_3 – SDC20 (KC – SDC), Li_2CO_3 – SDC20 (LC – SDC), (Li_2CO_3 – Na_2CO_3) – SDC20 (LNC – SDC), (Na_2CO_3 – K_2CO_3) – SDC20 (NKC – SDC), (Li_2CO_3 – K_2CO_3) – SDC20 (LKC – SDC) and (Li_2CO_3 – Na_2CO_3 – K_2CO_3) – SDC20 (LNKC – SDC). Among the single systems (Fig. 26 *a*), the highest conductivity (measured by impedance spectroscopy) was obtained for NC – SDC20 (52 mS cm^{-1} at 600 °C). Among the systems with a binary salt (Fig. 26 *b*) the highest conductivity was found for LNC – SDC20 (310 mS cm^{-1}) and for the ternary system (Fig. 26 *c*) LKC – SDC20 (94 mS cm^{-1}).

For all investigated systems, the $\sigma_{O^{2-}}$ value, measured by the dc four-probe method, exceed the σ_{H^+} values. Kinks in the Arrhenius dependences (except for the dependence $\sigma_{O^{2-}}$ for composite KC – SDC) were observed at ~ 450 °C for single and binary salt composites (despite the difference in the melting points of simple salts and eutectics) and at 400 °C for the ternary system. Previously, Ferreira *et al.*[270] suggested that protons interacting with CO_3^{2-} diffuse through the carbonate phase in the form of HCO_3^-. In this case, oxygen ions can be dissolved in the carbonate phase, according to following equilibrium equation:

$$CO_3^{2-} \rightleftharpoons CO_2 + O^{2-} \qquad (29)$$

Thus, oxygen ions can be transported not only through the bulk of solid electrolyte but also through the carbonate phase. The authors explain the dominance of oxygen ionic conductivity (observed in the aforementioned studies) by the fact that O^{2-} anions in both phases are structural (or internal) charge carriers, whereas H^+ ions are external carriers, depending on the gas-phase conditions.

6.4. SOFCs based on salt composites and ways to increase their operation efficiency

A schematic diagram of operation of an SOFC with a composite 3C membrane is presented in Fig. 27. The cooperative mechanism of multi-ion conductivity in 3C composites makes it possible to obtain high SOFC output powers at relatively low temperatures. The powers of SOFC with a composite membrane having a thickness from 200 to 900 μm and with SDC20 electrolyte ~10 μm thick are comparable. It was suggested by Asghar *et al.*[279] that, having developed adequate methods for fabricating thin-film composite membranes, one can increase the power density of SOFC with a composite 3C membrane to 2.5 W cm^{-2} at 550 °C. In addition, the OCVs for low-temperature SOFCs with a composite membrane (generally,

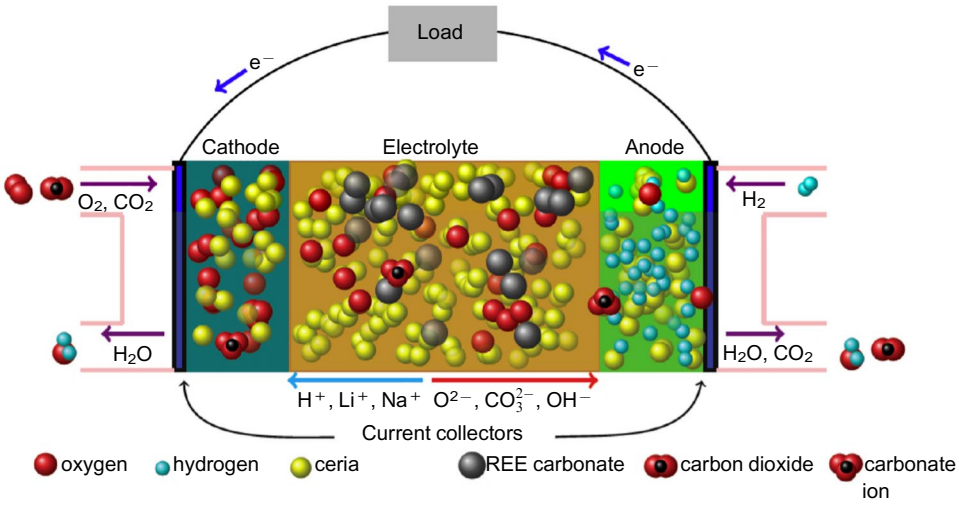


Figure 27. Schematic diagram of operation of an SOFC with a composite 3C membrane; a CO_2-containing mixture and hydrogen are used as cathode and anode gases, respectively. The figure was compiled by the authors based on the data of Ref. 279.

$\sim$1 – 1.1 V or more at temperatures of 550 – 600 °C) exceed those for SOFCs with a single-phase membrane based on doped cerium ($\sim$0.8 – 0.9 V) in this temperature range due to the decrease in the electronic conductivity of composite. Some authors noted water release in this cell from both cathode and anode sides, which proves indirectly the existence of mixed oxygen ionic and protonic conductivity of 3C composites.

Di *et al.*[304] investigated the influence of humidity on the OCV in SOFCs with a composite membrane of the SDC20 – LNC52/48 composition, using air and hydrogen as cathode and anode gases, respectively. The maximum OCVs, found at the same minimum water content in the anode and cathode channels (0.6 vol.%, 1.053 and 1.036 V at 500 and 600 °C, respectively), decreased with an increase in the humidity of anode and cathode gases (Table 6). The OCVs determined by the authors are smaller than the calculated ones (1.207 V) because of the low density of the membrane obtained by mixing components. It was also noted that OCV decreases at temperatures $< T_{melt}$ of the carbonate mixture (0.96 V at 450 °C) due to the even larger decrease in membrane density. The density and electrical properties of composite membranes can be improved by increasing the sintering time (up to 20 h), using low vacuum during their formation, and applying one-step chemical (as well as infiltration) methods to form a composite. The infiltration method allows for increasing the mechanical strength of membrane.[265]

The SOFC output increases when using a gas mixture containing carbon dioxide as an oxidant. In particular, it was shown by Li's team[313, 314] that the replacement of air with a mixture of oxygen and carbon dioxide (1 : 1 vol.%) provides an increase in the output of an SOFC with a composite membrane 70 mol.% SDC20 – 30 mol.% LNC50/50 due to the increase in both power and OCV (at 650 °C, respectively, from 1.0 W cm^{-2} and 1.03 V to 1.7 W cm^{-2} and 1.13 V). One can suggest the following generalized mechanism of ion transport in a composite membrane, provided that carbon dioxide is present in the cathode gas:

— transport of O^{2-} through the bulk of particles and grain boundaries in the electrolyte based on doped CeO_2, similar to that in conventional SOFCs;

— interfacial oxygen ionic conductivity with participation of the carbonate phase;

— occurrence of H^+ due to the dissociation of hydrogen molecules on the anode and protonic conductivity through the interfaces with participation of the carbonate phase (possible mechanisms of protonic conductivity were considered in the previous section);

— transport of CO_3^{2-} through the bulk of the carbonate phase.

Thus, the carbonate phase is an important intermediate stage in the implementation of oxygen ion and proton transport in SOFCs based on 3C composites. An essential aspect is the choice of electrodes for low-temperature SOFCs with a composite 3C membrane. Lithiated NiO is often used as a cathode. Proton transport in the layered structure of this compound facilitates expansion of the three-phase boundary and decrease in the polarization resistance of cathode contacting with the composite, which has a rather high protonic conductivity. Thus, promising candidates can be cathode materials developed both for molten carbonate fuel cells (MCFCs) and for low-temperature fuel cells based on proton-conducting ceramic electrolytes (PCFCs). In addition, conventional cathodes with a perovskite structure, compatible with ceria-based electrolytes, can be used as cathodes for SOFCs with a composite membrane; their activity at low operating temperatures is increased by modifying with additives of carbonate or 3C composite.

The mechanism of oxygen reduction reaction on a fuel cell cathode in the presence of the carbonate phase was studied repeatedly, both experimentally and theoretically with application of DFT.[315 – 317] Reactions with formation of intermediate CO_4^{2-} and CO_5^{2-} ions were shown to be thermodynamically more favourable; *i.e.*, the presence of

Table 6. Influence of the humidity of cathode (air) and anode (hydrogen) gases on the OCV of an SOFC with a composite membrane 80 wt.% SDC20 – 20 wt.% LNC52/48 (185 μm).[304]

H_2O content (vol.%)		OCV, V	
anode gas	cathode gas	at 500 °C	at 600 °C
0.6	0.6	1.053	1.036
0.6	2.3	1.045	1.022
2.3	2.2	1.017	1.012
2.3	2.3	1.009	1.002

the carbonate phase at the three-phase boundary accelerates oxygen reduction due to the formation of alternative channels of oxygen transport from the cathode to the electrolyte. A 'cogwheel' mechanism, implying the formation – break of $O-CO_3^{2-}$ bonds, was proposed to describe the transport of CO_4^{2-} from the carbonate surface to the interface. The introduction of the carbonate phase has some advantages over the infiltration method commonly adopted for the cathode activation. In particular, it was shown[318] that activation of LSCF – GDC cathode by introducing carbonate LKC62/38 (LKC is the binary salt $Li_2CO_3-K_2CO_3$) in amount of 3.6 mg cm^{-2} led to a decrease in the polarization resistance by a factor of 20 – 40 and contact resistance by a factor of 2 – 3 in a temperature range of 550 – 650 °C, whereas in the case of infiltration of LSCF into a porous matrix the polarization resistance was reduced by a factor of 2 – 10 without affecting the contact resistance.

The mechanism of oxygen reduction in this modified electrode is schematically presented in Fig. 28. Two ways of oxygen reduction reaction in a MIEC-SOFC electrode modified by the carbonate phase (MC) can be selected. The first (indicated by dotted arrows) includes adsorption from the gas phase, dissociation, and diffusion of oxygen over the MIEC-phase surface (O_s), incorporation of oxygen and its transport through the MIEC-phase bulk to the electrolyte in the form of O^{2-} ions, and charge transfer through the MIEC/electrolyte interface. The second way implies participation of the carbonate phase and can be presented as follows (the numbers of stages are indicated in black circles in Fig. 28):[318]

stage 1: oxygen chemisorption from the gas phase on the MC/O_2 interface

$$CO_3^{2-}(MC) + O_2 = CO_5^{2-}(MC) \quad (30)$$

stage 2: interaction between CO_5^{2-} and CO_3^{2-} in the bulk of the carbonate phase

$$CO_5^{2-}(MC) + CO_3^{2-}(MC) = CO_4^{2-}(MC) \quad (31)$$

stage 3: ion transport in the carbonate bulk to the MC/MIEC interface

$$CO_4^{2-}(O_2/MC) = CO_4^{2-}(MC/MIEC) \quad (32)$$

stage 4: charge transfer on the MC/MIEC interface

$$CO_4^{2-}(MC) + 2e^-(MIEC) = CO_3^{2-}(MC) + O^{2-}(MIEC) \quad (33)$$

stage 5: charge transfer through the MIEC/electrolyte interface

$$O^{2-}(MIEC) = O^{2-}(electrolyte) \quad (34)$$

It should also be noted that the method of fabricating perovskite cathode materials using molten salts is being actively developed. This technique makes it possible to obtain highly dispersed materials;[319] cathodes can be formed based on these materials without the stage of preliminary sintering with the electrolyte.

Conventionally, the following oxides are applied in SOFC anodes with a composite 3C membrane: NiO, ZnO – NiO, $Li_2O-NiO-ZnO$, and $Li_2O-NiO-CuO-ZnO$. CuO and ZnO additives are used to reduce the NiO solubility in carbonate and improve the electrochemical activity and stability of anode. Such anodes can successfully operate in cells based on 3C-composite membranes. In particular, Raza *et al.*[320] obtained the following values of power density for a single SOFC with a scaled (60 × 60 mm) electrolyte SDC20 – NC and a nanocomposite anode

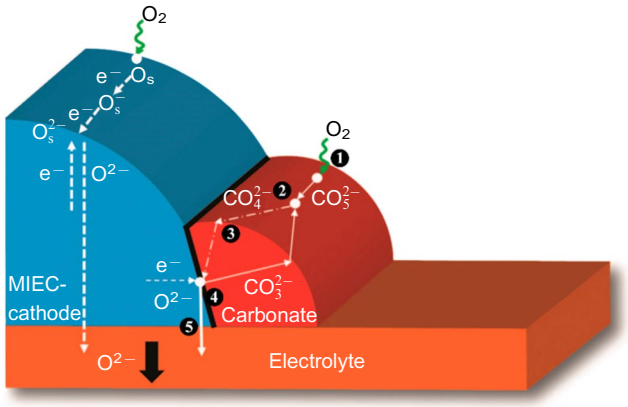


Figure 28. Schematic mechanism of oxygen reduction reaction in an SOFC perovskite cathode, modified by carbonate additives contacting with oxygen-conducting electrolyte. CO_5^{2-} and CO_4^{2-} are intermediate species, playing the role of fast absorber and carrier of oxygen. See text for designations *1* – *5*. The figure was compiled by the authors based on the data of Ref. 318.

LiNiCuZn: 970, 300, 600, and 550 mW cm^{-2} at 550 °C (using, respectively, hydrogen, biogas, biomethanol, and bioethanol as a fuel). Gao *et al.*,[321] who used a mixture of methanol and water vapour (1 : 1) as a fuel, obtained power of 603 mW cm^{-2} at 600 °C for an SOFC with the SDC – LNC53/47 composite electrolyte and the LiNiCuZn anode.

Examples of SOFCs with different salt composites, including sulfates and chlorides, which were not considered thoroughly in the review, can be found in Table 7. Data obtained by different research groups are presented for objectivity. An analysis of these results showed that high powers can be obtained only by optimizing the fabrication technology and decreasing the electrolyte thickness, as well as by optimizing the composition and microstructure of electrodes. An interesting comparison of SOFCs with salt composites and MCFCs was performed in the review by Tomczyk.[322] In contrast to SOFCs, lower current densities were obtained in MCFC because of the limited region of electrode reaction and low solubility of oxygen and hydrogen in molten carbonates. In opinion of the author, MCFCs are advantageous for stationary setups, whereas SOFCs, including those with carbonate electrolytes, can also be applied as portable devices.

7. Methods aimed at increasing the SOFC performance by forming heterostructures

Recently the research in the field of formation of nanoscale heterostructures of various types for functional SOFC units (cathode, electrolyte, anode) has been actively developed. The purpose is to increase significantly the output due to the intensification and expansion of the electrode-reaction zone, increase the ionic conductivity, and reduce the polarization loss with a decrease in working temperature. The modern state of art in the research in this field is described, for example, in reviews by Zhao *et al.*[323] and Garbayo *et al.*[324]

7.1. Formation principles and properties of electrolytic heterostructures

Intense development of the studies devoted to the nature and mechanisms lying in basis of the effects of developed

Table 7. Characteristics of SOFCs with salt composite membranes.

Membrane (thickness)	Gas medium (anode/cathode)	T, °C	OCV, V	Specific power density, mW cm^2	Ref.
Solid-oxide cells with a 3C membrane					
Anode: 50 vol.% NiO – *50 vol.%* (SDC20 – LNC 50/50), *cathode: 50 vol.%* $LiNiO_2$ – *50 vol.%* (SDC20 – LNC 50/50)					
95SDC20 – 5NC (~0.2 mm)	H_2/air	550	0.93	514	308
90SDC20 – 10NC (~0.2 mm)	H_2/air	550	0.96	833	308
85SDC20 – 15NC (~0.2 mm)	H_2/air	550	0.93	729	308
80SDC20 – 20NC (~0.2 mm)	H_2/air	550	0.88	613	308
Anode: 50 vol.% NiO – *50 vol.% electrolyte (0.5 mm), cathode: 50 vol.%* $LiNiO_2$ – *50 vol.% electrolyte (0.25 mm)*; Ag *collector*					
70 SDC20 – 30 LNC50/50 [a]					
GN (0.5 mm)	$H_2/CO_2 – O_2$	650	1.15	607	264
OC (0.5 mm)	$H_2/CO_2 – O_2$	650	1.10	1266	264
SG (0.5 mm)	$H_2/CO_2 – O_2$	650	1.19	1121	264
OC (0.25 mm)	$H_2/CO_2 – O_2$	450 – 650	1.03 – 1.13	350 – 1704	264
OC (0.25 mm)	H_2/air	450 – 650	1.00 – 1.00	300 – 1000	264
Anode: NiO – *electrolyte (ratio is not indicated), cathode*: $LiNiO_2$ – *electrolyte (ratio is not indicated)*					
SDC20 – LNC52/48 (4 : 1wt.)	H_2/air	500	1.05	432	304
	H_2/air	550	1.03	563	304
	H_2/air	600	1.03	590	304
Anode: 50 wt.% LiNiZnCu – *35 wt.% electrolyte — 7.5 wt.% EC – 7.5 wt.% PVA, cathode: 50 wt.%* LSCF – *35 wt.% electrolyte – 7.5 wt.% EC – 7.5 wt.% PVA;* Au *collector*					
70 Ca – SDC – 30 NLKC33.4/32.1/34.5 (0.9 mm)	H_2/air – CO_2	450	0.92	260	279
	H_2/air – CO_2	500	1.02	560	279
	H_2/air – CO_2	550	1.14	1030	279
Anode: 45 wt.% NiO – *45 wt.% electrolyte – 10 wt.% EC, cathode: 45 wt.%* LSCF – *45 wt.% electrolyte – 10 wt.% EC*					
70 SDC15 – 30 NLKC33.4/32.1/34.5 (0.9 mm)	$H_2/CO_2 – O_2$	550	1.2	1100	305
	H_2/air	550	1.05	–	305
Anode: NiO – *electrolyte – polystyrene, cathode:* $LiNiO_2$ – *electrolyte – polystyrene*					
75 GDC20 – 25 LNC	H_2/air	450	0.79	44	268
	H_2/air	500	0.77	54	268
	H_2/air	550	0.89	92	268
Anode and cathode: 50 wt.% $LiNiO_2$ – *50 wt.% electrolyte;* Ag *collector*					
60 $Ce_{0.8}Gd_{0.05}Y_{0.15}O_{1.9}$ – 40 LNC52/48 (0.7 mm)	H_2/air	550	1.02	520 [b] (420) (300)	290
Anode: 50 vol.% NiO — *40 vol.% electrolyte – 10 vol.% starch, cathode:* $LiNiO_2$ – *electrolyte*					
70 GDC10 – 30 LKC72.7/27.3	H_2/air	600	~0.95	60	269
	H_2/air	550	~1.0	55	269
Solid-oxide fuel cells with a composite 3C membrane					
Anode and cathode: LiCuNiZnO — *electrolyte (ratio is not indicated);* Ag *collector*					
SDC20 – NC (co-precipitation, ratio is not indicated)	Fuel:				
	H_2	550	1.1	970	320
	biogas [å]	550	0.8	300	320
	CH_3OH	550	0.95	550	320
	C_2H_5OH	550	1.0	530	320

Table 7 (continued).

Membrane (thickness)	Gas medium (anode/cathode)	T, °C	OCV, V	Specific power density, mW cm^2	Ref.
Solid-oxide fuel cells with a composite 3C membrane					
Anode and cathode: 50 vol.% LiCuNiZnO — *50 vol.% electrolyte*					
SDC + *n* wt.% LNC53/47					
n = 10	$CH_3OH + H_2O$	500	0.871	213	321
n = 10	$CH_3OH + H_2O$	600	0.835	390	321
n = 20	$CH_3OH + H_2O$	500	0.858	295	321
n = 20	$CH_3OH + H_2O$	600	0.85	516	321
n = 25	$CH_3OH + H_2O$	500	0.803	431	321
n = 25	$CH_3OH + H_2O$	600	0.810	603	321
n = 30	$CH_3OH + H_2O$	500	0.837	376	321
n = 30	$CH_3OH + H_2O$	600	0.848	577	321
Solid-oxide fuel cells with a composite 3C membrane based on sulfates					
Anode: NiO – (GDC10 – LCS) *(3 : 2 wt.)*, *cathode:* $LiNiO_2$ – (GDC10 – LCS) *(3 : 2 wt.)*; Ag *collector*					
GDC10 – Li_2CO_3 – Li_2SO_4 (LCS61.1/38.9)	H_2/air	600	1.01	272	288
Anode: NiO – GDC10 *(ratio is not indicated)*, *cathode: 40 wt.%* LSM – *60 wt.%* GDC10					
GDC10	H_2/air	600	0.86	113	288
Anode and cathode: 20% Pd – *80%* Ag					
$Ce_{0.8}Yb_{0.1}Gd_{0.1}O_{2-\delta}$ – Li_2SO_4 – K_2SO_4 (LKS) (4 : 1 wt.) (1 mm)	H_2/air	700	~1.1	197	287
$Ce_{0.8}Yb_{0.1}Gd_{0.1}O_{2-\delta}$ (1 mm)	H_2/air	700	~1.0	39	287
Solid-oxide fuel cells with a composite 3C membrane based on chlorides					
Anode: 40 wt.% NiO – *60 wt.%* GDC10 *(0.3 mm)*, *cathode*: $LiNiO_2$ *(0.5 mm)*					
GDC10 – LiCl – $SrCl_2$	H_2 + 3% H_2O/O_2	550	~0.83	260	285
(LSCl50/50) (12 : 5)	H_2 + 3% H_2O/O_2	590	0.85	330	285
(0.3 – 0.5 mm)	H_2 + 3% H_2O/O_2	625	–	510	285
Anode and cathode: 20% Pd – *80%* Ag					
80 EDC20 – 20 KCl – NaCl (CNCl50/50) (1 mm)	H_2/O_2	700	~1.05	187	286
EDC20 (1 mm)	H_2/O_2	700	~1.07	30.9	286

Note. Designations are as follows: EDC20 — $Ce_{0.8}Er_{0.2}O_{2-\delta}$; PVA is polyvinyl alcohol; EC is ethyl cellulose. [a] Electrolyte SDC20 was obtained by nitrate combustion with glycine (GN), oxalate co-precipitation (OC), sol – gel (SG) method. [b] Degradation after 210 and 390 min is shown. [c] Biogas composition (vol.%): H_2 (25) + CH_4 (25) + CO_2 (25.1) + N_2 (24.9).

interface on electrochemical transport processes began after the publication of Garcia-Barriocanal *et al.*[325] They reported that the ionic conductivity increased by 8 orders of magnitude along the interface in an YSZ layer with a thickness of 1 – 62 nm, located between $SrTiO_3$ (STO) layers with a thickness of 10 nm, when layers are formed by epitaxial growth on a single-crystal STO substrate. The set conductivity value reached 40 S cm^{-1} at a temperature of 277 °C and YSZ thickness is 1 nm. Interpretation of the obtained results was debated in some studies. For example, Guo [326] suggested that the revealed increase in conductivity is due to the presence of p-type electronic conductivity of strontium titanate.

Cavallaro *et al.*[327] reported the results of studying the conductivity of three-layer structure STO (10 nm)/YSZ (1 nm)/STO (10 nm). The dependence of conductivity on the partial oxygen pressure was found to have the form $\sigma \sim p_{O_2}^{0.2}$, which is close to the dependence of p-type electronic conductivity, characteristic of acceptor-doped strontium titanate. To refine the mechanisms explaining the obtained experimental results on the increased conductivity of heterostructures, Gale [328] performed a theoretical analysis using the DFT, molecular dynamics, and Monte Carlo methods and atomistic simulation with application of lattice dynamics methods. The following effects were considered as possible factors responsible for the increase in conductivity:

— influence of mechanical stress near the interface on the change in the configuration of electron energy levels;
— change in mobility and vacancy concentration;
— occurrence of space-charge region;
— change in the interaction between vacancies.

Some theoretical models developed by Schichtel *et al.*[329] provided quantitative estimates of the change in near-interface ionic conductivity, which demonstrated the influence of lattice mismatch and occurrence of mechanical stress. It was found that the ionic conductivity on the interface increases

by a factor of ~460 as compared with the bulk value. Kushima and Yildiz[330] performed a Monte Carlo simulation and found the optimal strain of YSZ lattice at which the diffusion coefficient of oxygen ions is maximum. An increase in the diffusion coefficient by a factor of 10^3 occurs at a strain of 4% and a temperature of 127 °C, which is much lower as compared with the data reported previously by Garcia-Barriocanal *et al.*[325]

Atomistic simulation of the influence of strained state on the transport characteristics of electrolytic materials based on CeO_2 was performed by De Souza *et al.*[331] using the GULP software, lattice dynamics methods, and empirical pair-interaction potential, which were described by Gale.[328] It was established that, at a lattice strain of 4%, the conductivity of CeO_2-based electrolyte at a temperature of 227 °C may increase by a factor of $\sim 10^4$ due to the change in activation energy. According to the calculations, a similar increase in ionic conductivity occurs for the $SrTiO_3/YSZ/SrTiO_3$ heterostructure. As a result, it was suggested by Garcia-Barriocanal *et al.*[325] that the elevated conductivity is due to either electron transport or the influence of other mechanisms, for example, formation of a space-charge region. The authors made an emphasis on the necessity of further theoretical and experimental studies of the processes occurring in the heterostructures promising for increasing SOFC efficiency.

It is noteworthy that nanoscale effects arise also in single-phase electrolyte films with a decrease in the grain size to 10 – 20 nm. For example, the ionic conductivity of thin films based on YSZ[332] and the electronic conductivity of electrolyte films based on CeO_2, both in a reducing atmosphere and at high partial oxygen pressure, can be increased with a decrease in the grain size to ~10 nm.[333]

To use most efficiently the nanoscale effects arising at the interface between structural elements, along with nanocomposites having a core/shell structure and composite structures in the form of a mixture of particles, their thin-film modifications have been proposed: a multilayer structure with a nanoscale layer thickness and vertically aligned nanocomposite (VAN) films (Fig. 29). VAN films are a relatively new type of thin-film nanomaterials having a columnar structure, in which the material of one phase alternates with the material of another, and the interface planes are oriented perpendicular to the film plane. The transverse size of single-phase structural elements is ~10 – 20 nm. The ion transport along interfaces can be significantly enhanced in these films, due to which new-generation SOFCs with a lower working temperature can be designed.

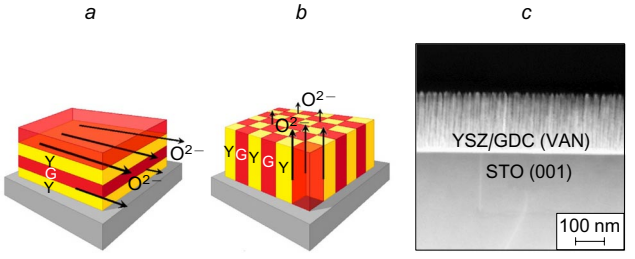


Figure 29. Schematic diagrams of (*a*) multilayer and (*b*) vertically aligned heterostructures YSZ (Y)/GDC (G) and (*c*) a micrograph of a VAN microstructure.[211] Published with permission of Elsevier.

VAN films have a high density of interfacial regions per unit volume. This fact determines the difference between the properties of these films and the properties of corresponding bulk materials. In particular, Su *et al.*[211] reported the results of studying an SOFC with a two-phase GDC – YSZ electrolyte layer, formed as a VAN structure, and showed an increase in the electrolyte conductivity by 50% relative to the conductivity of single-phase SDC layer and by two orders of magnitude relative to the YSZ conductivity. With a VAN structure formed between the YSZ and GDC layers in an SOFC with a carrier anode, the OCV turned out to be 1.04 V at a temperature of 700 °C, and the power densities were 0.432, 0.623, and 0.783 W cm^{-2} at 700, 750, and 800 °C, respectively. An YSZ – GDC cell without a VAN structure exhibited lower power densities: 0.227, 0.376, and 0.571 W cm^{-2} at 700, 750, and 800 °C, respectively.

Based on the above results, one can conclude that the application of VAN structures is more efficient at lower working temperatures (the power density increases by factors of 1.9, 1.6, and 1.4 at 700, 750, and 800 °C, respectively). When a VAN structure was formed from above on the GDC layer, between the cathode layer and electrolyte, the power density was found to be 0.488, 0.694, and 0.883 W cm^{-2} at 700, 750, and 800 °C, respectively. The electron micrograph (Fig. 29 *c*) shows that the VAN structure and GDC layer have comparable lengths; this factor may limit the increase in power caused by the increased ionic conductivity in the VAN structure.

Some remarks concerning the expediency and efficiency of application of YSZ/GDC heterostructures were made by Näfe,[334] who noted, in particular, that the results obtained by Su *et al.*[211] did not show any significant increase in the SOFC power and conductivity of heterostructures.

Experimental studies aimed at refining the character of conductivity in heterostructures and implemented interface mechanisms were continued. In particular, Yang *et al.*[335] studied the parameters of a heterostructure film with a thickness ~1 μm, which consisted of columnar SDC crystallites in an STO matrix, formed on a neodymium-doped STO substrate. The transverse diameter of SDC crystallites was ~30 μm. The local ion and electron transport characteristics of the SDC/STO heterostructure were studied by scanning probe microscopy with a spatial resolution of ~10 nm. The ionic conductivity was found to increase not only in the near-interface region but also in the entire volume of columnar SDC crystallite; the maximum conductivity was observed at its centre. A high degree of crystallinity of the structure formed in SDC throughout the entire thickness of SDC/STO film was noted. These results confirmed the increase of the conductivity in the heterostructure; nevertheless, they contradict the generally accepted interpretation, according to which conductivity increases specifically along the boundary between phases.[325]

The mechanism of formation of vertically aligned nanocomposite films is based on the self-assembly of a columnar structure growing from the gas phase on a single-crystal substrate. The growth methods are pulsed laser deposition,[336] as well as molecular-beam epitaxy and its modifications,[337] in which the initial material or components of desired material are evaporated with subsequent condensation on a heated substrate. The conditions of spontaneous formation of such structures were analyzed by MacManus-Driscoll.[338] The formation of nanoscale heterostructures was considered in that study from the point of view of

spinodal decomposition, at which a homogeneous system is separated into phases.

Spinodal decomposition arises when the formation of a homogeneous system at high temperatures is energetically favourable for minimizing free energy, and sharp cooling causes delamination of system with segregation of separate initial phases due to the increase in fluctuations. Spinodal decomposition of a homogeneous system occurs throughout the entire volume, and there is no need for activation energy to form new-phase nuclei.[339] Of particular interest are the mechanisms of formation of an ordered periodic nanostructure during spinodal decomposition in processes of condensation and solid solution cooling. The influence of the dependence of solubility of individual phases in a heterogeneous system on the temperature and ratio of mixture components with different lattice parameters and the strained state at the interface on these mechanisms was noted by MacManus-Driscoll.[338] The mixing of individual components of oxide systems depends on the ratio of ionic radii of cations, the difference in which excludes component mixing at lowered mixture temperatures. A columnar structure with arrangement of individual phases in the checkerboard pattern is formed during spinodal decomposition. Maybe, it is the strained state at boundaries between them that determines this peculiarity of periodic structure formation.[340]

7.2. Increasing the electrode response in heterostructural systems

The efficiency of SOFC oxygen electrodes can be increased using heterostructures, in particular, those combining materials with a perovskite structure and structure of Ruddlesden – Popper phases ($ABO_3 - A_2BO_4$). Based on the results of studying the isotopic exchange in test layered materials $La_{2-x}Sr_xCoO_4/La_{1-x}Sr_xCoO_3$ ($LSC_{214} - LSC_{113}$) on a $Ce_{0.9}Gd_{0.1}O_{1.95}$ (GDC) substrate, Sase *et al.*[341] proposed a composite layered structure of cathode with an upper porous layer LSC_{214} and dense sublayer LSC_{113}. The results of subsequent experimental studies confirmed the enhancement of electrode kinetics due to the contribution of LSC_{214}/LSC_{113} interface and significant difference in the rates of electrochemical reactions in heterostructure systems as compared with the corresponding bulk materials. For example, Crumlin *et al.*[342] revealed that an island structure of coating (LSC_{214} on LSC_{113}) with a developed interface increases the rate of electrode processes, a fact confirming the key role of the LSC_{214}/LSC_{113} interface in this effect.

VAN structures (Fig. 30 *a*,*b*) can also be organized at the interface between electrolyte $Ce_{0.9}Gd_{0.1}O_{1.95}$ (CGO) and cathode layer $La_{0.5}Sr_{0.5}CoO_3$ (LSCO); in this configuration, the effective three-phase boundary length and electrode reaction rate increase.[343] Thereafter, different theoretical models explaining the mechanisms of enhancement of oxygen reduction reaction kinetics at the LSC_{214}/LSC_{113} interface were developed.[346] The strained lattice state near this interface was simulated using the DFT method. The results obtained confirmed the enhancement of oxygen incorporation on the LSC_{214} surface, which is facilitated by the strained lattice state near the LSC_{214}/LSC_{113} interface. At the same time, there may be activation of oxygen diffusion along this interface with its subsequent incorporation into LSC_{113}. In correspondence with the simulation results, the joint effect of these two mechanisms may enhance oxygen reduction up to 400 times at a temperature of 500 °C. Stress also facilitates changes in the state of point defects, as well as the diffusion kinetics and redistribution of oxygen vacancies and dopants. Boundary effects include also diffusion of strontium cations from LSC_{113} to LSC_{214} and redistribution of lanthanum ions in these phases, which increases the concentration of oxygen vacancies and enhances oxygen incorporation. This mechanism is consistent with the DFT simulation results obtained by Gadre *et al.*[347]

In addition to the above-considered mechanisms of increasing the electrode reaction rate in heterogeneous VAN structures LSC_{214}/LSC_{113}, Chen *et al.*[348] indicated the activation of electronic conductivity of the LSC_{214} layer (contacting LSC_{113}), due to which the band gap in the energy diagram of LSC_{214} disappears at temperatures > 250 °C. It should be noted that the single-phase material LSC_{214} is characterized by a wide band gap (~1 eV) at the aforementioned temperatures. The increase in the electronic conductivity in combination with the enhancement of oxygen transport along the interface facilitate the reduction of oxygen adsorbed on the surface of nanocomposite electrode LSC_{214}/LSC_{113}. The authors suggested that this activation of electronic conductivity in LSC_{214} is due to the generation of electrons in the conduction band of LSC_{113} layer and their injection from LSC_{113} to LSC_{214} through the interface, which is also accompanied by the formation and subsequent migration of oxygen vacancies. In the case of VAN structure, this effect arises in the entire volume of columnar LSC_{214} cell with a length of 200 – 300 nm.

Despite the advantages of electrode VAN structures LSC_{214}/LSC_{113}, they were found to exhibit instability, enhanced ageing, and deterioration of characteristics at

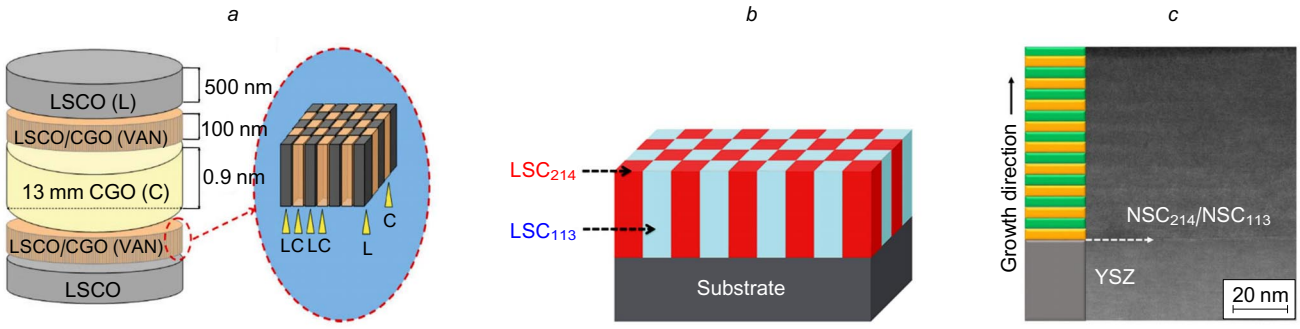


Figure 30. Schematics of (*a*) a symmetric cell with a VAN structure LSCO/CGO, located between electrode (LSCO) and electrolyte (CGO) layers;[343] (*b*) electrode VAN structure LSC_{214}/LSC_{113};[344] and (*c*) multilayer structure NSC_{113}/NSC_{214} on an YSZ substrate fabricated by PLD.[345] The figures were compiled by the authors based on the data of the aforementioned publications.

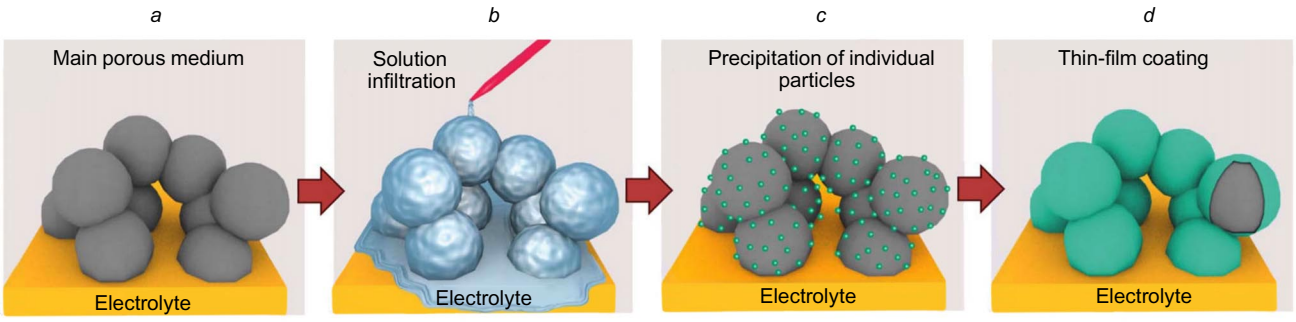


Figure 31. Schematic diagrams of the (*a*) structure of porous medium and processes of (*b*) solution infiltration into it with (*c*) deposition of individual particles and (*d*) formation of thin-film coating on the particles of porous material. The figure was compiled by the authors based on the data of Ref. 349.

temperatures >400 °C. Ma *et al.*[344] stated necessity of further search for materials based on which one would design efficient VAN structures stably operating at elevated temperatures.

Good prospects of the $Nd_{0.5}Sr_{0.5}CoO_{3-\delta}$/$Nd_{0.8}Sr_{1.2}CoO_{4\pm\delta}$ (NSC_{113}/NSC_{214}) heterostructure were announced by Zheng *et al.*,[345] who reported the results of studying the kinetics of oxygen exchange in this multilayer thin-film system, formed on a single-crystal YSZ substrate by pulsed laser deposition (Fig. 30 *c*). A significant increase in the oxygen surface exchange coefficient at 500 °C (up to 10^2-10^3 times) in comparison with single-phase NSC_{113} and NSC_{214} samples was obtained. Studies showed that the found enhancement of oxygen exchange kinetics is due to the processes of segregation of Sr^{2+} ions near the interface, where Nd^{3+} ions are replaced with Sr^{2+} ions; as a result, the activation energy of oxygen vacancy formation decreases.

Impregnation (or infiltration) of a porous material can be performed without using expensive equipment, due to which the heterostructure fabrication technology is significantly simplified. The characteristic features and application of infiltration in heterostructure fabrication technology were reviewed by Ding *et al.*[349] Impregnation is incorporation of a material into a porous medium using the solution or colloidal method (Fig. 31); the incorporated material is deposited on the inner pore surface, in contrast to the technologies of joint pressing and sintering of two powder materials.[350]

After the impregnation a heat treatment is performed at a relatively low temperature (300 – 500 °C), and the impregnation and heat treatment cycles are repeated. The output and long-term stability of SOFCs increases due to the infiltration of catalytically active species into the porous material of electrode. Kiebach *et al.*[351] noted that a necessary condition for implementing these composite electrodes is the absence of interaction between the embedded (impregnated) phase and the main porous medium, both during formation and under SOFC operation conditions. The morphology of composite electrode depends on the viscosity and wetting of its precursor. Various surfactants, as well as solutions of nitrates in different solvents and their mixtures,[352] are used to improve these characteristics. Vacuum and heating of porous substrate are applied to enhance infiltration.[353] The structures can be implemented in the following versions:

— impregnation of a material with oxygen ionic or mixed conductivity, such as SDC, GDC, and doped bismuth oxide, into the main porous material with electronic conductivity, for example, lanthanum – strontium manganites (LSM);[354, 355]

— impregnation of a material with electronic conductivity (in particular, LSM, LSCF) into a porous material with ionic or mixed conductivity, for example, GDC;[356]

— impregnation of catalytically active additives into the porous structure of electrode (single-phase or composite).

A drawback of impregnated composite electrodes is their temporal instability, caused by morphological and structural changes.[357] To eliminate the instability of impregnated electrode structures, Sındıraç *et al.*[358] proposed to apply composites based on nonaqueous LSCF – GDC precursors for infiltration into the porous GDC structure. The authors could form a continuous composite coating LSCF – GDC on GDC particles by multiple repetition of impregnation and heat treatment cycles (10 – 50 in total) at 700 °C and thus reduce the polarization resistance to 0.71 Ω cm^2. A subsequent analysis did not reveal any significant changes in the morphology and size of porous cathode particles after a long-term exposure at 700 °C; this was explained by the stabilizing effect of the composite shell on GDC particles, which impedes particle growth and agglomeration. One can also reduce the polarization resistance and increase the oxygen exchange rate by impregnating catalytically active particles of Pr_6O_{11},[359, 360] and MgO,[361, 362] and nanoparticles of barium carbonate[363] and calcium oxide.[364] Impregnation of CeO_2 nanoparticles is a well-known way to increase the catalytic activity of SOFC anodes. When studying the electrode kinetics of Ni – SDC20 anodes, Osinkin[365] showed that, by adding highly dispersed CeO_2, one can increase the anode activity by a factor of 10 – 24 due to the enhancement of surface processes (adsorption).

8. Modification of SOFC designs. Electrolyte-free and single-chamber cells

In the study by Riess[244] (published in 1992), it was suggested that a material with mixed conductivity can be used for both electrolyte and electrodes, with modification of the latter in the electrode conductivity region by doping. Currently, this approach is applied in electrolyte-free or single-layer SOFCs; the corresponding data were generalized in recent reviews, presented by Zhu's group.[366, 367] A schematic diagram of functioning of a single-layer SOFC is presented in Fig. 32.

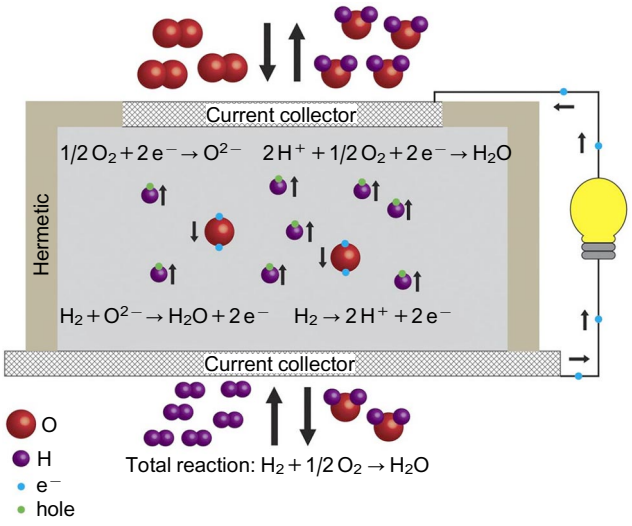


Figure 32. Schematic diagram of operation of a single-layer SOFC with a composite membrane, combining functions of anode, electrolyte, and cathode.[368] Published with permission of Elsevier.

The electrode reactions of hydrogen oxidation and oxygen reduction occur from the anode and cathode sides of the functional layer, in which transport of oxygen and hydrogen ions is implemented, with possible catalytic enhancement of electrochemical reactions under the action of current collector material.[368] The functional layer in these cells is a porous composite membrane, formed from a mixture of semiconductor and oxide particles with oxygen ionic or mixed conductivity. The role of semiconductor material is played by transition metal oxides, lithiated nickel oxide, or strontium titanate, which are mixed with ceria powder; for example, $LiNiO_2-GDC$,[369] $Ce_{0.8}Sm_{0.2}O_{2-\delta}-Li_{0.3}Ni_{0.6}Cu_{0.07}Sr_{0.03}O_{2-\delta}$,[370] and $SrTiO_3-CeO_2$.[371]

In correspondence with the fabrication technology of electrolyte-free or single-layer SOFCs, which were applied by Zhu's group,[369–371] a powder mixture can be formed by different methods. For example, an $LiNiO_2-GDC$ mixture was obtained[369] by co-precipitation, powders were annealed at a low temperature (~700 °C), and isostatic pressing was performed at a pressure of 250 MPa without subsequent high-temperature sintering. Then a current collector was deposited on both sides of the cell fabricated. Measurements on these cells were performed in a temperature range of 450–600 °C. Despite the absence of high-temperature annealing, the following parameters were obtained: OCV ≈ 1 V and power density of 0.45 W cm^{-2} at 550°C. For a single-layer SOFC with a composite membrane $SrTiO_3-CeO_2$ and current collectors-$LiNi_{0.8}Co_{0.15}Al_{0.05}O_2$ (NCAL), the OCV and specific power density at the same temperature were, respectively, 1.1. V and 0.75 W cm^{-2} (Ref. 371).

Different mechanisms were proposeds[366, 367] to explain the effect of blocking the electron current through a single-layer SOFC, for example, because of the occurrence of n- and p-type conductivities from the sides of fuel and oxidant supply, respectively. This mechanism is responsible for the occurrence of a depleted p–n junction and blocking of electron current through the cell. An example is the study by Wang *et al.*,[372] who proposed to use undoped CeO_2 (with dominant electronic conductivity) in a single-layer SOFC. As a result, they obtained a nanocomposite material with a core/shell ($CeO_{2-\delta}/CeO_2$) structure (Fig. 33 *a*,*b*) having ionic conductivity of ~0.1 S cm^{-1} at 550 °C; its application as an electrolytic membrane (200 μm) provided power 660 mW cm^{-2} at 550 °C (Fig. 33 *c*) and OCV equal to 1.12 V for an SOFC with symmetric NCAL electrodes. Surface doping of nanoscale CeO_2 (aimed at forming a core/shell composite) was carried out by 2-h treatment in hydrogen at 550 °C. The presence of Ce^{3+} in the near-surface layer several nanometers thick was confirmed by different methods. The principle of blocking electronic conductivity in the nanocomposite membrane due to the formation of a p–n junction between CeO_2 and reduced $CeO_{2-\delta}$, which have electronic conductivities of p and n types, respectively, is illustrated in Fig. 33 *d*. The enhancement of ionic conductivity was related to the formation of interface channels with elevated concentration of oxygen vacancies.

Modelling of single-layer SOFC operation, with consideration of the gas permittivity of composite porous membrane from the sides of fuel and oxidant, and comparison of calculation results with experimental data were performed.[373] The authors reported the results of calculating

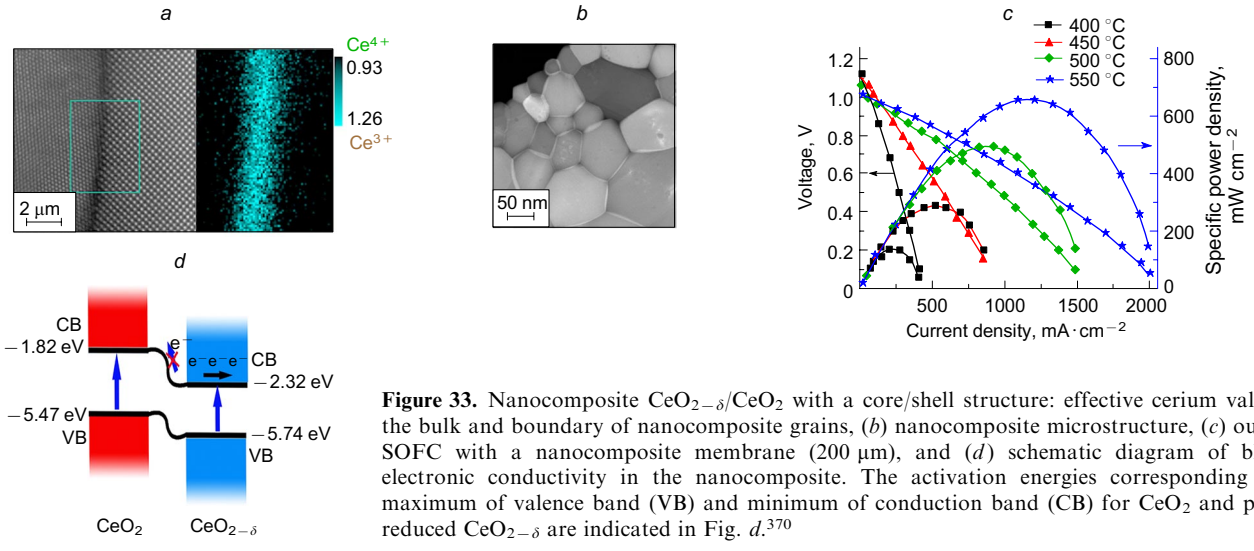


Figure 33. Nanocomposite $CeO_{2-\delta}/CeO_2$ with a core/shell structure: effective cerium valence in the bulk and boundary of nanocomposite grains, (*b*) nanocomposite microstructure, (*c*) output of SOFC with a nanocomposite membrane (200 μm), and (*d*) schematic diagram of blocking electronic conductivity in the nanocomposite. The activation energies corresponding to the maximum of valence band (VB) and minimum of conduction band (CB) for CeO_2 and partially reduced $CeO_{2-\delta}$ are indicated in Fig. *d*.[370]

the oxygen and hydrogen permittivities from the corresponding sides of porous membrane (at a pressure of 1 atm). It was found that the gas penetration depth did not exceed 14 μm at a membrane porosity of 0.5 and a current density through the cell of 100 – 2000 mA cm^{-2}; *i.e.*, it was much smaller than the membrane thickness (0.5 mm).

Zhu *et al.*[374] also paid attention to the porosity of composite membrane, which seems to play a rather important role in the single-layer SOFC operation. It was found that pressing of a composite membrane at a pressure of 250 MPa may change its porosity at an elevated temperature; specifically, the porosity decreases from 30.94 ± 0.088 to 29.35 ± 0.068% upon heating at 600 °C for 0.5 h. To increase the SOFC efficiency, the authors proposed to use a membrane with a porosity gradient, in particular, with a dense central part. A possibility of applying a composite membrane consisting of a mixture of powders of protonic conductor $BaCe_{0.6}Zr_{0.2}Y_{0.2}O_{3-\delta}$ (BCZY622) and $Li_2O-NiO-ZnO$ (LNZn) oxides was investigated;[375] this membrane was subjected to isostatic pressing with subsequent sintering at 1200 °C. Dense membranes 1.11 mm thick were prepared. Current collectors were formed by depositing and sintering a silver paste. For this cell, the OCV was 0.83 V and the maximum specific power density was 3.86 mW cm^{-2} at 600 °C. The authors explained the low value of maximum specific power density by the dense microstructure of the sintered membrane BCZY622 – LNZn, in contrast to the porous membranes applied by Zhu *et al.*[374] The polarization loss (~100 Ω cm^2 at 600 °C) turned out to be about two orders of magnitude larger than the ohmic loss. Thus, the active region of electrochemical reactions at the membrane/gas interface decreased because of the dense membrane microstructure. One can suggest that the increase in the active region of electrochemical reactions in a single-layer SOFC is due to the porous structure of composite ceramic membrane, in which the inner surface of the porous space of a significant part of bulk is involved, which leads to an increase in the SOFC output. One does not need to use a gas-tight electrolyte for a single-layer SOFC and some mixing of fuel and oxidant is allowed; thus, the requirement to isolation of fuel and oxidant gas channels are less stringent. This requirement is rather difficult to fulfill, especially under conditions of long-term and nonstationary SOFC operation. Solid oxide fuel cells with porous electrolyte can be considered as a catalytic membrane reactor.[376]

The problem of gas channel isolation is absent in the case of single-chamber SOFCs, where a cell (Fig. 34) is placed in a mixture of fuel and oxidant.[377] The advantages of single-chamber SOFCs are as follows: no need for making cells gas-tight, possibility of miniaturizing the device, a simpler design of the cell and gas supply system in comparison with a two-chamber SOFC, and a possibility of increasing cell temperature due to the exothermic reaction between the fuel and oxidant. Their drawbacks are lower efficiency, need for applying catalytically active materials, less fuel utilization, and a risk of fuel – oxidant mixture explosion.

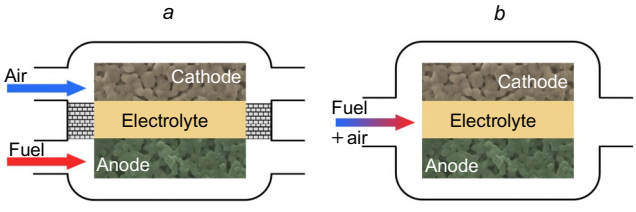


Figure 34. Schematic diagrams of (*a*) two-chamber and (*b*) single-chamber SOFCs.[377]

Hibino *et al.*[378] reported that a specific power density of 644 mW cm^{-2} was achieved on a single-chamber solid-oxide fuel cell PdO + NiO – SDC (anode)/SDC (electrolyte)/$Sm_{0.5}Sr_{0.5}CoO_3$ (cathode). The electrodes were deposited on a carrier SDC electrolyte substrate 0.5 mm thick. A rather large OCV was obtained: OCV ≈ 0.9 V. The highest specific power density was reached at a methane : oxygen volume ratio equal to 1 : 1; the large OCV indicates the absence of any significant electron current causing internal short circuit. An important role is played by the PdO additive (1 wt.%) in the anode composition; without this additive the OCV does not exceed 0.11 V, which indicates the catalytic activity of palladium oxide with respect to the reactions of partial methane oxidation on the anode and generation of H_2O and CO_2

$$CH_4 + 1/2\,O_2 \longrightarrow 2\,H_2 + CO \quad (35)$$

$$H_2 + O^{2-} \longrightarrow H_2O + 2e^- \quad (36)$$

$$CO + O^{2-} \longrightarrow CO_2 + 2e^- \quad (37)$$

Apparently, the influence of the exothermic character of anode reactions, whose thermal effect increases the cell temperature, on the single-chamber SOFC output is decisive. It was found by Shao *et al.*[379] that the temperature measured directly on the cell exceeds the temperature of the gas mixture in the heating chamber; the difference was as large as 150 °C. With an increase in the gas mixture temperature to 585 °C the difference between the cell and gas mixture temperatures increased (due to thermal effect of oxidation reaction). The authors investigated SOFCs with a thin-film SDC electrolyte on a carrier anode Ni – SDC with a composite cathode $Ba_{0.5}Sr_{0.5}Co_{0.8}Fe_{0.2}O_{3-\delta}$/SDC. The maximum power density was obtained with a $CH_4 + O_2 + He$ mixture at a temperature of 650 °C (corresponding to a cell temperature of ~790 °C): 760 mW cm^{-2}.

The operation of a single-chamber SOFC is based on the difference in the catalytic activity and selectivity of cathode and anode materials with respect to the electrochemical reactions occurring in them.[380] Riess[381,382] considered the theoretical aspects of operation of a single-chamber SOFC and an SOFC with a porous electrolyte in a fuel – oxidant mixture. The application of a porous electrolyte in a two-chamber fuel cell allows one to solve the problem of igniting fuel due to its controlled mixing with oxidant. A working version of this SOFC was reported.[383] The maximum power density obtained on a cell with a porous GDC electrolyte and a methane – oxygen mixture was rather low: 16 mW cm^{-2} (700 °C).

The problem of increasing the performance of single-chamber SOFCs and SOFCs with a porous electrolyte can be solved by increasing the selectivity of cathode and anode, modifying their microstructure, and optimizing the working regimes in order to provide maximum catalytic activity and efficiency of electrochemical energy conversion. In this case, modification can be performed applying all the aforementioned heterostructure fabrication methods, including the simplest one: electrode impregnation, whose effect is also pronounced in the case of single-chamber cells.[384]

9. Conclusion

Currently, the basic line of research in the development of medium- and low-temperature SOFCs is the search for ways to increase their operation efficiency and reduce the cost of generated energy. The tendency for the ceramic-MIEC cells is the same. Materials based on CeO_2 are considered among the most promising for SOFCs of this type due to their high ionic conductivity, thermodynamic stability in a wide range of temperatures and partial oxygen pressures, and tolerance of fluorite lattice to doping with different-valence elements to high concentrations.

Despite the high ionic conductivity of ceria-based materials, there are a number of fundamental problems impeding commercial production of MIEC SOFCs. Hence, the approaches implemented must be analyzed with estimation of their prospects and possibility of commissioning solutions obtained. The key problems determining the SOFC working efficiency are as follows (in the order of their importance):

— occurrence of electronic conductivity in materials based on CeO_2 electrolytes in a reducing atmosphere at high temperatures, which gives rise to leakage currents and reduces the SOFC output (one of possible solutions of this problem is to develop cells operating in medium- and low-temperature ranges);

— decrease in the electrolyte conductivity at low temperatures (< 600 °C) and high dopant concentrations as a result of the formation of local ordered structures due to the association of vacancies and dopant cations;

— significant influence of the microstructure of electrolyte on its conductivity, because grain boundaries form a barrier for ion transport even in materials with a very low impurity content; there are also problems with fabrication of gas-tight ceramics because of high sintering temperatures;

— difficulties with the use of nanomaterials based on CeO_2, which are related to the occurrence of electronic conductivity in air in the nanoscale state;

— implementation of thin-film technologies calls for thermodynamic and thermomechanical stability of thin electrolyte film in a multilayer solid structure during SOFC operation;

— necessity of searching for new materials for electrodes and optimizing their structure for successful operation in MIEC-electrolyte SOFCs at low temperatures (in this context, the advantage of CeO_2 electrolytes over conventional electrolytes based on ZrO_2 is the absence of chemical reactions with many known perovskite materials).

Different research teams propose the following ways to solve the aforementioned problems: to perform structural modification of electrolyte by fitting dopants according to different criteria in order to increase the ionic conductivity and expand the electrolytic domain and to design new composite materials. The best result was obtained by fitting dopants or combining dopants with minimum effective cation – vacancy binding energy in order to supress the formation of local ordered regions in fluorite structure. Good performance characteristics were reached for SOFCs with composite membranes characterized by a high level of both bulk and interface conductivity. Specific power densities in the range of 1 – 1.7 W cm^{-2} were observed for membranes with thicknesses from 120 to 900 μm. According to the estimates,[305] the development of appropriate methods for fabricating thin-film composite membranes will make it possible to increase the specific power density of SOFCs with these membranes to 2.5 W cm^{-2} at 550 °C.

The development of reproducible fabrication technologies for thin-film structures is of crucial importance for achieving high output and stability of SOFCs with multilayer structures, in which electron current is blocked by depositing barrier layers from the cathode or anode side. Currently, anode coatings are considered to be the most efficient. The range of coating materials is constantly expanded; both oxygen ionic and protonic conductors are applied. Techniques of thin film deposition are modified as well: from simple ceramic and colloidal methods to various laser- and plasma-based technologies. Methods for fabricating horizontally and vertically aligned heterostructures are also promising. However, the problem of their stability during long-term cell operation remains open.

During the last decade particular attention has been paid to designs of electrolyte-free cells. The operation of a single-layer SOFC is based on the occurrence of n- and p-type conductivities in a membrane from the sides of fuel and oxidant supply, respectively, which leads to the formation of a depleted p – n junction and blocking of electron current through the cell. The functioning of developed designs of single-chamber SOFCs is based on the difference in the catalytic activity and selectivity of cathode and anode materials with respect to the electrochemical reactions occurring in them. Note that the output of single-chamber SOFCs and SOFCs with porous electrolyte may be increased by modifying their microstructure and optimizing their working regimes in order to obtain maximum catalytic activity and electrochemical energy conversion efficiency. Modification can be performed using all above-described heterostructure fabrication methods, including the simplest one: impregnation of electrode materials.

Mathematical simulation of devices with a ceramic membrane (having mixed conductivity), aimed at finding the most effective structure and design of SOFC, is also of great importance. It was shown that one of the most efficient ways to block the internal short circuit in the electrolyte layer (caused by the occurrence of electronic conductivity in a reducing atmosphere) is to form thin barrier layers from the anode side; in this case one must ensure minimum electronic conductivity of the blocking layer and sufficiently high ionic and electronic conductivity of the layer with mixed conductivity. It is also important to develop further theoretical models and numerical simulation methods to describe the electrochemical reactions occurring in the SOFC solid structure and the corresponding processes of heat- and mass exchange in the porous space of electrodes and gas-supplying channels using computational hydrodynamics, kinetic theory, and lattice Boltzmann equations.

The review was supported by the Russian Foundation for Basic Research (Project 20-03-00151).

We are grateful to N.S.Pikalova (IHTE UB RAS) for the preparing graphical material.

10. List of acronyms and designations

Acronyms:

AFL — anode functional layer;

ALS — Adler – Lane – Steel model;

ASR — area specific resistance;

BCS — samarium-doped barium cerate: $BaCe_{0.8}Sm_{0.2}O_{3-\delta}$;

BLM — brick-layer model;
BZCY — yttrium-doped barium cerate – zirconate, $BaZr_{0.1}Ce_{0.7}Y_{0.2}O_{3-\delta}$;
DFT — density functional theory;
EC — ethyl cellulose;
EDC20 — erbium doped ceria $Ce_{0.8}Er_{0.2}O_{2-\delta}$;
EPD — electrophoretic deposition;
EXAFS — extended X-ray absorption fine structure;
FC — fuel cell;
GDC — ceria doped with gadolinium to different levels, $Ce_{0.9}Gd_{0.1}O_{1.95}$ (GDC10), $Ce_{0.8}Gd_{0.2}O_{1.9}$ (GDC20);
KC — potassium carbonate K_2CO_3;
LC — lithium carbonate Li_2CO_3;
LCN — calcium-doped lanthanum niobate, $La_{0.995}Ca_{0.005}NbO_4$;
LNC x/y — binary salt of lithium – sodium carbonate $Li_2CO_3 - Na_2CO_3$, where x and y are mole fractions of components;
LNCS — monoxide NiO, doped with lithium, copper, and strontium cations, $Li_{0.3}Ni_{0.6}Cu_{0.07}Sr_{0.03}O_{2-\delta}$;
LSC_{113} — lanthanum – strontium cobaltite, $La_{1-x}Sr_xCoO_{3-\delta}$;
LSC_{214} — layered lanthanum – strontium cobaltite, $La_{2-x}Sr_xCoO_{4-\delta}$;
LSCF — lanthanum – strontium cobaltite ferrite, $La_{0.6}Sr_{0.4}Co_{0.2}Fe_{0.8}O_{3-\delta}$;
LSCO — lanthanum – strontium cobaltite, $La_{0.5}Sr_{0.5}CoO_{3-\delta}$;
LSM — lanthanum – strontium manganites with different contents of lanthanum and strontium: $La_{0.85}Sr_{0.15}MnO_{3-\delta}$, $La_{0.6}Sr_{0.4}MnO_{3-\delta}$, $La_{0.8}Sr_{0.2}MnO_{3-\delta}$;
MIEC — mixed ionic – electronic conductor;
NC — sodium carbonate, Na_2CO_3;
NCAL — aluminium-doped lithiated nickelate cobaltite, $Ni_{0.8}Co_{0.15}Al_{0.05}LiO_{2-\delta}$;
NLKC $x/y/z$ — ternary salt of sodium – lithium – potassium carbonate, $Na_2CO_3 - Li_2CO_3 - K_2CO_3$, where x, y, z are mole factions of components;
N_{max} — maximum attainable specific power density (at the theoretical Nernst voltage);
NN — near neighbor interactions;
NNN — next near neighbor interactions;
NSC_{113} — neodymium – strontium cobaltite, $Nd_{0.5}Sr_{0.5}CoO_{3-\delta}$;
NSC_{214} — layered neodymium – strontium cobaltite, $Nd_{0.8}Sr_{1.2}CoO_{4\pm\delta}$;
OCV — open circuit value;
PLD — pulsed laser deposition;
PVA — polyvinyl alcohol;
SDC — samarium-doped ceria, $Ce_{0.8}Sm_{0.2}O_{1.9}$ (SDC20);
SOFC — solid-oxide fuel cell;
SSZ — zirconia stabilized with scandium oxide, $Zr_{0.9}Sc_{0.1}O_{1.9}$;
STO — strontium titanate, $SrTiO_3$;
TEM — transmission electron microscopy;
VAN — vertically aligned nanocomposite;
XANES — X-ray absorption near edge structure;
XPS — X-ray photoelectron spectroscopy;
XRD — X-ray diffraction analysis;
YSZ — zirconia stabilized with yttrium oxide, $(ZrO_2)_{0.92}(Y_2O_3)_{0.08}$.

Designations:
a — unit cell parameter;
a_0 — CeO_2 lattice constant;
Δa — change in the lattice parameter caused by doping;
$[Ce'_{Ce}]$ — concentration of small-radius polarons localized on cerium ions;
C_g, C_{gb} — capacitances of the grain bulk and grain boundaries of polycrystalline samples;
c_1 — dimer concentration;
c_2 — trimer concentration;
c_{el} — electron concentration;
c_v — oxygen vacancy concentration;
e — elementary charge;
E_a — conductivity activation energy;
E_H — activation energy of small-polaron hop;
E_{th} — voltage according to the Nernst formula;
i — ion current density;
ΔH_a — formation enthalpy of vacancy – cation associates;
ΔH_m — oxygen vacancy migration enthalpy;
ΔH_r — cerium reduction reaction enthalpy;
k — Boltzmann constant;
K_r — cerium reduction reaction constant;
M'_{Ce} — concentration of metal ions in cerium site with an effective charge of -1;
p_{O_2} — partial oxygen pressure ;
$p^*_{O_2}$ — critical partial oxygen pressure (at which $\sigma_{ion} = \sigma_{el}$);
R — universal gas constant;
R_{el}, R_{ion} — resistances to, respectively, electron and ion currents in electrolyte;
R_Z — polarization resistance;
R_g, R_{gb} — grain bulk and grain boundary resistances of polycrystalline samples;
r_c — dopant critical radius;
r_d — dopant radius;
r_p — average pore size;
ΔS_m — change in entropy caused by oxygen vacancy transport;
ΔS_r — cerium reduction reaction entropy;
T — absolute temperature;
T_c — critical temperature;
T_{melt} — carbonate melting temperature;
T_{trans} — superionic transition temperature;
$[V_O^{\cdot\cdot}]$ — oxygen vacancy concentration in the Kroger – Vink notation;
W — elastic lattice strain;
δ — oxygen vacancy level;
δ_{gb} — grain boundary width;
μ_{el} — electron mobility;
μ_{O_2} — oxygen chemical potential;
$\mu^\circ_{O_2}$ — standard value of oxygen chemical potential;
σ_{ion}, σ_{el} — ionic and electronic conductivities;
σ_{tot}, σ_g, σ_{gb} — total, grain bulk, and grain boundary conductivities, respectively;
λ — Debye length;
ω — frequency.

References

1. N.Jaiswal, K.Tanwar, R.Suman, D.Kumar, S.Upadhyay, O.Parkash. *J. Alloys Compd.*, **781**, 984 (2019)
2. *Tverdooksidnye Toplivnye Elementy: Problemy, Puti Resheniya, Perspektivy Razvitiya i Kommertsializatsii. Analiticheskii Obzor. (Solid Oxide Fuel Cells: Problems, Solutions, Development and Commercialization Prospects.*

Analytical Review). (SRI FRCEC 'Scientific Research Institute — Federal Research Centre for Projects Evaluation and Consulting Services'; 2015); https://www.extech.ru/files/anr_2015/anr_8.pdf (last access 27.05.2021)
3. I.Sreedhar, B.Agarwal, P.Goyal, S.A.Singh. *J. Electroanal. Chem.*, **848**, 113315 (2019)
4. A.M.Abdalla, S.Hossain, P.M.Petra, M.Ghasemi, A.K.Azad. *Front. Energy*, **14**, 359 (2020)
5. K.Kendall, M.Kendall. *High-Temperature Solid Oxide Fuel Cells for the 21st Century*. (2nd Edn). (Amsterdam: Elsevier, 2015)
6. A.Choudhury, H.Chandra, A.Arora. *Renew. Sustain. Energy Rev.*, **20**, 430 (2013)
7. U.Damo, M.Ferrari, A.Turan, A.Massardo. *Energy*, **168**, 235 (2019)
8. S.Y.Gómez, D.Hotza. *Renew. Sustain. Energy Rev.*, **61**, 155 (2016)
9. D.A.Osinkin, N.M.Bogdanovich, S.M.Beresnev, E.Yu.Pikalova, D.I.Bronin, Yu.P.Zaikov. *Russ. J. Electrochem.*, **54**, 644 (2018)
10. N.Danilov, J.Lyagaeva, G.Vdovin, D.Medvedev. *Appl. Energy*, **237**, 924 (2019)
11. N.Danilov, J.Lyagaeva, G.Vdovin, E.Pikalova, D.Medvedev. *Energy Convers. Manag.*, **172**, 129 (2018)
12. A.V.Kasyanova, L.R.Tarutina, A.O.Rudenko, J.G.Lyagaeva, D.A.Medvedev. *Russ. Chem. Rev.*, **89**, 667 (2020)
13. F.Ramadhani, M.A.Hussain, H.Mokhlis, S.Hajimolana. *Renew. Sustain. Energy Rev.*, **76**, 460 (2017)
14. J.Savioli, G.W.Watson. *Curr. Opin. Electrochem.*, **21**, 14 (2020)
15. *Modeling Solid Oxide Fuel Cells. Methods, Procedures and Techniques*. (Eds R.Bove, S.Ubertini). (Springer, Netherlands, 2008)
16. D.A.Osinkin, N.M.Bogdanovich, A.L.Gavrilyuk. *Electrochim. Acta*, **199**, 108 (2016)
17. A.V.Khrustov, D.S.Pavlov, M.V.Ananyev. *Solid State Ionics*, **346**, 115202 (2020)
18. Y.Ling, X.Wang, Z.Ma, K.Wei, Y.Wu, M.Khan, K.Zheng, S.Shen, S.Wang. *J. Mater. Sci.*, **55**, 1 (2020)
19. Z.Gao, L.V.Mogni, E.C.Miller, J.G.Railsback, S.A.Barnett. *Energy Environ. Sci.*, **9**, 1602 (2016)
20. B Singh, S.Ghosh, S.Aich, B.Roy. *J. Power Sources*, **339**, 103 (2017)
21. E.Yu.Pikalova, V.G.Bamburov, A.A.Murashkina, A.D.Neuimin, A.K.Demin, S.V.Plaksin. *Russ. J. Electrochem.*, **47**, 690 (2011)
22. N.Danilov, E.Pikalova, J.Lyagaeva, B.Antonov, D.Medvedev, A.Demin, P.Tsiakaras. *J. Power Sources*, **366**, 161 (2017)
23. S.Ya.Istomin, E.V.Antipov. *Chem. Rev.*, **82**, 686 (2013)
24. V.A.Sadykov, E.M.Sadovskaya, N.F.Eremeev, P.I.Skriabin, A.V.Krasnov, Yu.N.Bespalko, S.N.Pavlova, Yu.E.Fedorova, E.Yu.Pikalova, A.V.Shlyakhtina. *Russ. J. Electrochem.*, **55**, 701 (2019)
25. S.N.Marshenya, B.V.Politov, D.A. Osinkin, A.Yu.Suntsov, I.A.Leonidov, V.L.Kozhevnikov. *J. Alloys Compd.*, **779**, 712 (2019)
26. E.Pikalova, A.Kolchugin, M.Koroleva, A.Farlenkov, D.Medvedev. *J. Power Sources*, **438**, 226998 (2019)
27. N.A.Danilov, A.P.Tarutin, J.G.Lyagaeva, E.Yu.Pikalova, A.A.Murashkina, D.A.Medvedev, M.V.Patreleev, A.K.Demin. *Ceram. Int.*, **43**, 15418 (2017)
28. D.A.Osinkin, V.D.Zhuravlev. *Russ. J. Appl. Chem.*, **93**, 299 (2020)
29. D.A. Osinkin, N.I.Lobachevskaya, A.Yu.Suntsov. *J. Alloys Compd.*, **708**, 451 (2017)
30. O.A.Petrii. *Russ. Chem. Rev.*, **84**, 159 (2015)
31. Yu.D.Tretyakov, E.A.Goodilin. *Russ. Chem. Rev.*, **78**, 801 (2009)
32. A.A.Kurteeva, S.M.Beresnev, D.A.Osinkin, B.L.Kuzin, G.K.Vdovin, V.D.Zhuravlev, N.M.Bogdanovich, D.I.Bronin, A.A.Pankratov, I.Yu.Yaroslavtsev. *Russ. J. Electrochem.*, **47**, 1381 (2011)
33. O.V.Tiunova, T.A.Khabas, S.I.Bredikhin, I.E.Kuritsyna. *Inorg. Mater. Appl. Res.*, **7**, 278 (2016)
34. E.A.Agarkova, D.A.Agarkov, I.N.Burmistrov, O.Yu.Zadoroznaya, D.V.Yalovenko, Yu.K.Nepochatov, S.I.Bredikhin. *Russ. J. Electrochem.*, **56**, 132 (2020)
35. D.A.Osinkin, N.M.Bogdanovich, S.M.Beresnev, V.D.Zhuravlev. *J. Power Sources*, **288**, 20 (2015)
36. N.S.Sochugov, A.A.Soloviev, A.V.Shiplova, S.V.Rabotkin, V.P.Rotshtein. *Solid State Ionics*, **231**, 11 (2013)
37. I.S.Erilin, D.A.Agarkov, I.N.Burmistrov, V.E.Pukha, D.V.Yalovenko, N.V.Lyskov, M.N.Levin, S.I.Bredikhin. *Mater. Lett.*, **266**, 127439 (2020)
38. S.K.Schubert, M.Kusnezoff, À.Miåhaelis, S.I.Bredikhin. *J. Power Sources*, **217**, 364 (2012)
39. A.V.Kuzmin, Yu.V.Novikova, A.Yu.Stroeva, V.P.Gorelov, A.I.Vylkov, M.A.Ananyev, A.V.Ermakov, Yu.P.Zaikov. *Russ. J. Appl. Chem.*, **91**, 196 (2018)
40. A.V.Nikonov, A.V.Spirin, A.S.Lipilin, V.R.Khrustov, S.N.Paranin. *Russ. J. Electrochem.*, **54**, 547 (2018)
41. A.A.Solov'ev, A.V.Shipilova, A.N.Koval'chuk, I.V.Ionov, S.V.Rabotkin. *Russ. J. Electrochem.*, **52**, 662 (2016)
42. D.A.Agarkov, M.A.Borik, V.T.Bublik, A.S.Chislov, A.V.Kulebyakin, I.E.Kuritsyna, V.A.Kolotygina, E.E.Lomonova, F.O.Milovich, V.A.Myzina, V.V.Osiko, N.Yu.Tabachkova. *J. Alloys Compd.*, **791**, 445 (2019)
43. V.V.Kharton, A.A.Yaremchenko, E.N.Naumovich, F.M.B.Marques. *J. Solid State Electrochem.*, **4**, 243 (2000)
44. M.Mogensen, N.M.Sammes, G.A.Tompsett. *Solid State Ionics*, **129**, 63 (2000)
45. M.Melchionna, P.Fornaseiro. *Mater. Today*, **17**, 349 (2014)
46. S.Anirban, A.Dutta. *Int. J. Hydrogen Energy*, **43**, 23418 (2018)
47. R.Schmitt, A.Nenning, O.Kraynis, R.Korobko, A.I.Frenkel, I.Lubomirsky, S.M.Haile. *Chem. Soc. Rev.*, **49**, 554 (2020)
48. J.L.F.Da Silva, M.V.Ganduglia-Pirovano, J.Sauer, V.Bayer, G.Kresse. *Phys. Rev. B*, **75**, 045121 (2007)
49. R.T.Dirstine, R.N.Blumental, T.F.Kuech. *J. Electrochem. Soc.*, **126**, 264 (1979)
50. A.F.Wells. *Structural Inorganic Chemistry*. (3rd Edn.). (Oxford University Press,Clarendon Press, 1962)
51. A.I.Leonov. *Vysokotemperaturnaya Khimiya Khislorodnykh Soedinenii Tseziya. (High Temperature Chemistry of Oxygen Compounds of Cerium)*. (Leningrad: Nauka, 1969)
52. Yu.A.Baykov, T.Klaeson, D.Aerts. *Phys. Solid State*, **40**, 205 (1998)
53. K.L.Duncan, Y.Wang, S.R.Bishop, F.Ebrahimi, E.D.Wachsman. *J. Appl. Phys.*, **101**, 044906 (2007)
54. H.L.Tuller, A.S.Nowik. *J. Electrochem. Soc.*, **126**, 209 (1979)
55. C.W.M.Castleton, J.Kullgren, K.Hermansson. *J. Chem. Phys.*, **127**, 11 (2007)
56. W.C.Chueh, A.H.McDaniel, M.E.Grass, Y.Hao, N.Jabeen, Z.Liu, S.M.Haile, K.F.McCarty, H.Bluhm, F.El.Gabaly. *Chem. Mater.*, **24**, 1876 (2012)
57. Y.Xiong, H.Kishimoto, K.Yamaji, M.Yoshinaga, T.Horita, M.E.Brito, H.Yokokawa. *Electrochem. Solid State Lett.*, **13**, B21 (2010)
58. D.-J.Kim. *J. Am. Ceram. Soc.*, **72**, 1415 (1989)
59. S.J.Hong, A.V.Virkar. *J. Am. Ceram. Soc.*, **78**, 433 (1995)
60. G.Brauer, H.Gradinger. *Z. Anorg. Allg. Chem.*, **276**, 209 (1954)
61. M.Coduri, S.Checchia, M.Longhi, D.Ceresoli, M.Scavani. *Front. Chem.*, **6**, 526 (2018)
62. A.Kossoy, Q.Wang, R.Korobko, V.Grover, Y.Feldman, E.Wachtel, A.K.Tyagi, A.I.Frenkel, I.Lubomirsky. *Phys. Rev. B*, **87**, 054101 (2013)
63. F.Ye, T.Mori, D.R.Ou, J.Zou, G.Auchterlonie, J.Drennan. *Solid State Ionics*, **179**, 827 (2008)

64. O.Kraynis, J.Timoshenko, J.Huang, H.Singh, E.Wachtel, A.I.Frenkel, I.Lubomirsky. *Inorg. Chem.*, **58**, 7527 (2019)
65. C.Artini, M.M.Carnasciali, G.A.Costa, J.R.Plaisier, M.Pani. *Solid State Ionics*, **311**, 90 (2017)
66. W.B.White. *J. Chem. Phys.*, **59**, 1561 (1973)
67. R.Schmitt, J.Spring, R.Korobko, J.L.M.Rupp. *ACS Nano*, **11**, 8881 (2017)
68. D.A.Agarkov, I.N.Burmistrov, G.M.Eliseev, I.V.Ionov, S.V.Rabotkin, V.A.Semenov, A.A.Solovyev, I.I.Tartakovskii, S.I.Bredikhin. *Solid State Ionics*, **344**, 115091 (2020)
69. H.Yahiro, T.Ohuchi, K.Eguchi, H.Arai. *J. Mater. Sci.*, **23**, 1036 (1988)
70. V.Tangadurai, P.Kopp. *J. Power Sources*, **168**, 178 (2007)
71. J.M.S.Júnior, L.F.B.Malta, F.M.S.Garrido, T.Ogasawara, M.E.Medeiros. *Mater. Chem. Phys.*, **135**, 957 (2012)
72. K.S.Anjaneya, G.P.Nayaka, J.Manjanna, V.M.Ashwin Kumar, G.Govindaraj, K.N.Ganesha. *J. Alloys Compd.*, **598**, 33 (2014)
73. C.E.Milliken, S.Guruswamy, A.C.Khandkar. *J. Am. Ceram. Soc.*, **84**, 1533 (2001)
74. S.I.Ahmad, T.Mohammed, A.Bahafi, M.B.Suresh. *Appl. Nanosci.*, **7**, 243 (2017)
75. R.Chockalingam, V.R.W.Amarakoon, H.Giesche. *J. Eur. Ceram. Soc.*, **28**, 959 (2008)
76. E.Yu.Pikalova, V.I.Maragou, A.K.Demin, A.A.Murashkina, P.E.Tsiakaras. *Solid State Ionics*, **179**, 1557 (2008)
77. T.Zhang, Z.Zeng, H.Huang, P.Hing, J.Kilner. *Mater. Lett.*, **57**, 124 (2002)
78. C.Kleinlogel, L.J.Gauckler. *J. Electroceram.*, **5**, 231 (2000)
79. D.P.Fagg, V.V.Kharton, J.R.Frade. *J. Electroceram.*, **9**, 199 (2002)
80. L.A.Villas-Boas, F.M.L.Figueiredo, D.P.F.de Sauza, F.M.B.Marques. *Solid State Ionics*, **262**, 522 (2014)
81. V.Gil, J.Tataj, C.Moure, P.Duran. *J. Eur. Ceram. Soc.*, **27**, 801 (2007)
82. A.S.Bagishev, D.V.Maslennikov, M.P.Popov, A.P.Nemudry. *Mater. Today: Proc.*, **25**, 464 (2020)
83. T.S.Zhang, J.Ma, Y.J.Leng, S.H.Chan, P.Hing, J.A.Kilner. *Solid State Ionics*, **168**, 187 (2004)
84. V.V.Kharton, E.N.Naumovich, A.A.Vecher. *J. Solid State Electrochem.*, **3**, 61 (1999)
85. B.C.H.Steele, K.M.Hori, S.Uchino. *Solid State Ionics*, **135**, 445 (2000)
86. V.V.Kharton, A.P.Viskup, F.M.Figueiredo, E.N.Naumovich, A.L.Shaulo, F.M.B.Marques. *Mater. Lett.*, **53**, 160 (2002)
87. G.-B.Jung, T.-J.Huang, C.-L.Chang. *J. Solid State Electrochem.*, **6**, 225 (2002)
88. J.Faber, C.Geoffroy, A.Roux, A.Sylvestre, P.Abelard. *Appl. Phys. A: Sci. Process.*, **49**, 225 (1989)
89. L.Minervini, M.O.Zacate, R.W.Grimes. *Solid State Ionics*, **116**, 339 (1999)
90. V.Butler, C.R.A.Catlow, B.E.F.Fender, J.H.Harding. *Solid State Ionics*, **8**, 109 (1983)
91. D.A.Andersson, S.I.Simak, N.V.Skorodumova, I.A.Abrikosov, B.Johansson. *Proc. Natl. Acad. Sci. USA*, **103**, 3518 (2006)
92. J.van Herle, D.Seneviratne, A.J.McEvoy. *J. Eur. Ceram. Soc.*, **19**, 837 (1999)
93. N.J.Kidner, Z.J.Homrighaus, B.J.Ingram, T.O.Mason, E.J.Garboczi. *J. Electroceram.*, **14**, 283 (2005)
94. M.J.Verkerk, B.J.Middlehuis, A.J.Burggraaf. *Solid State Ionics*, **6**, 159 (1982)
95. H.Näfe. *Solid State Ionics*, **13**, 255 (1984).
96. S.Kim, J.Maier. *J. Electrochem. Soc.*, **149**, J73 (2002)
97. N.N.Novik, V.G.Konakov, I.Yu.Archakov. *Rev. Adv. Mater. Sci.*, **40**, 188 (2015)
98. J.A.Kilner, R.J.Brook. *Solid State Ionics*, **6**, 237 (1982)
99. S.Omar, E.D.Wachsman, J.L.Jones, J.C.Nino. *J. Am. Ceram. Soc.*, **92**, 2674 (2009)
100. S.Omar, E.D.Wachsman, J.C.Nino. *Solid State Ionics*, **177**, 3199 (2006)
101. T.S.Zhang, J.Ma, L.B.Kong, S.H.Chan, J.A.Kilner. *Solid State Ionics*, **170**, 209 (2004)
102. C.Sánchez-Bautista, A.J.Dos Santos-García, J.Peña-Martínez, J.Canales-Vázquez. *Solid State Ionics*, **181**, 1665 (2010)
103. E.Ruiz-Trejo, J.A.Kilner. *J. Appl. Electrochem.*, **39**, 523 (2009)
104. R.O.Fuentes, R.T.Baker. *J. Power Sources*, **186**, 268 (2009)
105. H.Keqin, F.Man, J.B.Goodenough. *J. Am. Ceram. Soc.*, **81**, 357 (1998)
106. K.R.Reddy, K.Karan. *J. Electroceram.*, **15**, 45 (2005)
107. N.Cioateră, V.Pârvulescu, A.Rolle, R.N.Vannier. *Solid State Ionics*, **180**, 681 (2009)
108. L.P.Li, X.M.Lin, G.S.Li, H.Inomata. *J. Mater. Res.*, **16**, 3207 (2001)
109. L.Aneflous, J.A.Musso, S.Villain, J.R.Gavarri, H.Benyaich. *J. Solid State Chem.*, **177**, 856 (2004)
110. I.E.L.Stephens, J.A.Kilner. *Solid State Ionics*, **177**, 669 (2006)
111. J.X.Zhu, D.F.Zhou, S.R.Guo, J.F.Ye, X.F.Hao, X.Q.Cao, J.Meng. *J. Power Sources*, **174**, 114 (2007)
112. J.Koettgen, S.Grieshammer, P.Hein, B.O.H.Grope, M.Nakayama, M.Martin. *Phys. Chem. Chem. Phys.*, **20**, 14291 (2018)
113. B.Steele. *Solid State Ionics*, **129**, 95 (2000)
114. S.J.Hong, K.Mehta, A.V.Virkar. *J. Electrochem. Soc.*, **145**, 638 (1998)
115. A.Tschöpe, S.Kilassonia, R.Birringer. *Solid State Ionics*, **173**, 57 (2004)
116. R.A.De Souza. *Phys. Chem. Chem. Phys.*, **11**, 9939 (2009)
117. A.Tschöpe, C.Bäuerle, R.Birringer. *J. Appl. Phys.*, **95**, 1203 (2004)
118. A.Tschöpe. *J. Electroceram.*, **14**, 5 (2005)
119. M.C.Göbel, G.Gregori. *Phys. Chem. Chem. Phys.*, **16**, 10175 (2014)
120. D.V.Laethem, J.Deconinck, D.Depla, A.Hubin. *J. Eur. Ceram. Soc.*, **36**, 1983 (2016)
121. D.V.Laethem, J.Deconinck, A.Hubin. *J. Eur. Ceram. Soc.*, **39**, 432 (2019)
122. I.Kosacki, C.Rouleau, P.Becher, J.Bentley, D.H.Lowndes. *Solid State Ionics*, **176**, 1319 (2005)
123. I.Kosacki, T.Suzuki, V.Petrovsky, H.U.Anderson. *Solid State Ionics*, **136** – **137**, 1225 (2000)
124. M.G.Bellino, D.G.Lamas, N.E.Walsoe de Reca. *Adv. Funct. Mater.*, **16**, 107 (2006)
125. V.V.Ivanov, S.N.Shkerin, A.A.Rempel, V.R.Khrustov, A.S.Lipilin, A.V.Nikonov. *Dokl. Phys. Chem.*, **433**, 125 (2010)
126. V.V.Ivanov, A.S.Lipilin, Yu.A.Kotov, V.R.Khrustov, S.N.Shkerin, S.N.Paranin, A.V.Spirin, A.S.Kaygorodov. *J. Power Sources*, **159**, 605 (2006)
127. V.P.Gorelov, S.V.Zayats, V.V.Ivanov, S.Yu.Ivin, Yu.A.Kotov, A.I.Medvedev, N.I.Moskalenko, A.M.Murzakaev, O.M.Samatov, V.R.Khrustov. *Glass Phys. Chem.*, **31**, 471 (2005)
128. G.Gregory, R.Merke, J.Maier. *Prog. Mater. Sci.*, **89**, 252 (2017)
129. V.P.Gorelov, V.B.Balakireva, I.Yu.Yaroslavtsev, V.A.Kazantsev, E.G.Vaganov. *Russ. J. Electrochem.*, **43**, 888 (2007)
130. S.Wang, M.Katsuki, T.Hashimoto, M.Dokiya. *J. Electrochem. Soc.*, **150**, A952 (2003)
131. E.C.C.Souza, W.C.Chueh, W.Jung, E.N.S.Muccillo, S.M.Haile. *J. Electrochem. Soc.*, **159**, K127 (2012)
132. E.Pikalova. *Solid Solutions on the base of CeO_2: Synthesis, Physico-Chemical Properties, Application in High-temperature Electrochemistry*. (Lambert Academic Publishing, 2012)
133. T.Kudo, H.Obayashi. *J. Electrochem. Soc.*, **123**, 415 (1976)

134. L.Navarro, F.Marques, J. Frade. *J. Electrochem. Soc.*, **144**, 267 (1997)
135. K.L.Duncan, E.D.Wachsman. *Ionics*, **13**, 127 (2007)
136. H.Yahiro, K.Eguchi, H.Arai. *Solid State Ionics*, **36**, 71 (1989)
137. H.Arai, T.Kunisaki, Y.Shimizu, T.Seiyama. *Solid State Ionics*, **20**, 241 (1986)
138. H.Yahiro, K.Eguchi, H.Arai. *Solid State Ionics*, **21**, 37 (1986)
139. S.Wang, T.Kobayashi, M.Dokiya, T.Hashimoto. *J. Electrochem. Soc.*, **147**, 3606 (2000)
140. D.Schneider, M.Godickemeier, L.J.Gauckler. *J. Electroceram.*, **1**, 165 (1997)
141. M.Godickemeier. *Mixed Ionic Electronic Conductors for Solid Oxide Fuel Cells: Doctoral Thesis*. Swiss Federal Institute of Technology, Zürich, 1996; https://www.research-collection.ethz.ch/handle/20.500.11850/14-2540 (last access 27.05.2021)
142. D. Pérez Coll. *Mixed Conducting Materials for Solid Oxide Fuel Cells*; https://www.icv.csic.es/images/Difusion/DISSEMI-NATION_Mixed_conducting_materials_for_SOFCs.pdf (last access 27.05.2021)
143. M.Godickemeier, L.J.Gauckler. *J. Electrochem. Soc.*, **145**, 414 (1998)
144. I.Riess. *J. Eectrochem. Soc.*, **128**, 2077 (1981)
145. S.Omar, E.D.Wachsman, J.C.Nino. *Solid State Ionics*, **178**, 1890 (2008)
146. M.Dudek. *J. Eur. Ceram. Soc.*, **28**, 965 (2008)
147. X.Sha, Z.Lü, X.Huang, J.Miao, L.Jia, X.Xin, W.Su. *J. Alloys Compd.*, **424**, 315 (2006)
148. X.Sha, Z.Lü, X.Huang, J.Miao, Z.Liu, X.Xin, Y.Zhang, W.Su. *J. Alloys Compd.*, **433**, 274 (2007)
149. J.A.Lane, J.L.Neff, G.M.Chrisitie. *Solid State Ionics*, **177**, 1911 (2006)
150. P.-S.Cho, S.B.Lee, D.-S.Kim, J.-H.Lee, D.-Y.Kim, H.-M.Park. *Electrochem. Solid State Lett.*, **9**, A399 (2006)
151. P.-S.Cho, S.B.Lee, Y.-H.Cho, D.-Y.Kim, H.-M.Park, J.-H.Lee. *J. Power Sources*, **183**, 518 (2008)
152. E.Yu.Pikalova, A.A.Murashkina, D.A.Medvedev. *Russ. J. Electrochem.*, **47**, 681 (2011)
153. P.-S.Cho, S.B.Lee, Y.-H.Cho, D.-Y.Kim, H.-M.Park, G.Auchterlonie, J.Drennan, J.-H.Lee. *J. Electrochem. Soc.*, **156**, B339 (2009)
154. E.Yu.Pikalova, A.A.Kolchugin, V.G.Bamburov. *J. Energy Prod. Manag.*, **1**, 272 (2016)
155. E.Yu.Pikalova, A.A.Murashkina, V.I.Maragou, A.K.Demin, V.N.Strekalovsky, P.E.Tsiakaras. *Int. J. Hydrogen Energy*, **36**, 6175 (2011)
156. F.-Y.Wang, B.-Z.Wan, S.Cheng. *J. Solid State Electrochem.*, **9**, 168 (2005)
157. T.Zhang, P.Hing, H.Huang, J.Kilner. *Solid State Ionics*, **148**, 567 (2002)
158. R.Peng, C.Xia, Q.Fu, G.Meng, D.Peng. *Mater. Lett.*, **56**, 1043 (2002)
159. A.V.Coles-Aldridge, R.T.Baker. *Solid State Ionics*, **316**, 9 (2018)
160. S.Omar, E.D.Wachsman, J.C.Nino. *Appl. Phys. Lett.*, **91**, 144106 (2007)
161. B.Li, Y.Liu, X.Wei, W.Pan. *J. Power Sources*, **195**, 969 (2010)
162. D.R.Ou, F.Ye, T.Mori. *Phys. Chem. Chem. Phys.*, **13**, 9554 (2011)
163. M.Burbano, S.Nadin, D.Marrocchelli, M.Salanne, G.M.Watson. *Phys. Chem. Chem. Phys.*, **16**, 8320 (2014)
164. M.Chen, H.Gao, L.Zhang, Y.Xuan, J.Ren, M.Ni, Z.Lin. *Ceram. Int.*, **45**, 3977 (2019)
165. K.A.Bhabu, J.Theertagiri, J.Madhavan, T.Balu, T.R.Rajasekaran. *J. Phys. Chem. C*, **120**, 18452(2016)
166. W.Zając, J.Molenda. *Solid State Ionics*, **179**, 154 (2008)
167. M.Gupta, S.Shirbhate, P.Ojha, S.Acharya. *Solid State Ionics*, **320**, 199 (2018)
168. A.Arabaci, T.G.Altınçekiç, M.Der, M.A.F.Öksüzömer. *J. Alloys Compd.*, **792**, 1141 (2019)
169. C.Madhuri, K.Venkataramana, A.Nurhayati, C.Vishnuvardhan Reddy. *Curr. Appl. Phys.*, **18**, 1134 (2018)
170. A.S.Babu, R.Bauri. *ECS Trans.*, **57**, 1115 (2013)
171. A.Arabaci. *Solid State Ionics*, **326**, 69 (2018)
172. S.Ramesh, K.S.J.Raju. *Int. J. Hydrogen Energy*, **37**, 10311 (2012)
173. D.L.Maricle, T.E.Swarr, S.Karavolis. *Solid State Ionics*, **52**, 173 (1992)
174. K.Venkataramana, C.Madhuri, C.Madhusudan, Y.Suresh Reddy, G.Bhikshamaiah, C.Vishnuvardhan Reddy. *Ceram. Int.*, **44**, 6300(2018)
175. C.Artini, L.Gigli, M.M.Carnasciali, M.Pani. *Inorganics*, **7** (8), 94 (2019)
176. T.Mori, J.Drennan, Y.Wang, J.- G.Li, T.Ikegami. *J. Therm. Anal. Calorim.*, **70**, 309 (2002)
177. T.Mori, J.Drennan, Y.Wang, J.-H.Lee, J.-G.Li, T.Ikegami. *J. Electrochem. Soc.*, **150**, A665 (2003)
178. H.Yamamura, E.Katoh, M.Ichikawa, K.Kakinuma, T.Mori, H.Haneda. *Electrochemistry*, **68**, 455 (2000)
179. T.Mori, H.Yamamura. *J. Mater. Synth. Process.*, **6**, 175 (1998)
180. Patent EP 0722194A1 (1996)
181. E.Yu.Pikalova, V.G.Bamburov, I.V.Rukavishnikova, A.K.Demin, A.A.Kolchugin. *WIT Trans. Ecology Environ.*, **190**, 261 (2014)
182. D.Medvedev. *Int. J. Hydrogen Energy*, **44**, 26711 (2019)
183. D.Medvedev, Yu.Lyagaeva, S.Plaksin, A.Demin, P.Tsiakaras. *J. Power Sources*, **273**, 716 (2015)
184. D.Medvedev, A.Murashkina, E.Pikalova, A.Demin, A.Podias, P.Tsiakaras. *Prog. Mater Sci.*, **60**, 72(2014)
185. W.Wang, D.Medvedev, Z.Shao. *Adv. Funct. Mater.*, **28**, 1802592 (2018)
186. D.Hirabayashi, A.Tomita, S.Teranishi, T.Hibino, M.Sano. *Solid State Ionics*, **176**, 881 (2005)
187. A.Venkatasubramanian, P.Gopalan, T.R.S.Prasanna. *Int. J. Hydrogen Energy*, **35**, 4597 (2010)
188. M.Khadelwal, A.Venkatasubramanian, T.R.S.Prasanna, P.Gopalan. *J. Eur. Ceram. Soc.*, **31**, 559 (2011)
189. W.Sun, Y.Jiang, Y.Wang, S.Fang, Z.Zhu, W.Liu. *J. Power Sources*, **196**, 62 (2011)
190. J.Huang, L.Zhang, C.Wang, P.Zhang. *Int. J. Hydrogen Energy*, **37**, 13044 (2012)
191. D.Medvedev, V.Maragou, E.Yu.Pikalova, A.K.Demin, P.Tsiakaras. *J. Power Sources*, **221**, 217 (2012)
192. D.Medvedev, E.Pikalova, A.Demin, A.Podias, I.Korzun, B.Antonov, P.Tsiakaras. *J. Power Sources*, **267**, 269 (2014)
193. H.Sun, X.Guo, F.Yu, Z.Yang, G.Li, J.Li, H.Ding, F.Meng, Z.Fan, P.Wang, W.Yan, Z.Hu. *Ceram. Int.*, **45**, 7667(2019)
194. M.Irshad, K.Siraj, R.Raza, A.Ali, P.Tiwari, B.Zhu, A.Rafique, A.Ali, M.K.Ullah, A.Usman. *Appl. Sci.*, **6**, 75 (2016)
195. J.A.Greer. *J. Phys. D: Appl. Phys.*, **47**, 034005 (2014)
196. H.-W.Lee, H.-I.Ji, J.-H.Lee, B.-K.Kim, K.J.Yoon, J.-W.Son. *J. Korean Ceram. Soc.*, **56**, 130 (2019)
197. E.Pikalova, E.Kalinina. *Int. J. Energy Prod. Manag.*, **4**, 1 (2019)
198. E.G.Kalinina, E.Yu.Pikalova. *Russ. Chem. Rev.*, **88**, 1179 (2019)
199. E.Yu.Pikalova, E.G.Kalinina. *Renew. Sustain. Energ. Rev.*, **116**, 109440 (2019)
200. I.Aznam, J.C.W.Mah, A.Muchtar, M.R.Samalu, M.J.Ghazali. *Zhejiang Univ.-Sci. A: Appl. Phys. Eng.*, **19**, 811 (2018)
201. C.Seok, J.Moon, M.Park, J.Hong, H.Kim, J.-W.Son, J.-H.Lee, B.-K.Kim, H.W.Lee, K.J.Yoon. *J. Eur. Ceram. Soc.*, **36**, 1417 (2016)
202. E.-O.Oh, C.-M.Whang, Y.-R.Lee, S.-Y.Park, D.H.Prasad, K.J.Yoon, J.-W.Son, J.-H.Lee, H.-W.Lee. *Adv. Mater.*, **24**, 3373 (2012)

203. H.Ichiboshi, K.Myoujin, T.Kodera, T.Ogihara. *Key Eng. Mater.*, **566**, 137 (2013)
204. S.Nakayama, M.Miyayama. *Key Eng. Mater.*, **350**, 175 (2007)
205. S.-M.Yu, K.-T.Lee. *J. Ceram. Process. Res.*, **17**, 290 (2016)
206. M.Matsuda, T.Hosomi, K.Murata, T.Fukui, M.Miyake. *J. Power Sources*, **165**, 102 (2007)
207. C.Kim, S.Kim, I.Jang, H.Yoon, T.Song, U.Paik. *J. Power Sources*, **415**, 112 (2019)
208. A.A.Solovyev, S.V.Rabotkin, A.V.Shipilova, I.V.Ionov. *Int. J. Electrochem. Sci.*, **14**, 575 (2019)
209. Z.Lu, X.Zhou, D.Fisher, J.Templeton, J.Stevenson, N.Wu, A.Ignatiev. *Electrochem. Commun.*, **12**, 179 (2010)
210. D.Yang, X.Zhang, S.Nikumb, C.Decès-Petit, R.Hui, R.Maric, D.Ghosh. *J. Power Sources*, **164**, 182 (2007)
211. Q.Su, D.Yoon, A.Chen, F.Khatkhatay, A.Manthiram, H.Wang. *J. Power Sources*, **242**, 455 (2013)
212. A.Tomita, Y.Tachi, T.Hibino, Electrochem. *Solid State Lett.*, **11**, B68 (2008)
213. A.Pesaran, A.Jaiswal, Y.Ren, E.D.Wachsman. *Ionics*, **25**, 3153 (2019)
214. A.N.Koval'chuk, A.V.Kuz'min, D.A.Osinkin, A.S.Farlenkov, A.A.Solov'ev, A.V.Shipilova, I.V.Ionov, N.M.Bogdanovich, S.M.Beresnev. *Russ. J. Electrochem.*, **54**, 541 (2018)
215. Z.Gong, W.Sun, D.Shan, Y.Wu, W.Liu. *ACS Appl. Mater. Interfaces*, **8**, 10835 (2016)
216. W.Sun, Z.Shi, Z.Wang, W.Liu. *J. Membr. Sci.*, **476**, 394 (2015)
217. Ju.Kim, Jo.Kim, K.J.Yoon, J.-W.Son, J.-H.Lee, J.-H.Lee, H.-W.Lee, H.-I.Ji. *J. Alloys Compd.*, **846**, 156318 (2020)
218. H.Sumi, E.Suda, M.Mori. *Int. J. Hydrogen Energy*, **42**, 4449 (2017)
219. J.S.Ahn, M.A.Camaratta, D.Pergolesi, K.T.Lee, H.Yoon, B.W.Lee, D.W.Jung, E.Traversa, E.D.Wachsman. *J. Electrochem. Soc.*, **157**, B376 (2010)
220. K.T.Lee, D.W.Jung, M.A.Camaratta, H.S.Yoon, J.S.Ahn, E.D.Wachsman. *J. Power Sources*, **205**, 122 (2012)
221. J.-Y.Park, E.D.Wachsman. *Ionics*, **12**, 15 (2006)
222. J.Hou, L.Bi, J.Qian, Z.Gong, Z.Zhu, W.Liu. *J. Power Sources*, **301**, 306 (2016)
223. B.-K.Park, S.A.Barnett. *J. Mater. Chem. A*, **8**, 11626 (2020)
224. B.Shri Prakash, R.Pavitra, S.Sentil Kumar, S.T.Aruna. *J. Power Sources*, **381**, 136 (2018)
225. T.Mukai, S.Tsukui, K.Yoshida, S.Yamaguchi, R.Hatayama, M.Adachi, H.Ishibashi, Y.Kakehi, K.Satoh, T.Kusaka, K.C.Goretta. *J. Fuel Cell Sci. Technol.*, **10**, 061006(1) (2013)
226. C.Xia, M.Liu. *Solid State Ionics*, **144**, 249 (2001)
227. P.Pianko-Oprych, T.Zinko, Z.Jaworski. *Materials*, **9**, 814 (2016)
228. X.Jin, X.Xue. *RSC Adv.*, **4**, 15782 (2014)
229. E.Olsson, J.Cottom, X.Aparicio-Anglès, N.H.de Leeu. *Phys. Chem. Chem. Phys.*, **22**, 692 (2020)
230. I.Kim, M.Choi. *ACS Omega*, **4**, 10960 (2019)
231. S.B.Adler. *Chem. Rev.*, **104**, 4791 (2004)
232. A.Schmid. *Diffusion Gas Electrode*. F.Fnke, Stuttgart, 1923
233. M.Kleitz. *Solid State Ionics*, **92**, 65 (1996)
234. S.B.Adler. *J. Electrochem. Soc.*, **143**, 3554 (1996)
235. J.E.Mortensen, M.Søgaard, T.Jacobsen. *ECS Trans.*, **28** (11), 17 (2010)
236. J.Fleig, J.Maier. *J. Eur. Ceram. Soc.*, **24**, 1343 (2004)
237. B.Ruger, A.Weber, E.Ivers-Tiffee. *ECS Trans.*, **7**, 2065 (2007)
238. L.Almar, J.Szász, A.Weber, E.Ivers-Tiffée. *J. Electrochem. Soc.*, **164**, F289 (2017)
239. A.L.Gavrilyuk, D.A.Osinkin, D.I.Bronin. *Russ. J. Electrochem.*, **53**, 575 (2017)
240. B.A.Boukamp, A.Rolle. *Solid State Ionics*, **314**, 103 (2018)
241. C.Kreller, M.Drake, S.B.Adler, H.-Y.Chen, H.-C.Yu, K.Thornton, J.R.Wilson, S.A.Barnett. *ECS Trans.*, **35** (1), 815 (2011)
242. N.S.Choudhury, J.W.Patterson. *J. Electrochem. Soc.*, **118**, 1398 (1971)
243. D.S.Tannhauser. *J. Electrochem. Soc.*, **125**, 1277 (1978)
244. I.Riess. *Solid State Ionics*, **52**, 127 (1992)
245. K.L.Duncan, E.D.Wachsman. *J. Electrochem. Soc.*, **156**, B1030 (2009)
246. K.L.Duncan, K.T.Lee, E.D.Wachsman. *J. Power Sources*, **196**, 2445 (2011)
247. S.L.Shen, M.Ni. *Int. J. Hydrogen Energy*, **40**, 5160 (2015)
248. S.L.Shen, Y.Kuang, K.Q.Zheng, Q.Y.Gao. *Solid State Ionics*, **315**, 44 (2018)
249. A.V.Virkar. *J. Electrochem. Soc.*, **138** 1481 (1991)
250. M.B.Marques, L.M.Navarro. *Solid State Ionics*, **90**, 183 (1996)
251. X.X.Wang, T.Zhang, J.H.Kang, L.Zhao, L.T.Guo, P.Z.Feng, F.B.Zhou, Y.H.Ling. *Electrochim. Acta*, **248**, 356 (2017)
252. Z.K.Ma, Z.Song, X.X.Wang, X.M.Ou, K.Q.Zheng, L.T.Guo, P.Z.Feng, S.R.Wang, F.B.Zhou, Y.H.Ling. *ACS Appl. Energy Mater.*, **2**, 3142 (2019)
253. M.Mozdzierz, K.Berent, S.Kimijima, J.S.Szmyd, G.Brus. *Catalysts*, **9**, 253 (2019)
254. H.Xu, Z.Dang, B.-F.Bai. *Energy*, **67**, 575 (2014)
255. W.Sigle, J.Fleig, J.Maier. *Solid State Ionics*, **154 – 155**, 555 (2002)
256. T.Suzuki, I,Kosacki, H.U.Anderson. *Solid State Ionics*, **151**, 111 (2002)
257. X.Wang, Y.Ma, B.Zhu. *Int. J. Hydrogen. Energy*, **37**, 19417 (2012)
258. L.Fan, C.Wang, M.Chen, B.Zhu. *J. Power Sources*, **234**, 154 (2013)
259. R.Raza, B.Zhu, A.Rafique, M.R.Naqui, P.Lund. *Mater. Today Energy*, **15**, 100373 (2020)
260. V.S.Bagotsky. *Fuel Cells: Problems and Solutions*. (Hoboken, NJ: Wiley, 2009)
261. N.F.Uvarov, O.P.Shrivastava, E.F.Hairetdinov. *Solid State Ionics*, **36**, 39 (1989)
262. N.F.Uvarov, V.G.Ponomareva, G.V.Lavrova. *Russ. J. Electrochem.*, **46**, 722 (2010)
263. N.F.Uvarov, P.Vaněk. *J. Mater. Synth. Process.*, **8**, 319 (2000)
264. C.Xia, Y.Li, Y.Tian, Q.Liu, Z.Wang, L.Jia, Y.Zhao, Y.Li. *J. Power Sources*, **195**, 3149 (2010)
265. T.Cai, Y.Zeng, S.Yin, L.Wang, C.Li. *Mater. Lett.*, **65**, 2751 (2011)
266. F.Xu, C.Li, Z.Wang, Z.Ye, Y.Zhang, Y.Zeng. *J. Rare Earths*, **34**, 711 (2016)
267. J.-T.Kim, T.-H.Lee, K.Y.Park, Y.Seo, K.B.Kim, S.-J.Song, B.Park, J.-Y.Park. *J. Power Sources*, **275**, 563 (2015)
268. R.Chockalingam, S.Basu. *Int. J. Hydrogen Energy*, **36**, 14977 (2011)
269. M.Benamira, A.Ringuedé, L.Hildebrandt, C.Lagergren, R.N.Vannier, M.Cassir. *Int. J. Hydrigen Energy*, **37**, 19371 (2012)
270. A.S.V.Ferreira, C.M.C.Soares, F.M.H.L.Figueiredo, F.M.B.Marques. *Int. J. Hydrogen Energy*, **36**, 3704 (2011)
271. S.Rajesh, D.A.Macedo, R.M.Nascimento, G.L.Souza, F.M.L.Figueiredo, F.M.B.Marques. *Int. J. Hydrogen Energy*, **38**, 16539 (2013)
272. M.Anwar, S.A.Muhammed Ali, A.Muchtar, M.R.Somalu. *J. Alloys Compd.*, **775**, 571 (2019)
273. N.Jaiswal, D.Kumar, S.Upadhyay, O.Parkash. *Trans. Indian Inst. Met.*, **72**, 2029 (2019)
274. Y.Ma, X.Wang, H.A.Khalifa, B.Zhu, M.Muhammed. *Int. J. Hydrogen Energy*, **37**, 19401 (2012)
275. A.Maheshwari, H.-D.Wiemhöfer. *Acta Mater.*, **103**, 361 (2016)
276. L.Zhang, R.Lan, A.Kraft, S.Tao. *Electrochem. Commun.*, **13**, 582 (2011)
277. W.Liu, Y.Liu, B.Li, T.D.Sparks, X.Wei, W.Pan. *Compos. Sci. Technol.*, **70**, 181 (2010)
278. R.Raza, X.Wang, Y.Ma, B.Zhu. *J. Power Sources*, **195**, 6491 (2010)

279. M.I.Asghar, S.Jouttijärvi, P.D.Lund. *Int. J. Hydrogen Energy*, **43**, 12797 (2018)
280. G.Y.Meng, Q.X.Fu, S.W.Zha, C.R.Xia, X.Q.Liu, D.K.Peng. *Solid State Ionics*, **148**, 533 (2002)
281. J.Huang, Z.Gao, Z.Mao. *Int. J. Hydrogen Energy*, **35**, 4270 (2010)
282. C.M.C.Soares, S.G.Patrício, F.M.H.L.Figueiredo, F.M.B.Marques. *Int. J. Hydrogen Energy*, **39**, 5424 (2014)
283. W.Zhu, C.Xia, D.Ding, X.Shi, G.Meng. *Mater. Res. Bull.*, **41**, 2057 (2006)
284. S.A.Muhammed Ali, A.Muchtar, A.Bakar Sulong, N.Muhamad, E.H.Majlan. *Ceram. Int.*, **39**, 5813 (2013)
285. Q.X.Fu, S.W.Zha, W.Zhang, D.K.Peng, G.Y.Meng, B.Zhu. *J. Power Sources*, **104**, 73 (2002)
286. H.Wang, R.Du, H.Zhai, G.Xi, F.Wu. *Ceram. Int.*, **46**, 2677 (2020)
287. W.M.Lv, Z.Tong, Y.M.Yin, Z.F.Ma. *Nano-Micro Lett.*, **7**, 268 (2015)
288. R.Li, C.Li, L.Cao, Y.Zeng, Z.Wang, Z.Ye, Y.Zhang. *Ceram. Int.*, **43**, 12191 (2017)
289. C.Li, Y.Zeng, Z.Wang, F.Xu, Z.Ye, R.Shi. *Electrochim. Acta*, **212**, 583 (2016)
290. L.Zhang, R.Lan, C.T.G.Petit, S.W.Tao. *Int. J. Hydrogen Energy*, **35**, 6934 (2010)
291. B.Zhu, S.Li, B.-E.Mellander. *Electrochem. Commun.*, **10**, 302 (2008)
292. T.Schober. *Electrochem. Solid-State Lett.*, **8**, A199 (2005)
293. A.B.Yaroslavtsev. *Russ. Chem. Rev.*, **78**, 1013 (2009)
294. H.Näfe. *Ionics*, **22**, 297 (2016)
295. C.Ricca, V.Albin, F.Labat, C.Adamo, M.Cassir, A.Ringuedé. *Int. J. Hydrogen Energy*, **41**, 18778 (2016)
296. C.Ricca, A.Grishin, A.Ringuedé, M.Cassir, C.Adamo, F.Labat. *J. Mater. Chem. A*, **4**, 17473 (2016)
297. J.Patakangas, Y.Ma, P.Lund. *J. Power Sources*, **263**, 315 (2014)
298. A.Devidson, M.Tinkham. *Phys. Rev. B*, **13**, 3261 (1976)
299. T.Ristoiu, T.Petrisor Jr., M.Gabor, S.Rada, F.Popa, L.Ciontea, T.Petrisor. *J. Alloys Compd.*, **532**, 109 (2012)
300. M.Mizuata, Y.Harada, G.Cha, A.Bienvenu Béleké. *J. Electrochem. Soc.*, **151**, E179 (2004)
301. P.Mallet, C.A.Guerin, A.Sentenac. *Phys. Rev. B*, **72**, 014205 (2005)
302. S.Kirkpatrick. *Rev. Mod. Pys.*, **45**, 574 (1973)
303. R.Landauer. *J. Appl. Phys.*, **23**, 779 (1952)
304. J.Di, M.Chen, C.Wang, J.Zheng, L.Fan, B.Zhu. *J. Power Sources*, **195**, 4695 (2010)
305. M.I.Asghar, M.Heikkilä, P.Lund. *Mater. Today Energy*, **5**, 338 (2017)
306. L.Zhang, X.Li, S.Wang, K.G.Romito, K.Huang. *Electrochem. Commun.*, **13**, 554 (2011)
307. Sh.Yin, Zh.Ye, Ch.Li, X.Chen, Y.Zeng. *Mater. Lett.*, **92**, 78 (2013)
308. X.Wang, Y.Ma, S.Li, B.Zhu, M.Muhammed. *Int. J. Hydrogen Energy*, **37**, 19380 (2012)
309. X.Wang, Y.Ma, S.Li, A.-H.Kashyout, B.Zhu, M.Muhammed. *J. Power Sources*, **196**, 2754 (2011)
310. L.Fan, G.Zhang, M.Chen, C.Wang, J.Di, B.Zhu. *Int. J. Electrochem. Sci.*, **7**, 8420 (2012)
311. Z.Qiao, C.Xia, Y.Cai, M.Afzal, H.Wang, J.Qiao, B.Zhu. *J. Power Sources*, **392**, 33 (2018)
312. A.Ali, A.Rafique, M.Kaleemullah, G.Abbas, M.A.Khan, M.A.Ahmad, R.Raza. *ACS Appl. Mater. Interfaces*, **10**, 806 (2018)
313. C.Xia, Yu.Li, Y.Tian, Q.Liu, Y.Zhao, L.Jia, Yo.Li. *J. Power Sources*, **188**, 156 (2009)
314. Y.Li, Z.Rui, C.Xia, M.Anderson, Y.S.Lin. *Catal. Today*, **148**, 303 (2009)
315. Y.Gong, X.Li, L.Zhang, W.Tharp, C.Qin, K.Huang. *J. Electrochem. Soc.*, **161**, F226 (2014)
316. C.Qin, A.Gladney. *Comput. Theor. Chem.*, **999**, 179 (2012)
317. X.Lei, K.Haines, K.Huang, C.Qin. *J. Power Sources*, **305**, 161 (2016)
318. Y.Gong, X.Li, L.Zhang, W.Tharp, C.Qin, K.Huang. *J. Electrochem. Soc.*, **160**, F958 (2013)
319. P.Xue, H.Wu, Y.Lu, X.Zhu. *J. Mater. Sci. Technol.*, **34**, 914 (2018)
320. R.Raza, H.Qin, Q.Liu, M.Samavati, R.B.Lima, B.Zhu. *Adv. Energy Mater.*, **1**, 1225 (2011)
321. Z.Gao, R.Raza, B.Zhu, Z.Mao. *Int. J. Energy Res.*, **35**, 690 (2010)
322. P.Tomczyk. *J. Power Sources*, **160**, 852 (2006)
323. C.Zhao, Y.Li, W.Zhang, Y.Zheng, X.Lou, B.Yu, J.Chen, Y.Chen, M.Liu, J.Wang. *Energy Environ. Sci.*, **13**, 53 (2020)
324. I.Garbayo, F.Baiutti, A.Morata, A.Tarancón. *J. Eur. Ceram. Soc.*, **39**, 101 (2019)
325. J.Garcia-Barriocanal, A.Rivera-Calzada, M.Varela, Z.Sefrioui, E.Iborra, C.Leon, S.J.Pennycook, J.Santamaria. *Science*, **321**, 676 (2008)
326. X.Guo. *Science*, **324**, 465 (2009)
327. A.Cavallaro, M.Burriel, J.Roqueta, A.Apostolidis, A.Bernardi, A.Tarancón, R.Srinivasan, S.N.Cook, H.Fraser, J.A.Kilner, D.W.McComb, J.Santiso. *Solid State Ionics*, **181**, 592 (2010)
328. J.D.Gale. *J. Chem. Soc., Faraday Trans.*, **93**, 629 (1997)
329. N.Schichtel, C.Korte, D.Hesse, J.Janek. *Phys. Chem. Chem. Phys.*, **11**, 3043 (2009)
330. A.Kushima, B.Yildiz. *J. Mater. Chem.*, **20**, 4809 (2010)
331. R.A.De Souza, A.Ramadan, S.Hörner. *Energy Environ. Sci.*, **5**, 5445 (2012)
332. M.Sillassen, P.Eklund, N.Pryds, E.Johnson, U.Helmersson, J.Bøttiger. *Adv. Funct. Mater.*, **20**, 2071 (2010)
333. Y.M.Chiang, E.B.Lavik, I.Kosacki, H.L.Tuller, J.Y.Ying. *Appl. Phys. Lett.*, **69** (2), 185 (1996)
334. H.Näfe. *Ionics*, **24**, 763 (2018)
335. S.M.Yang, S.Lee, J.Jian, W.Zhang, P.Lu, Q.Jia, H.Wang, T.W.Noh, S.V.Kalinin, J.L.MacManus-Driscoll. *Nat. Commun.*, **6**, 8588 (2015)
336. J.Mittra, G.J.Abraham, M.Kesaria, S.Bahl, A.Gupta, S.M.Shivaprasad, C.S.Viswanadham, U.D.Kulkarni, G.K.Dey. *Mater. Sci. Forum*, **710**, 757 (2012)
337. Q.Lei, M.Golalikhani, B.A.Davidson, G.Liu, D.G.Schlom, Q.Qiao, Y.Zhu, R.U.Chandrasena, W.Yang, A.X.Gray, E.Arenholz, A.K.Farrar, D.A.Tenne, M.Hu, J.Guo, R.K.Singh, X.Xi. *Quantum Mater.*, **2**, 10 (2017)
338. J.L.MacManus-Driscoll. *Adv. Funct. Mater.*, **20**, 2035 (2010)
339. J.W.Cahn. *Acta Metall.*, **9**, 795 (1961)
340. Y.Ni, A.G.Khachaturyan. *Acta Mater.*, **56**, 4498 (2008)
341. M.Sase, F.Hermes, K.Yashiro, K.Sato, J.Mizusaki, T.Kawada, N.Sakai, H.Yokokawa. *J. Electrochem. Soc.*, **155**, B793 (2008)
342. J.Crumlin, E.Mutoro, S.-J.Ahn, G.J.la O', D.N.Leonard, A.Borisevich, M.D.Biegalski, H.M.Christen, Y.Shao-Horn. *J. Phys. Chem. Lett.*, **1**, 3149 (2010)
343. J.Yoon, S.Cho, J-H.Kim, J.H.Lee, Z.Bi, A.Serquis, X.Zhang, A.Manthiram, H.Wang. *Adv. Funct. Mater.*, **19**, 3868 (2009)
344. W.Ma, J.J.Kim, N.Tsvetkov, T.Daio, Y.Kuru, Z.Cai, Y.Chen, K.Sasaki, H.L.Tuller, B.Yildiz. *J. Mater. Chem.*, **3**, 207 (2015)
345. Y.Zheng, Y.Li, T.Wu, W.Zhang, J.Zhu, Z.Li, J.Chen, B.Yu, J.Wang, J.Zhang. *Nano Energy*, **51**, 711 (2018)
346. J.W.Han, B.Yildiz. *Energy Environ. Sci.*, **5**, 8598 (2012)
347. M. J.Gadre, Y.-L.Lee, D.Morgan. *Phys. Chem. Chem. Phys.*, **14**, 2606 (2012)
348. Y.Chen, Z.Cai, Y.Kuru, W.Ma, H.L.Tuller, B.Yildiz. *Adv. Eng. Mater.*, **3**, 1221 (2013)
349. D.Ding, X.Li, S.Y.Lai, K.Gerdes, M.Liu. *Energy Environ. Sci.*, **7**, 552 (2014)
350. A.J.Samson, M.Søgaard, N.Bonanos. *Electrochem. Solid-State Lett.*, **15**, B54 (2012)

351. R.Kiebach, C.Knöfel, F.Bozza, T.Klemensø, C.Chatzichristodoulou. *J. Power Sources*, **228**, 170 (2013)
352. S.Lee, K.Gerdes. *ECS Electrochem. Lett.*, **4**, F17 (2015)
353. K.K.Hansen, M.Wandel, Y.-L.Liu, M.Mogensen. *Electrochim. Acta*, **55**, 4606 (2010)
354. S.P.Jiang, W.Wang. *J. Electrochem. Soc.*, **152**, A1398 (2005)
355. Z.Jiang, L.Zhang, K.Feng, C.Xia. *J. Power Sources*, **185**, 40 (2008)
356. M.Shah, S.A.Barnett. *Solid State Ionics*, **179**, 2059 (2008)
357. M.Shah, P.W.Voorhees, S.A.Barnett. *Solid State Ionics*, **187**, 64 (2011)
358. C.Sındıraç, A.Büyükaksoy, S.Akkurt. *J. Sol-Gel Sci. Technol.*, **92**, 45 (2019)
359. I.Yu.Yaroslavtsev, B.L.Kuzin, D.I.Bronin, G.K.Vdovin, N.M.Bogdanovich. *Russ. J. Electrochem.*, **45**, 875 (2009)
360. A.I.Vshivkova, V.P.Gorelov. *Russ. J. Electrochem.*, **52**, 488 (2016)
361. Y.Yang, M.Li, Y.Ren, Y.Li, C.Xia. *Int. J. Hydrogen Energy*, **43**, 3797 (2018)
362. Q.Yang, F.Chai, C.Ma, C.Sun, S.Shi, L.Chen. *J. Mater. Chem. A*, **4**, 18031 (2016)
363. T.Hong, F.Chen, C.Xia. *Electrochem. Commun.*, **51**, 93 (2015)
364. L.Zhang, T.Hong, Y.Li, C.Xia. *Int. J. Hydrogen Energy*, **42**, 17242 (2017)
365. D.A.Osinkin. *Electrochim. Acta*, **330**, 135257 (2020)
366. E.Hu, Z.Jiang, L.Fan, M.Singh, F.Wang, R.Raza, M.Sajid, J.Wang, J.-S.Kim, B.Zhu. *Science*, **24**, 102191 (2021)
367. Y.Zhang, J.Liu, M.Singh, E.Hu, Z.Jiang, R.Raza, F.Wang, J.Wang, F.Yang, B.Zhu. *Nano-Micro Lett.*, **12**, 178 (2020)
368. S.V.Jouttijärvi, M.I.Asghar, P.D.Lund. *Catal. Today*, **364**, 104 (2021)
369. B.Zhu, L.Ma, X.D.Wang, R.Raza, H.Y.Qin, L.D.Fan. *Electrochem. Commun.*, **13**, 225 (2011)
370. H.Hu, Q.Lin, Z.Zhu, X.Liu, M.Afzal, Y.He, B.Zhu. *J. Power Sources*, **275**, 476 (2015)
371. Q.Shi, J.Chen, Y.Xing, B.Zhu, Y.Wu. *J. Electrochem. Soc.*, **167**, 054504 (2020)
372. B.Wang, B.Zhu, S.Yun, W.Zhang, C.Xia, M.Afzal, Y.Cai, Y.Liu, Y.Wang, H.Wang. *NPG Asia Mater.*, **11**, 51 (2019)
373. Q.Liu, H.Qin, R.Raza, L.Fan,Y.Li, B.Zhu. *RSC Adv.*, **2**, 8036 (2012)
374. B.Zhu, R.Raza, H.Qin, L.Fan. *J. Power Sources*, **196**, 6362 (2011)
375. K.Zagorski, S.Wachowski, D.Szymczewska, A.Mielewczyk-Gryn, P.Jasinski, M.Gazda. *J. Power Sources*, **353**, 230 (2017)
376. T.Westermann, T.Melin. *Chem. Eng. Process.*, **48**, 17 (2009)
377. M.Kuhn, T.W.Napporn. *Energies*, **3**, 57 (2010)
378. T.Hibino, A.Hashimoto, M.Yano, M.Suzuki, S.Yoshida, M.Sano. *J. Electrochem. Soc*, **149**, A133 (2002)
379. Z.Shao, J.Mederos, W.C.Chueh, S.M.Haile. *J. Power Sources*, **162**, 589 (2006)
380. M.Yano, A.Tomita, M.Sano, T.Hibino. *Solid State Ionics*, **177**, 3351 (2007)
381. I.Riess, P.J.Van der Put, J.Schoonman. *Solid State Ionics*, **82**, 1 (1995)
382. I.Riess. *Solid State Ionics*, **176**, 1667 (2005)
383. Y.Guo, M.Bessaa, S.Aguado, M.C.Steil, D.Rembelski, M.Rieu, J.-P.Viricelle, N.Benameur, C.Guizard, C.Tardivat, P.Vernoux, D.Farrusseng. *Energy Environ. Sci.*, **6**, 2119 (2013)
384. C.Zang, Y.Lin, R.Ran, Z.Shao. *Int. J. Hydrogen Energy*, **35**, 8171 (2010)